

Plasma and magnetic field interaction on large and small scales within the solar atmosphere

MSc. Jose Iván Campos Rozo

August 10, 2023



PhD Dissertation

Plasma and magnetic field interaction on large and small scales within the solar atmosphere

MSc. Jose Iván Campos Rozo

in partial fulfillment of the requirements for the degree of
Doctor in Science

Supervisors Univ.-Prof. Dr. Astrid M. Veronig

August 10, 2023

MSc. Jose Iván Campos Rozo

Plasma and magnetic field interaction on large and small scales within the solar atmosphere

Thesis in partial fulfillment of the requirements for the degree of Doctor in Science;

Department for Geophysics, Astrophysics and Meteorology,
Institute for Physics, NAWI Graz, University of Graz.

Supervisor: Univ.-Prof. Dr. Astrid M. Veronig¹

External Reader: Assoc. Prof. MSc. Dr. Michal Švanda^{2,3}

¹ Institut für Physik, Institutsbereich Geophysik, Astrophysik und Meteorologie,
NAWI Graz, University of Graz, Universitätsplatz 5/II, 8010 Graz, Austria.

² Astronomical Institute, Faculty of Mathematics and Physics, Charles University,
V Holešovičkách 2, 182 00 Praha 8, Czech Republic

³ Astronomical Institute, Czech Academy of Sciences,
Fričova 298, 251 63 Ondřejov, Czech Republic

Abstract

In this study, we investigate the solar surface, focusing on the properties of magnetic fields and the flow of apparent motions on the photosphere. We analysed different datasets obtained from space-based telescopes such as the Helioseismic and Magnetic Imager (HMI) onboard the Solar Dynamics Observatory (SDO) and the Solar Optical Telescope (SOT) onboard the Hinode satellite, as well as the ground-based GREGOR solar telescope, employing image processing techniques to extract relevant features from intensity images and vector magnetograms.

To gain a deeper understanding of the different features we can observe in the solar photosphere, requires that we examine the interaction between convective flows and magnetic fields in newly emerging active regions. Using data from the HMI instrument onboard SDO, we applied local correlation tracking (LCT) methods to study the statistical distribution of proper motions on the photosphere during the emergence, formation, and evolution of an active region. The mean value of the velocities distribution within small quiet areas, obtained by averaging over a period of 2 hours, reaches values of $v_{Cont} = 72 \pm 8.8 \text{ m s}^{-1}$ associated with plasma motions, while the mean velocity derived from line-of-sight (LOS) magnetic elements is $v_{LOS} = 54 \pm 10.7 \text{ m s}^{-1}$. However, when strong magnetic flux newly emerges in the region of interest, the horizontal motions inferred from the LOS magnetograms reach values of $v_{LOS} = 65 \pm 2.2 \text{ m s}^{-1}$, becoming slightly higher than the plasma apparent motions ($v_{Cont} = 55 \pm 2.5 \text{ m s}^{-1}$), unveiling the influence of the newly emerging magnetic field that alters the behaviour within the region. Our analysis reveals a two-component velocity distribution, with one component representing stable and more random background flows following a Rayleigh distribution and the other component is associated with variable flux emergence. During this investigation, we also noted the existence of correlations and anti-correlations of the temporal evolution of the proper motion parameters associated with the plasma granular motions and the magnetic features motions.

Among the different magnetic features of the solar surface, solar pores and the properties of magnetic fields on their boundaries, are an important topic. A previous study conducted by García-Rivas et al. (2021) analysed the properties of the vertical magnetic field in one single solar pore. To increase the statistics, we study the evolution of the vertical magnetic fields in a sample of 6 pores that showed a stable evolution over at least 27 hours, using images from the SDO-HMI instrument. Our

outcomes indicate that the maximal values of the vertical magnetic field on the boundaries of the solar pores under study range from 1400 G to 1600 G, with a standard deviation between 7.8 and 14.8%. In addition, we found that the inclination angle of the magnetic field lies within a range of $30 \pm 7^\circ$ with respect to the local radial direction, supporting the notion that the magnetic field structure in solar pores is mainly vertical.

Furthermore, the photosphere exhibits small-scale features that contribute to the local and global evolution of the solar magnetic fields. Among these features, we explore the characteristics of magnetic bright points (MBPs) on the surface of the Sun. We analysed high-resolution observations from the space-based SOT onboard the Hinode mission and from the High-resolution Fast Imager (HiFI) instrument mounted on the ground-based 1.5 m solar GREGOR telescope. We detected and tracked MBPs, to determine their size and velocity distributions. Our results demonstrated that the areas and diameters of MBPs display log-normal distributions with two distinct components, likely related to different magnetic flux elements in the solar photosphere. The first component of the size distribution displays values ranging from $2200 - 15000 \text{ km}^2$, whereas the second component shows sizes in the range $6300 - 40000 \text{ km}^2$, but decreases in quantity. The mean velocity value for the first component is 7.5 km s^{-1} , while for the second component, it is 1.9 km s^{-1} .

The findings of this thesis contribute to the development of models for the solar dynamo, magnetic flux emergence, and the characterisation of fine-scale structures within the solar atmosphere. Additionally, the thesis highlights the role of high-resolution data in accurately analysing and interpreting solar observations.

Zusammenfassung

Diese Dissertation untersucht die Photosphäre der Sonne mit einem Fokus auf den Eigenschaften des Magnetfeldes als auch des Strömungsfeldes. Zu diesem Zweck wurden Datensätze analysiert, welche durch weltraumgestützte Teleskope, wie dem Helioseismic and Magnetic Imager (HMI) an Bord des Solar Dynamics Observatory (SDO) und dem Solar Optical Telescope (SOT) an Bord des Hinode Satelliten, aufgenommen wurden. Des Weiteren verwendeten wir bodengestützte Daten des GREGOR Sonnenteleskopes. Die Analyse der Daten wurde mittels computergestützter Bildverarbeitungstechniken durchgeführt.

Um tiefere Einsichten in verschiedene Strukturen auf der Sonnenoberfläche zu gewinnen, untersuchten wir die Interaktion zwischen den konvektiven Plasma-Strömungen und den Magnetfeldern innerhalb neu entstehender aktiver Regionen. Wir wendeten die Local Correlation Tracking Methode auf HMI-Daten an, um die statistische Verteilung des Strömungsfeldes der Photosphäre während des erstmaligen Erscheinens, und der anschließenden Entwicklung einer Aktiven Region zu verfolgen. Der Mittelwert, der Geschwindigkeitsverteilung der Plasmastromungen über einen 2-stündigen Zeitraum in einer ruhigen Region erreichte Werte von $v_{Cont} = 72 \pm 8.8 \text{ m s}^{-1}$, während die mittlere Geschwindigkeit, die aus den magnetischen Elementen ermittelt wurde, einen Wert von $v_{LOS} = 54 \pm 10.7 \text{ m s}^{-1}$ aufwies. Für den Fall, dass neuer starker magnetischer Fluss die Oberfläche erreicht, können die horizontalen Geschwindigkeiten der Magnetfeldelemente Werte von $v_{LOS} = 65 \pm 2.2 \text{ m s}^{-1}$ annehmen. Dieser Wert ist etwas größer als jener für die Plasmageschwindigkeiten, $v_{Cont} = 55 \pm 2.5 \text{ m s}^{-1}$. Dies zeigt den Einfluss von neu auftauchenden Magnetfeldern auf die sich entwickelnden Strömungsverhältnisse. Unsere Analyse zeigt eine Zweikomponenten Geschwindigkeitsverteilung, in welcher eine Komponente mit der zufälligen aber stabilen Hintergrundströmung über eine Rayleigh Verteilung verknüpft ist, während die zweite Komponente durch das Auftauchen (engl., emergence) neuen magnetischen Flusses verursacht wird. Unsere Untersuchungen legen auch die Existenz von Korrelationen und Anti-Korrelationen der zeitlichen Entwicklung der Eigenbewegungs-Parameter, welche mit der granularen Bewegung bzw. den Magnetfeldstrukturen assoziiert sind, nahe.

Innerhalb der magnetischen Strukturen, welche sich auf der Sonnenoberfläche beobachten lassen, nehmen "Poren" und die Analyse ihrer magnetischen Begrenzung, eine besondere Stellung ein. Eine Studie von García-Rivas et al. (2021) analysierte

die Eigenschaften des vertikalen Magnetfeldes einer einzelnen Sonnenpore. Um die Aussagekraft dieser Studie zu erhöhen, untersuchten wir die Entwicklung des vertikalen Magnetfeldes für eine Gruppe von 6 weiteren Poren mittels Aufnahmen des HMI Instrumentes. Diese Poren zeigten eine stabile Entwicklung über zumindest 27 Stunden. Unsere Ergebnisse lieferten für die betrachteten Poren Maximalwerte des vertikalen Magnetfeldes von 1400 G bis 1600 G mit einer Standardabweichung von 7.8 bis 14.8%. Zusätzlich bestimmten wir die Inklinationswinkel des Magnetfeldes, welche Werte zwischen $30 \pm 7^\circ$, in Bezug auf die lokale Senkrechte, aufwiesen. Dies unterstützt die Annahme, dass das Magnetfeld in solaren Poren hauptsächlich vertikal ausgerichtet ist.

Des Weiteren besitzt die Photosphäre kleinskalige Strukturen, welche zur Entwicklung des lokalen und globalen Sonnenmagnetfeldes beitragen. Innerhalb dieser Strukturen untersuchten wir die Charakteristika der magnetisch hellen Punkte (engl., magnetic bright points – MBPs) mittels hochauflösende Beobachtungen des weltraumgestützten SOT Instrumentes. Darüberhinaus verwendeten wir auch Daten des bodengebundenen High-resolution Fast Imager (HiFi) Instrumentes. Wir haben MBPs detektiert und verfolgt, um ihre Größen- und Geschwindigkeitsverteilung zu bestimmen zu können. Unsere Ergebnisse bestätigen, dass die Flächen- und Durchmesserverteilungen der MBPs log-normal verteilt sind und zwei unterscheidbare Komponenten aufweisen. Diese Komponenten sind wahrscheinlich mit unterschiedlichen magnetischen Flusselementen verknüpft. Die erste Komponente, der Größenverteilung zeigt Werte zwischen 2200 und 15.000 km². Die zweite Komponente weist Größen im Bereich von 6300 bis 40.000 km² auf, jedoch mit einer verringerten Häufigkeit. Der Mittelwert für die erste Komponente der Geschwindigkeitsverteilung beträgt 7.5 km s⁻¹, während der Mittelwert für die zweite Komponente bei 1.9 km s⁻¹ liegt.

Die Ergebnisse dieser Arbeit tragen zur Entwicklung von Modellen des solaren Dynamos, der Magnetfeldentstehung und der Charakterisierung von kleinskaligen Strukturen innerhalb der Sonnenatmosphäre bei. Zusätzlich beleuchtet die Arbeit, die wesentliche Rolle von hochauflösenden Beobachtungsdaten, in der exakten Analyse und Interpretation von Sonnenbeobachtungen.

Acknowledgement

The culmination of this thesis has been possible through the collective efforts and support of numerous people. Their unhesitating encouragement and invaluable insights have been crucial to complete this work, and for this reason, I would like to express my deepest gratitude to all of them.

The person I am most grateful for, and to whom I want to express my deepest love and gratitude, is my mother, María Helena Rozo Hernández. She has been a persevering pillar of strength, constantly fighting against all odds to provide my siblings and me with constant support throughout our lives. I am profoundly thankful for the amazing mother that the universe blessed me with. Her selflessness, resilience, and unconditional love have been fundamental in forming the person I am today.

I would like to thank my supervisors, Prof. Dr. Astrid M. Veronig and Dr. Mag. Dipl. Ing. Dominik Utz, for their countless expertise, constant support, and dedicated time throughout this work. I am especially grateful to Dr. Utz for his innumerable hours of delightful scientific discussions, his friendship, and for illuminating our ideas with endless laughs and joy, making me feel like Graz could be my second home.

I want to thank specially all the administrative, technical, and academic staff of the Department for Geophysics, Astrophysics and Meteorology (IGAM) at the Institute of Physics of the University of Graz. I thank DI Roland Maderbacher for all the help when the technical support, whenever needed, but especially I really appreciate the always good mood shownen by Mag. Klaus Huber, and the good conversations in the department corridors. I want to thank Prof. Arnold Hanslmeier who contributed to the end of this wonderful career.

I would also like to express my gratitude to a few of my closest friends in Graz. Although our circle may be small, I feel it essential to mention the persons who have played a significant role making my time in Graz more enjoyable and helping with my integration into the community. In particular, I want to express my thankfulness to Prof. Dr. Manuela Temmer, Dr. Ewan Dickson, Dr. Stefan Hofmeister, Dr. Aaron Hernández Pérez, Dr. Isabell Piantschitsch, and Mag. Kilian Krikova for their invaluable friendship.

I would like to extend my special thanks to Prof. Mag. Benjamín Calvo Mozo and Prof. Dr. Santiago Vargas Domínguez, who, even after my leaving the National

Astronomical Observatory in my home country, continued to provide guidance, determined friendship, invaluable advice, and above all, immense patience during my process at the University of Graz.

I am deeply thankful to my friends in my home country, and although it would be very difficult to mention each one individually without turning this thesis into an endless list of my favorite people, I would like to acknowledge a few of them: Dayhana R., Walter G., Camilo B., Jorge T., Eduard B., Olga L., Anaceida M., Islena B., Valeria Q., Henry O., Alejandra O., Miguel Q., Jhonattan P., Pahola P., Sebastian H., Javier S., Tatiana A., Luisa A. (pollita), Camilo B.C., Camilo G., Gina T., Jennyffer M., Lizeth B., and many others who have played a significant role in my life and during this process. However, I must express my special and loving gratefulness to Architect Linda Katherine Díaz Agudelo, who has been there for me during some of my most challenging days, always reminding me all the time of her immense pride in my small triumphs.

I gratefully acknowledge the Austrian Science Fund (FWF): P27800 (PI: Utz) and I 3955-N27 (PI: Hanslmeier) for supporting this project. This work was also partially supported and funded by grant 21-16508J of the Grant Agency of the Czech Republic.

Finally, I would like to thank the administrative team at our University of Graz that assisted me during my time as Ph.D. student. Also, I would like to thank all the different academic institutions which host the different meetings, workshops, summer schools, and observational campaigns that I applied for and participated in.

Contents

Abstract	v
Zusammenfassung	vii
Acknowledgements	ix
1 Introduction	1
1.1 Background and Motivation	1
1.2 Objectives and Research Questions	2
1.3 Overview of the Thesis Structure	3
2 The Sun and its Magnetic Field	5
2.1 The Solar Magnetic Field	5
2.2 Solar Atmosphere	7
2.2.1 Solar Photosphere	8
2.2.2 Chromosphere	10
2.2.3 Transition Region	11
2.2.4 Solar Corona	12
2.2.5 Active Regions and their Dynamics	14
2.2.6 Small-scale magnetic fields	17
2.3 High-Resolution Observations and Imaging Techniques	19
2.3.1 Adaptive Optics (AO) system	20
2.3.2 Solar Image Reconstruction	22
2.3.3 Proper Motions	23
2.4 Space and ground-based telescopes	24
2.4.1 Helioseismic and Magnetic Imager (HMI)	24
2.4.2 Solar Optical Telescope (SOT)	25
2.4.3 GREGOR and the High-resolution Fast Imager	26
Bibliography	29
3 Paper 1	39
4 Paper 2	55
5 Paper 3	65
6 Discussion and Conclusions	79
List of publications	81

Introduction

1.1 Background and Motivation

The interaction between magnetic fields and ionised plasma gas is a fundamental aspect for the understanding of the connection between the different layers of the solar atmosphere. Comprehension of the large-scale magnetic fields present in features such as sunspots and Active Regions (AR) is crucial to understanding the origin of solar magnetic fields and their implications on solar dynamics and different energetic activity, including solar flares and coronal mass ejections (e.g. reviews by Green et al., 2018; Toriumi and Wang, 2019). This study aims to track the proper motions of various structures in the solar photosphere on different spatial scales, such as granulation, mesogranulation, and supergranulation, as well as magnetic bright points, ARs and small pores, and to explore their potential connection with features in the upper layers of the solar atmosphere. Numerous authors have investigated photospheric flow fields, and apparent motions on active regions (e.g., November and Simon, 1988; Welsch et al., 2004; Schuck, 2006).

Recent advances in space-based and ground-based solar telescopes have made it possible to observe the various solar features in higher spatial and temporal resolutions than ever before. The research in this thesis primarily utilises solar data images obtained from the Helioseismic and Magnetic Imager (HMI; Scherrer et al., 2012) instrument onboard the Solar Dynamics Observatory (SDO; Pesnell et al., 2012) operated by the National Aeronautics and Space Administration (NASA). The HMI instrument provides observations with a physical resolution of approximately 1 arc-second, and time cadences of 45 seconds and 720 seconds (12 minutes) depending on the data product. This research also used data from the Solar Optical Telescope (SOT; Tsuneta et al., 2008a) onboard of the Hinode mission (Solar-B; Kosugi et al., 2007), led by the Japan Aerospace Exploration Agency (JAXA), which has a temporal resolution of 30 seconds with a spatial sampling resolution of 0.108 arcseconds per pixel. Finally, solar images acquired by the High-resolution Fast Imager (HiFI) instrument mounted on the GREGOR 1.5 m solar telescope supervised mainly by the Leibniz Institute for Solar Physics (KIS) and the Instituto de Astrofisica de Canarias (IAC), with a high spatial sampling of approximately 0.03 arcseconds per pixel and an average temporal resolution of 5 seconds. The intensity and magnetic field data require specialised processing techniques, and this study uses advanced methods for data processing. A deeper description of the different instruments employed during this research can be found in Section 2.4.

A comprehensive study of the Sun, accessing various wavelengths of the electromagnetic spectrum, is essential to understand the connections between small-scale magnetic flux tubes in the photosphere with multiple features in the upper atmospheric layers. By exploring the Sun from radio wavelengths to the high-energy X-rays and gamma rays, we can gain insights into the formation of large-scale magnetic fields and the vast release of magnetic energy during solar flares, or the role that small-scale magnetic fields play in creating these structures. Furthermore, studying the interactions between the small-scale magnetic fields and the solar plasma can enhance our understanding of the Sun's behaviour and its long-term evolution (Thompson et al., 2009).

1.2 Objectives and Research Questions

Objectives

1. The main aim of this work is to investigate the interaction and connection between the plasma and magnetic fields within the solar atmosphere on both large and small scales.
2. We study the properties of magnetic fields in AR and their impact on the solar atmosphere and its relation to the plasma. ARs are the largest manifestation of the magnetic field on the solar surface.
3. Small-scale magnetic fields require the analysis of high-resolution images of the solar photosphere to track the proper motions of various structures and understand their connection with the upper layers of the solar atmosphere.

Research Questions

This study aims to investigate the interaction between plasma and magnetic fields on both large and small scales within the solar atmosphere, with a particular focus on the photosphere and the magnetic features there. The following research questions will guide our research:

1. What is the role of plasma in interacting with magnetic fields in large-scale structures such as active regions, sunspots, and solar pores?
2. How do small-scale magnetic structures on the photosphere contribute to the formation of large-scale magnetic fields in the solar atmosphere?
3. What are the properties of the emergence of magnetic fields in ARs, and how do they influence the dynamics of the solar photosphere?

4. How can we use high-resolution images of the solar photosphere to track the apparent motions of different structures, such as granules or magnetic bright points, and what is their possible connection with the upper layers of the solar atmosphere?
5. What advanced techniques can be used for processing different magnetic field data, and how can they help us for a better understanding of the interaction between plasma and magnetic fields in the solar atmosphere?

1.3 Overview of the Thesis Structure

The structure of the present thesis consists of six chapters, beginning with this introduction, followed by an overview of the Sun and its magnetic field, which provides a background about the solar atmosphere, from the solar corona to the photosphere. Additionally, a brief description of high-resolution observations and different imaging, processing, and analysis techniques are discussed in Chapter 2. Chapters 3–5 present a compilation of the three research papers published in international peer-reviewed journals, which build the core of this thesis. Below is an executive summary of each of the three papers:

- **Paper 1** – Campos Rozo, J. I., Utz, D., Vargas Domínguez, S., Veronig, A., & Van Doorsselaere, T. 2019. Photospheric plasma and magnetic field dynamics during the formation of solar AR 11190. *Astronomy & Astrophysics*, 622, A168. DOI: [10.1051/0004-6361/201832760](https://doi.org/10.1051/0004-6361/201832760).

In this paper, we focused on the analysis of the apparent convective flows of emerging active regions observed in the photosphere. The main results indicate a two component distribution: one component represents stable background motions that follow a Rayleigh distribution, while the second component is associated with strong changes of the flux emergences, such that background apparent velocities reach values of $v_{Cont} = 72 \pm 8.8 \text{ m s}^{-1}$ and $v_{LOS} = 54 \pm 10.7 \text{ m s}^{-1}$, whereas when new strong magnetic field emerge into the region of interest, the horizontal flows reached values of $v_{LOS} = 65 \pm 2.2 \text{ m s}^{-1}$ and $v_{Cont} = 55 \pm 2.5 \text{ m s}^{-1}$, demonstrating that the average proper motions of the analysed field of view depend on the presence of new strong magnetic fields.

- **Paper 2** – Campos Rozo, J. I., Vargas Domínguez, S., Utz, D., Veronig, A. M., & Hanslmeier, A. 2023. Exploring magnetic field properties at the boundary of solar pores: A comparative study based on SDO-HMI observations. *Astronomy & Astrophysics*, 674, A91. DOI: [10.1051/0004-6361/202346389](https://doi.org/10.1051/0004-6361/202346389).

In this paper, the focus was on the analysis of the properties of magnetic fields on the boundaries of solar pores. The main goal of this new study is to increase the sample statistics of a previous work presented by García-Rivas et al. (2021) and investigate the evolution of vertical magnetic fields at the borders of pores,

which are found to range in values from 1400 G to 1600 G, with standard deviations between 7.8% and 14.8%. Additionally, the inclination angle of the magnetic field showed small values of $30 \pm 7^\circ$, consolidating that the magnetic field in the umbra or solar pores is mostly vertical.

- **Paper 3** – Berrios Saavedra, G., Utz, D., Vargas Domínguez, S., Campos Rozo, J. I., González Manrique, S. J., Gömöry, P., Kuckein, C., Balthasar, H., & Zelina, P. 2022. Observational evidence for two-component distributions describing solar magnetic bright points. *Astronomy & Astrophysics*, 657, A79. DOI: [10.1051/0004-6361/202141231](https://doi.org/10.1051/0004-6361/202141231).

This paper studies the significance of small-scale magnetic features on the photosphere. Specifically, we focused on investigating the characteristics of magnetic bright points (MBPs) on the solar surface. During this analysis MBPs were detected and tracked, and their size and velocity distributions were measured. The results revealed that the areas and diameters of MBPs exhibit log-normal distributions with two distinct components, which are likely associated with different magnetic flux elements. As co-author in the present paper, I contributed in some of the post-processing stages, including: coalignment, and prefiltering of 5-minute oscillations (p-modes) to improve velocity and apparent motion analysis, calculating frame by frame, or MBP by MBP, without taking into account time average, as well as applying LCT to calculate horizontal flows and vertical divergences, showing a correspondence between the MBPs and those calculated divergences (see Figure 1 in Chapter 5).

Finally, Chapter 6 provides a general discussion and conclusion of the research, summarising the key findings and their implications. This chapter concludes with the significance of the research and its contribution to the community.

The Sun and its Magnetic Field

This chapter provides a brief overview of the fundamental characteristics of the solar atmosphere and various processes occurring within each layer of the solar atmosphere. To obtain a comprehensive understanding of the physical phenomena occurring in the Sun, it is essential to know some important basic attributes of our star. Moreover, the unique proximity of the Sun to Earth gives us the opportunity to investigate the different physical processes in highest detail. Below we summarise various fundamental parameters of the Sun (Mullan, 2010):

-  Spectral classification: G2V star on the main sequence within the Hertzsprung-Russel diagram.
-  Effective surface temperature: $T_{eff} = 5777$ K.
-  Mass: $M_\odot = 1.9884 \times 10^{30}$ kg.
-  Radius: $R_\odot = 6.9568(\pm 0.0003) \times 10^5$ km.
-  Distance from Sun to Earth: Defined as 1 astronomical unit (AU). $D_\odot = 149,597,870.691$ km.
-  Luminosity: $L_\odot = 3.8416 \times 10^{26}$ W.
-  Surface gravity: $g_s = 274.216$ ms⁻²
-  Average density: $\rho_\odot = 10^{-6} - 10^{-7}$ g cm⁻³

2.1 The Solar Magnetic Field

The magnetic field of the Sun is a complex and dynamic system that plays a critical role in the behaviour and activity of our host star. The magnetic field is a fundamental component of the Sun's structure and evolution as well as the source of its variability and activity. It plays a crucial role in regulating the total solar energy and drives the behaviour of the solar wind, which has far-reaching effects on the space environment of the entire solar system. In addition, the magnetic field is closely linked to various physical processes that occur within the Sun, such as convection, radiation, and turbulence, making it a crucial factor in understanding the dynamics of our star (Schrijver et al., 2019).

The most widely accepted theory for the generation of the magnetic field is the dynamo mechanism (Parker, 1970), which involves the conversion of kinetic energy

into magnetic energy. This process occurs in a thin interface region between the radiative zone and the convective zone called the tachocline, a term introduced by Spiegel and Zahn (1992). In this interface region, the plasma changes from a solid-like rotation in the core and radiative zone to a differential rotation in the convective region (Charbonneau, 2014). The resulting shear motion creates a stress that generates magnetic fields via the motion of charged particles which plays a key element in the dynamo process (Parker, 1955). There have been various studies and observations supporting the dynamo theory, including the detection of helioseismic waves, which provide a mechanism to “observe” the Sun’s interior and to reveal the existence of the tachocline zone (see: Gough and Thompson, 1990; Spiegel and Zahn, 1992; Brandenburg and Subramanian, 2005). Additionally, the detection of magnetic fields in other stars that exhibit similar rotational characteristics to the Sun has further supported the idea that a dynamo mechanism is responsible for generating magnetic fields in stars (Reiners and Basri, 2009). The magnetic fields generated by this mechanism emerge through the Sun’s surface due to magnetic buoyancy (Hansen et al., 2004; Cheung and Isobe, 2014), leading to a variety of phenomena, such as the formation of sunspots or active regions (see Fig. 2.1), as well as high-energy phenomena including solar flares, and coronal mass ejections (Parker, 1979).

Different observational techniques have been developed to study the magnetic field of the Sun, including the Zeeman and Hanle effects. The Zeeman effect was initially observed by Zeeman (1897) in laboratory experiments. In principle, the Zeeman effect measures the splitting and separation of spectral lines in the presence of a magnetic field measured in the line-of sight direction. Within the solar atmosphere, the Zeeman effect has been utilised to estimate the magnetic field strength in sunspots, where the field intensity can exceed that of the surrounding plasma by several orders of magnitude (Stenflo, 2013). An additional and important technique applied to investigate the solar magnetic field is the Hanle effect, which was first observed by Hale (1908). This effect consists of the modification of the polarisation state of light as it passes through a medium with a magnetic field (Wood and Ellett, 1923). The Hanle effect is particularly valuable for exploring small and weak magnetic fields within the solar atmosphere, such as those detected in the chromosphere and transition region (Trujillo Bueno et al., 2006). Spectropolarimetry aids as another typical approach for investigating the full vector magnetic field. It requires the measurement of Stokes parameters by polarising the incident light coming from the Sun (del Toro Iniesta, 2003). In the textbook *Magnetic Fields in the Solar System* (2018), a broader perspective on magnetic fields is presented, including those of other planets and the interplanetary medium. The book provides a comprehensive review of the current knowledge on the solar magnetic field, from its origin and generation to its impact on the Earth’s environment.

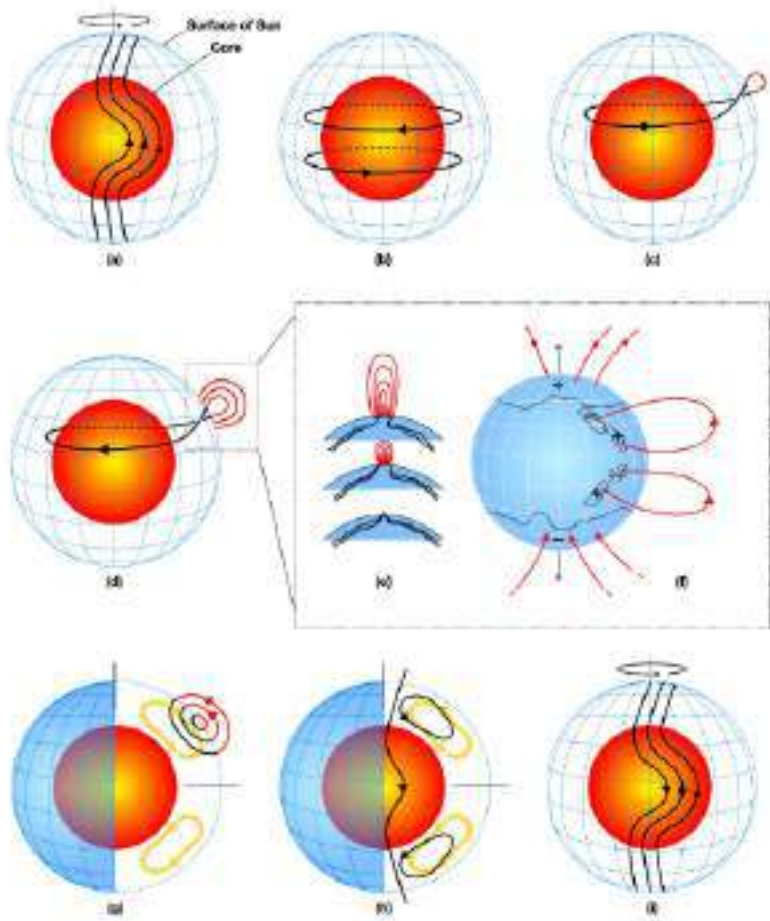


Fig. 2.1: The Sun's dynamo operates from the tachocline region, just below the solar convection zone, where the shear of the poloidal magnetic field by differential rotation creates a toroidal field from an original weak poloidal field. Sunspots are formed from rising buoyant loops, and the magnetic flux undergoes reversal and transport toward the poles. Image from https://www.nasa.gov/vision/universe/solarsystem/solar_cycle_graphics.html

These studies provide a full understanding of the solar magnetic field, including its generation, evolution, and effects on the solar atmosphere and outer heliosphere. Through a variety of simulations and observational techniques, they offer valuable insights into the magnetic field of the Sun, significantly advancing our knowledge of the physics of the solar atmosphere. Furthermore, these studies highlight the importance of investigating the Sun's magnetic activity, not only for comprehending the behaviour of our star, but also for assessing the impact of solar variability on the Earth and space environment.

2.2 Solar Atmosphere

The solar atmosphere is a complex and dynamic region of the Sun, exhibiting various phenomena and structures. It comprises distinct layers, each playing a crucial role with its own unique characteristics and importance for the understanding of solar

behaviour. The interaction of magnetic field, solar plasma, and energy transport mechanisms gives rise to a diverse range of high-energy events, including solar flares, coronal mass ejections, prominences, and coronal loops (Aschwanden, 2004).



Fig. 2.2: The solar atmosphere shows various features that can be observed at different wavelengths. This is an example of the multiple observations in the UV and EUV from the Atmospheric Imaging Assembly (AIA Lemen et al., 2012) onboard SDO. Image from <https://blogs.nasa.gov/sunspot/page/6/>

The solar atmosphere is divided into four well-differentiated layers named photosphere, chromosphere, the transition region, and the solar corona, which will be described in the following subsections.

2.2.1 Solar Photosphere

The photosphere is considered the “surface” of the Sun. It exists at a depth where the opacity is no longer sufficient to inhibit the escape of light coming from the solar interior. The change of the optical depth is defined by:

$$d\tau_\lambda = -\kappa_\lambda dh; \quad (2.1)$$

where τ_λ denotes the optical depth, κ_λ is the absorption coefficient, λ is the wavelength, and the negative sign indicates that the optical depth increases when the height coordinate h is becoming smaller. The photosphere exhibits an effective surface temperature of 5777 K, with a thickness of approximately 500 km at τ_{5000} . The average gas pressure within the photosphere is approximately given by $P_g \sim 10^4$ Pa. Due to the relatively lower temperatures dominating this layer, the plasma particles are less ionised than in the solar interior, resulting in a reduced electron density. These conditions facilitate the escape of photons from the solar surface. The advances in techniques, technology, and theory in solar physics have driven forward high-resolution imagery, revealing the intricate composition of irregular structures on the photosphere that exhibit continuous dynamics. Within the solar

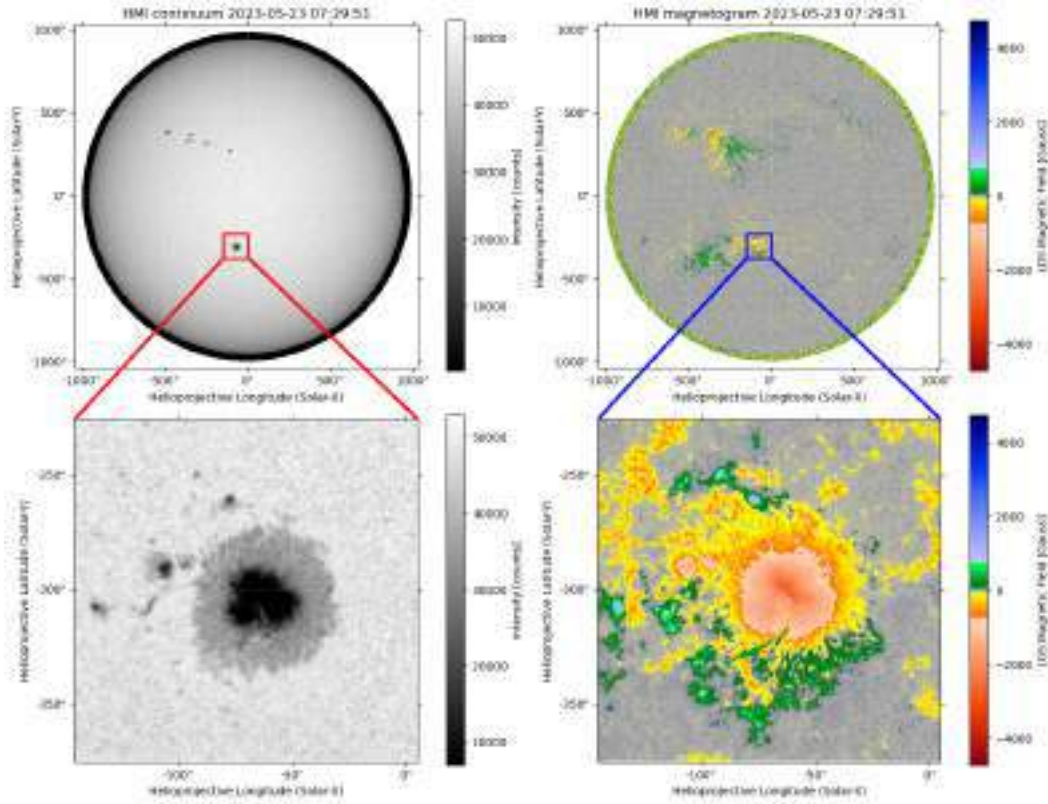


Fig. 2.3: Photosphere continuum and LOS magnetic field images. The top row shows full-disk intensity map (left) and magnetogram (right). The bottom row displays a zoomed AR with a large sunspot and multiple solar pores around the magnetic structures. The zoomed magnetogram (right) exhibits the intricate and complex magnetic field on the photosphere related to the structures observed in the intensity map (left). Images were taken by the HMI instrument onboard of SDO. Date: 2023-05-23 07:29:51 UT.

surface, various distinct structures can be observed, among them, convection cells or granules forming the granulation pattern. These granules comprise three different configuration sizes, namely granulation, mesogranulation, and supergranulation, each characterised by a specific spatial scale, lifetime, and speeds associated with each of them. Among the mentioned patterns, solar granulation is the smallest and most predominant which can be described as a brighter central part bounded by dark lanes, with hot plasma ascending with a vertical speed of 0.4 km s^{-1} . This material subsequently transitions to a horizontal motion, with outward radial flows of 0.25 km s^{-1} . Finally, the plasma joins downward flows at the edges of the granules (see Title et al., 1986; Hathaway et al., 2000).

As previously mentioned, the photosphere is a complex and non-uniform layer, which results in a similarly intricate and much more complicated magnetic field. The solar photosphere is dominated mainly by plasma pressure forces, while in the chromosphere equipartition can be observed between plasma and magnetic pressure, and finally in the corona magnetic pressure dominates over plasma pres-

sure. The transition between layers from gas dominance to magnetic dominance is characterised by using the well-known plasma- β parameter:

$$\beta = \frac{P_g}{P_B} = \frac{nk_B T}{B^2/(2\mu_0)}; \quad (2.2)$$

where P_g and P_B are the gas and magnetic pressure, respectively. The gas pressure is given by the number of molecules n , the Boltzmann's constant k_B , and the plasma temperature T , whereas the magnetic pressure is given in terms of magnetic field strength B and μ_0 the magnetic permeability in vacuum. In terms of plasma- β , the solar photosphere has a $\beta \gg 1$, confirming the dominance of plasma in this layer.

The magnetic field on the solar surface exhibits a wide range of scales, including large-scale structures spanning megametres as well as small-scale magnetic elements on the order of a few kilometres (see Fig. 2.3). These elements display seemingly random movements and rapid dynamics. Despite this apparent randomness, they come together in distinct configurations to form large magnetic structures offering valuable insights into the behaviour of the Sun's magnetic phenomena. Some of these large- and small-scale magnetic features include:

-  Sunspots and active regions,
-  Solar pores,
-  Magnetic Bright Points (MBPs),
-  and others such as plages and faculae.

2.2.2 Chromosphere

The chromosphere, an irregular layer positioned above the solar surface, exhibits a large number of characteristics. The temperature in this layer rises from the temperature minimum (Holweger, 1967) which is about 4500 K to nearly 20000 K, causing the presence of the dominant neutral hydrogen atom which emits in a visible spectral line with a wavelength of 6562.8 Å named H α line (Zirin, 1988). H α is the first spectral line in the Balmer series (Balmer, 1885) which is emitted when an electron transitions from the third energy level to the second lowest level.

Spectroscopic analysis reveals a multitude of structures forming in the chromosphere, including the chromospheric magnetic network, the bright plages surrounding the sunspots, dark filaments crossing the solar disk, and prominences rising above the solar limb. The more sensitive and strongest spectral lines that can be observed in the chromosphere include the emissions from other hydrogen lines as H β , H γ , and H δ centred at wavelengths of 4861, 4340, and 4102 Å respectively. Other interesting lines can be found centred at 5876 Å (Helium), or calcium lines

such as Ca II H (3968 Å) and Ca II K (3934 Å) (Mullan, 2010). The chromosphere is well-known for its extraordinary dynamics and magnetic activity, with multiple examples of energetic and rapid events such as solar flares (Shibata and Magara, 2011), filament eruptions (Schmieder and Aulanier, 2012) and jet-like spicules (de Pontieu et al., 2007), among other phenomena.

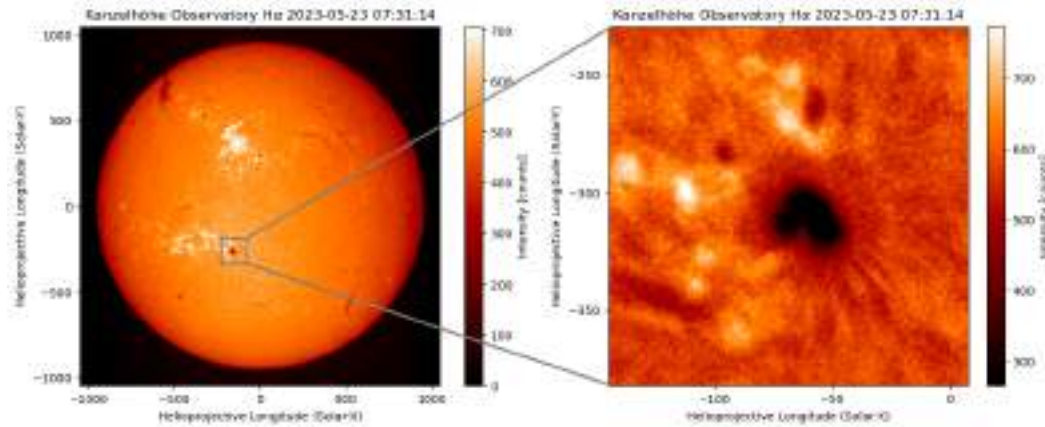


Fig. 2.4: Image of the solar chromosphere in the Halpha line at a wavelength of 6562.8 Å. Left: Full-disk image of the chromosphere, where dark features show an example of filaments. Right: Zoomed field of view (FOV) shows the same active region as Fig. 2.3. Image taken at the Kanzelhoehe Observatory. Date: 2023-05-23 07:31:14 UT.

Different observations of the solar chromospheric spectral lines have revealed the presence of extensive areas of roughly horizontal magnetic field. These fields expand due to the decrease of the gas pressure at higher atmospheric heights, and then, eventually, fill the atmosphere with magnetic fields. This magnetic cover located at the lower chromosphere is called the chromospheric magnetic canopy and is typically referred to as the transition point between the gas-dominated photosphere and magnetic field-dominated solar corona with a characteristic $\beta \sim 1$. The magnetic canopy is observed as a layer of magnetic fields parallel to the solar surface, and displays weak magnetic field strength, reaching values around 100 G, and covering a substantial part of the "magnetic field-free" solar photosphere. For quiet Sun regions, this structure starts at a height of about 700–1000 km from the surface, and its intricate details and role in shaping the Sun's magnetic behaviour require further investigation (Steiner, 2000).

2.2.3 Transition Region

The transition region, located between the upper chromosphere and corona, is a remarkable and narrow layer of the solar atmosphere that exhibits distinct characteristics. This region plays a significant role due to its steep gradient in temperature, starting from the lower part with values of approximately 20,000 K, to its upper part reaching temperatures around 10^6 K, and the rapid drop of density over a very small height range of the order of a thousand kilometers.

Besides the ionisation of Hydrogen at such high temperatures, the predominant emissions from this atmospheric layer come up from C IV, O IV, and Si IV (Doschek, 1997). These specific spectral lines predominantly emit in the ultraviolet (UV) region of the solar spectrum, offering valuable insights into the structure and distinctive attributes of the transition zone.

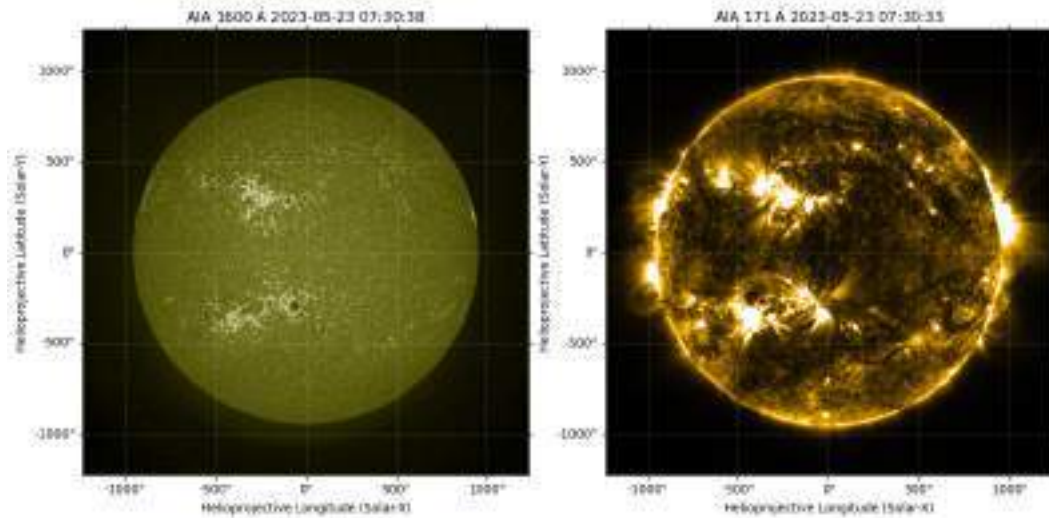


Fig. 2.5: Images of the solar transition region acquired with AIA/SDO. On the left: AIA channel 1600 Å imaging the upper chromosphere and transition region. On the right: AIA channel 171 Å show region between the upper transition region and lower corona. The observations were made on May 23, 2023, at 07:30 UT.

Many imaging instruments have been used to observe the transition region in the Sun. One of the most prominent is the AIA instrument, incorporated onboard the SDO satellite (e.g. see Fig. 2.5), covering a wide spectral range, enabling detailed imaging and analysis of the transition region as well as additionally the solar corona, and its associated phenomena. Those energetic events are primarily driven by small-scale magnetic reconnections which generate nano-flares. As Moses et al. (1994) showed, these nano-flares tend to occur in areas of strong magnetic chromospheric network, while avoiding the center of the cells in the network. However, despite the significant energy released by these events, Cook et al. (1987) suggested that these processes are not sufficient to fully explain the elevated temperatures observed in the transition region and the solar corona.

2.2.4 Solar Corona

The solar corona is the outermost layer of the solar atmosphere, and hides the solution to one of the most unresolved enigmas in the field of solar physics, known as the coronal heating problem. The faint light of the solar corona has an intensity of approximately 5×10^{-6} times the brightness at the solar disk center (van de Hulst, 1950). Because of its extremely low density, the solar corona is indistinct and

difficult to observe directly, except during total solar eclipses when it appears as a radiant crown-like structure around the Sun (see Fig. 2.6.a), or with specialised instruments like coronagraphs, introduced by the French astronomer Lyot (1931), which artificially obscure the disk of the Sun as seen in Fig. 2.6.b and referred to as the “white-light corona”. The dominance of the strong magnetic field on the solar corona ($\beta \ll 1$) exhibits various dynamic features such as filaments, loops, and streamers, which are formed due to the complex interplay between the magnetic field and the plasma in this atmosphere (Aschwanden, 2004).

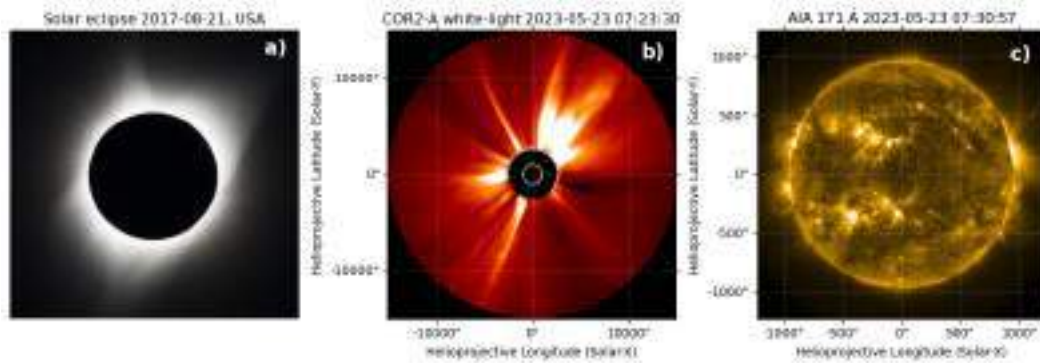


Fig. 2.6: Three different ways to observe the solar corona. Left: solar corona observed during a total solar eclipse on August 21, 2017, above Madras, Oregon, USA. Credits: NASA/Aubrey Gemignani; published on October 11, 2022. Center: solar corona observed using a coronagraph to create an artificial eclipse. Image taken by the STEREO-A SECCHI's Cor2 coronagraph. Right: Solar corona emits in the range of EUV and SXRs which can be observed using space telescopes. Image taken by SDO/AIA 171 Å.

First observations aimed at determining the solar corona’s temperatures were made by Grotian (1939) and Edlén (1945). Eldén demonstrated that strong emission lines from the corona, specifically those associated with Fe X and Fe XIV at wavelengths of $\lambda = 6375 \text{ \AA}$ and $\lambda = 5303 \text{ \AA}$ respectively, require a highly energetic process to ionise iron atoms (Brooks et al., 2011). These ionisation processes are an indicator of temperatures reaching at least 1 MK, thereby suggesting that the plasma particles reach average thermal energies spanning from 0.1 kiloelectronvolt (keV) to 1 keV. This energy range corresponds to the wavelengths between 10 – 100 Å, enclosing the Extreme Ultraviolet (EUV) and Soft-X Ray (SXR) spectral regions (e.g. Fig. 2.6.c). These emission lines are diagnostic of the physical conditions in the corona, and their analysis provides insights into the plasma properties, such as temperature, density, and composition (Del Zanna et al., 2023).

The study of the solar corona is crucial for understanding the dynamic behaviour of the Sun and its impact on space weather. Solar eruptions originating in the corona eject ionised plasma into the interplanetary space causing geomagnetic storms which can disrupt satellite communications, power grids, and navigation systems on Earth (Webb et al., 2009). Moreover, the corona acts as a laboratory for investigating fundamental plasma physics, such as magnetic reconnection, high energy particle

acceleration (Harra, 2000), and solar flares (Shibata and Magara, 2011), which have broader implications across astrophysical systems (Priest and Forbes, 2002; Benz, 2017).

Space-based observatories provide high-resolution images, detailed spectra, and continuous monitoring of solar dynamic behaviour and evolution, in particular, at EUV and SXR wavelengths which are not accessible from Earth. Some of the most utilised spacecrafts comprise the Solar and Heliospheric Observatory (SoHO) with specialised instruments like the Extreme ultraviolet Imaging Telescope (EIT) and the Large Angle and Spectrometric Coronagraph (LASCO), the Transition Region and Coronal Explorer (TRACE), the Hinode mission with its onboard X-Ray Telescope (XRT) and the Extreme-ultraviolet Imaging Spectrometer (EIS) instruments, and the SDO with its AIA instrument (Domingo et al., 1995; Handy et al., 1999; Kosugi et al., 2007; Pesnell et al., 2012). These missions have improved our knowledge and understanding of the coronal heating mechanisms, magnetic field evolution and reconnection, and the physics behind eruptive events.

In summary, the solar corona, with its intricate structures, intense magnetic dynamics, and extreme temperatures, remains an intriguing subject of scientific research. Through a multidisciplinary approach encompassing observations, modelling, and theory, researchers continue to unravel its questions, shedding light on the fundamental processes that govern our dynamic Sun.

2.2.5 Active Regions and their Dynamics

It has been established that sunspots are large concentrations of magnetic field sufficiently strong to suppress convective processes on the photosphere, decreasing the efficiency to transport the convective energy leading to a temperature reduction to approximately 3500 K, causing sunspots to appear darker in comparison to the surrounding photosphere. Understanding the formation of these magnetic features requires an exhaustive and detailed investigation of the theoretical view of the fundamental processes of convection and the emergence of magnetic flux tubes (Solanki, 2003; Foukal, 2013). The general concept behind the sunspot formation involves the buoyancy of magnetic flux tubes retaining sufficiently strong magnetic fields within the subsurface convection zone (see Fig. 2.7). These flux tubes gradually rise towards the solar surface until they penetrate through the surface. At this moment and location, the magnetic flux starts to form initial solar pores, which are characterised by a decrease in surface brightness (Cheung and Isobe, 2014). Sunspots are described by two fundamental components, a dark inner core known as the umbra, characterised by strong, predominantly vertical magnetic fields, and a brighter, filamentary region surrounding the dark core named penumbra. In the penumbra, the magnetic fields become progressively weaker and more horizontal as they move away from the umbra (Thomas, 2010; Jurčák et al., 2018).

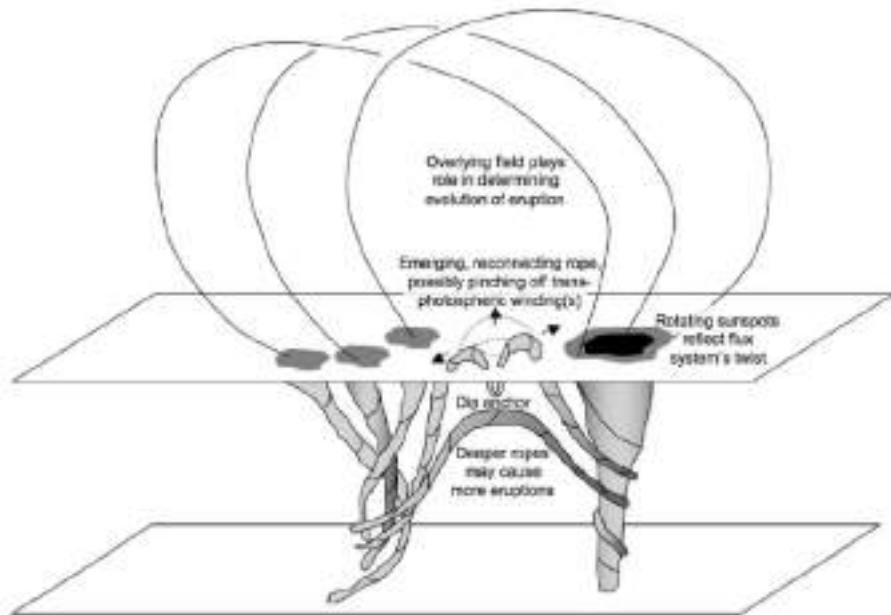


Fig. 2.7: Sketch representing the emergence of magnetic field and formation of solar ARs (Schrijver, 2009).

Umbra: The umbra constitutes the central dark region of a sunspot, where the temperatures are lower compared to its surrounding ranging from around 3500 to 5000 K. This discrepancy takes place due to the suppression of energy transport facilitated by the presence of strong magnetic fields within this region. The reduced relative plasma velocity into the umbra leads to a significant decrease in convective plasma motions underneath these regions (Chitre and Shaviv, 1967). In particular, larger sunspots with more extensive areas are characterised by having larger magnetic field strengths, reaching values up to >3500 Gauss (Solanki, 2003). Although the umbra is typically considered as a simple structure, advanced high-resolution observations have revealed a more intricate reality within the umbral region of sunspots. Contrary to a simplistic conception of a dark and uniform entity, several authors have unveiled many fine-scale bright features populating the umbral region, including the so-called umbral dots (Bharti et al., 2007; Riethmüller et al., 2008; Sobotka and Puschmann, 2009).

Penumbra: The penumbra is the outer ring-shaped region surrounding the umbra in sunspots. When the penumbra does not exist around the umbra, it is called a solar pore. Interestingly, umbra can exist without a penumbra. The opposite situation can also occur, where penumbrae are present without a hosting umbra; these cases are commonly known as orphan penumbrae (Jurčák et al., 2014). The penumbra presents a radial filamentary structure, characterised by being darker than the granular environment but less dark than the umbra (del Toro Iniesta, 2001; Solanki, 2003).

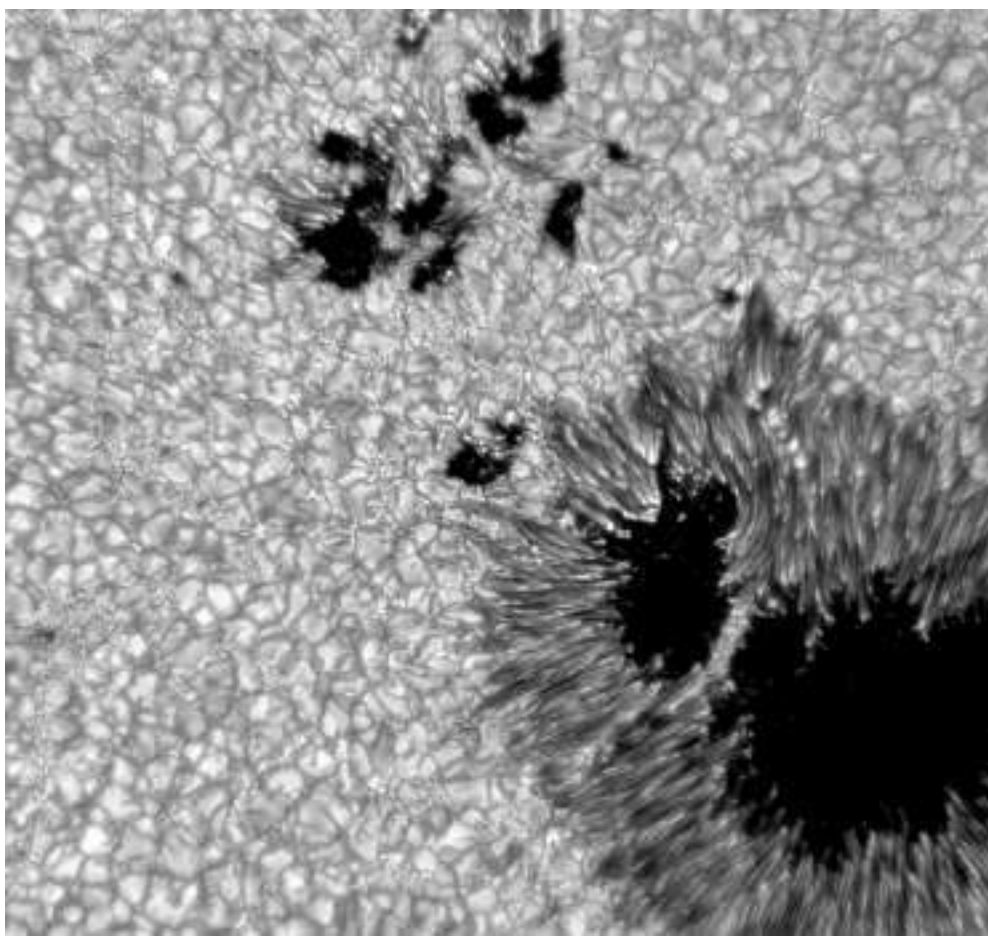


Fig. 2.8: High-resolution images display the complex structures for sunspots, where more fine features within the umbra and penumbra of a sunspot can be detected. Image taken with the New Solar Telescope (NST) using the TiO band (7057 Å. Date: 2010-0927 17:2539 UT. Credits of NJIT/Big Bear Solar Observatory, <http://www.bbso.njit.edu/Archive/>)

The penumbra is responsible for a significant portion of the sunspot's total magnetic flux. Figure 2.8 displays that sunspots are complex dynamic structures in the photosphere with multiple small-scale magnetic elements evolving within them.

The lifetime evolution of sunspots can be summarised in three main stages: formation, stability, and decaying phase. Chapter 3 (paper #1) represents a study of three active regions during the emergence and formation stage. Basically, with the formation of the first concentrations of magnetic flux, the brightness decreases, and the first solar pores appear on the surface. It is worth clarifying that not all solar pores evolve into sunspots. During the emergence of the magnetic flux, it can form isolated pores that evolve independently during hours, or they can also exist within large ARs, but they do not develop a penumbra. While the magnetic flux continues accumulating, the structure becomes larger leading to the formation and appearance of sunspots; see Fig. 2.8 & 2.9. Once sunspots are formed, the magnetic and gas pressure evolve until reaching equilibrium at the interface (Meyer et al., 1977; Strecker et al., 2021).

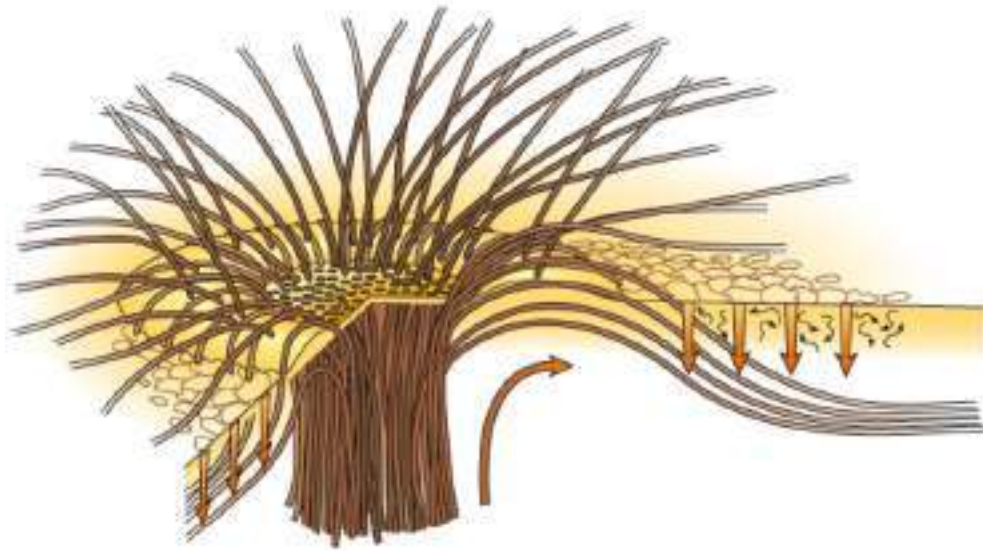


Fig. 2.9: Artistic representation of the magnetic field lines structure in a sunspot determined from observations and simulations (Thomas, 2010). The illustration displays the different configurations of the magnetic field lines within the umbra and penumbra.

According to Jurčák et al. (2018), an empirical criterion to determine when a sunspot is stable is when the vertical magnetic field reach values of 1849–1885 G. During this stage, their lifetimes span between a few hours up to several days, and exceptionally several weeks, depending on their sizes (surface area), morphology, the amount of magnetic flux and its configuration. The last stage is the decaying phase of the sunspot or active region when the magnetic flux starts to dissipate, and its area begins to shrink. Various physical mechanisms are involved during the decay stage, including diffusion processes due to the fragmentation of the penumbra and the umbra that spread the flux of the sunspot over a larger area, flux cancellation of moving magnetic features (MMFs), and flux transport by MMFs to the outer parts of sunspot dissolving the structure (see: Stix, 2002; Martínez Pillet, 2002; Deng et al., 2007; Sheeley et al., 2017).

2.2.6 Small-scale magnetic fields

Different studies of the solar photosphere have revealed an incredible amount of fine magnetic fine structures, mainly corresponding to Magnetic Bright Points (MBPs), which are small-scale magnetic features associated with high magnetic field strengths on the order of up to kilogauss (Beck et al., 2007; Utz et al., 2013; Keys et al., 2019), sizes in the range of 100 to 300 km, lifetimes of ~ 5 minutes, and detected horizontal velocities between 0.2 to 5 km/s (for more details see Sánchez Almeida et al., 2004; Utz et al., 2009; Liu et al., 2018, and references in there). MBPs represent a very important topic in solar physics because they are found all over the photosphere, both in quiet and active regions of the Sun, and they are present all the time on

the surface. MBPs particularly move and accumulate in the intergranular lanes in between granular convective cells (e.g., Muller et al., 1989).

Observations have revealed that using CH and CN molecular lines alongside specific spectral wavelengths highlights the magnetic bright points (Mallia, 1968; Schüssler et al., 2003). The 4308 Å broad spectral band (designated “G-band” by the German physicist Joseph von Fraunhofer) is the best spectral band to observe the MBPs which increases the contrast in G-band filtergrams (e.g., Fig. 2.8) due to a reduced abundance of CH lines that weaken the CH lines, allowing more of the continuum "brightness" to pass through (Rutten et al., 2001). It is widely utilized in spectroscopic investigations due to its high capability to detect the MBPs from the surrounding granulation compared to continuum images in other spectral bands (Steiner et al., 2001).

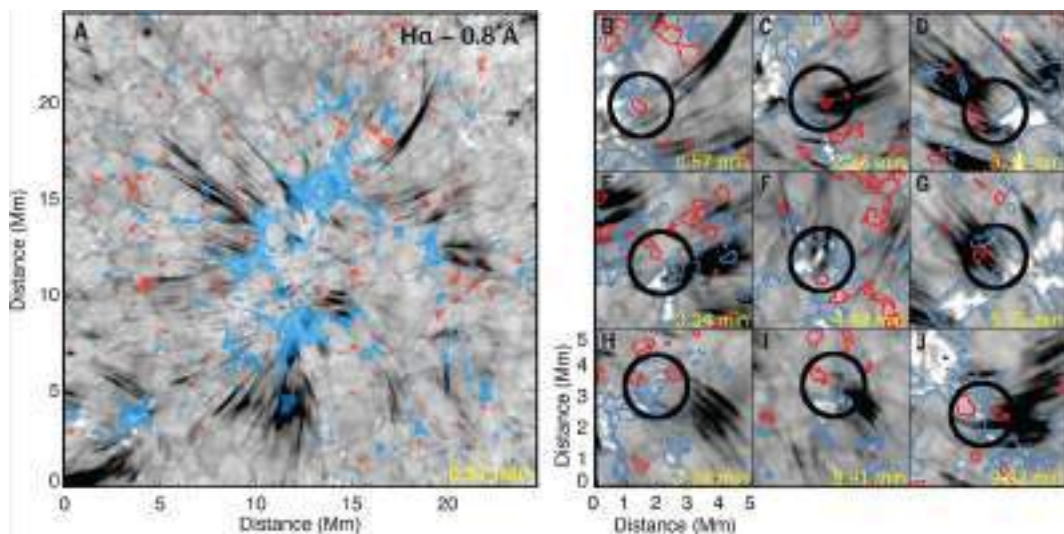


Fig. 2.10: Association of enhanced spicular activity with a magnetic field structures. Left: Dark contrast features in $\text{H}\alpha$ blue wing image (A) represent the jets-like spicules. Right: Timestamps (B-J) display enhanced spicules overlaying magnetogram with blue and red contours for positive and negative polarity, respectively. From Samanta et al. (2019).

Consequently, the study of MBPs has gained substantial interest, particularly in light of the rapid advancement in high-resolution instrumentation (see section 2.3). One of the unresolved issues in solar astrophysics is the coronal heating problem. Various hypotheses have been proposed, including the involvement of spicules, small structures that transport mass from the lower chromosphere to higher layers. One suggested mechanism for spicule creation involves small-scale magnetic structures such as MBPs and the reconnection of magnetic field lines, which could generate sufficient energy for the formation of these jets (de Pontieu et al., 2007; Samanta et al., 2019).

2.3 High-Resolution Observations and Imaging Techniques

Since Galileo Galilei started to use the telescope to register observations of the Sun, many scientists have been working on the development of new instruments and techniques to improve the understanding of our host star. Like in almost all fields of science, every time scientists solve a previous limitation, new problems appear, challenging the creativity and innovation of solar astronomers. During this endeavour, the scientific community succeed to launch telescopes into space extending the capabilities to observe in other wavelengths which could not be observed from Earth due to the presence of our atmosphere (see Fig. 2.11).

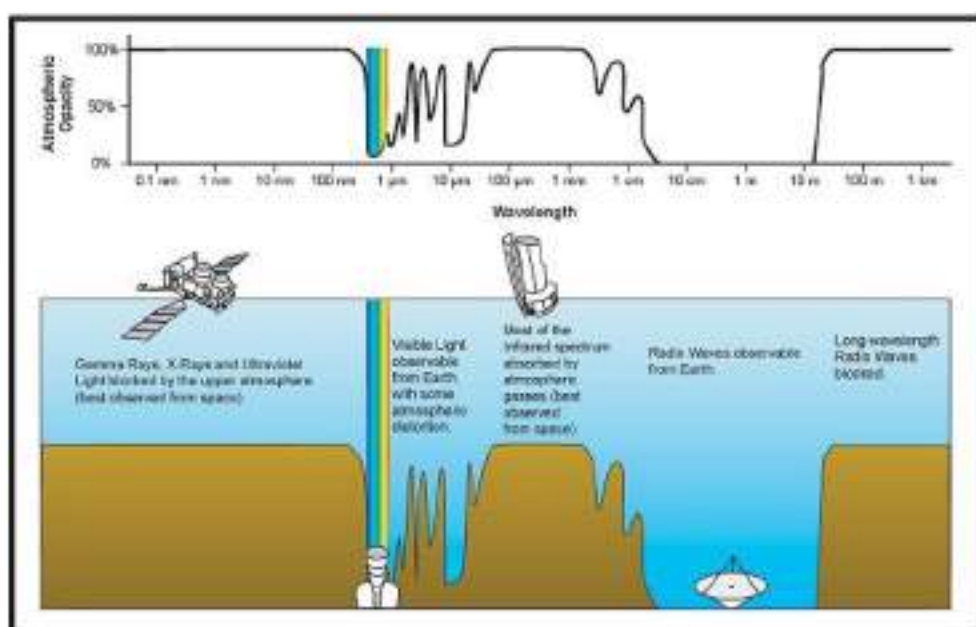


Fig. 2.11: Image representing the wavelength bands in which photons can penetrate the Earth's atmosphere. Such bands are commonly named “observational windows”, which comprise the visible spectrum window from 380 nm to 750 nm, i.e. from violet to red (Sliney, 2016). In addition, it includes various infrared (IR) windows and the radio waves window. Image from http://coolcosmos.ipac.caltech.edu/cosmic_classroom/ir_tutorial/irwindows.html

This remarkable progress can be attributed to the advancements in telescope technology, space technology, observing techniques, camera systems, computational technology, and many others. These innovations have collectively facilitated significant growth in our understanding of fundamental physical processes such as convection, magnetic field structure, and the interaction between plasma and magnetic fields, using observations of the Sun at an ever-higher resolution, spatially, temporally, and spectrally. The last two decades have been characterised by a revolution in development of space and ground-based telescopes such as the renewed Swedish 1-m Solar Telescope (SST; Scharmer et al., 2003) and the new CRisp

Imaging SpectroPolarimeter (CRISP; Scharmer et al., 2008) installed at the SST in 2008, the Interferometric Bidimensional Spectrometer (IBIS; Cavallini and Reardon, 2006) installed at the Richard B. Dunn Solar Telescope (DST) in 2003, the Hinode spacecraft launched in 2006 and its SOT instrument, the Goode Solar Telescope (GST; Goode et al., 2010), the SDO spacecraft with its HMI and AIA instruments launched on February 2010, and the GREGOR 1.5 m solar telescope Schmidt et al. (2012) and its instruments, the GREGOR Infrared Spectrograph (GRIS; Collados et al., 2012) and the HiFI instrument (Denker et al., 2018). The most recent advances in telescopes, instruments, and detectors include the Parker Solar Probe (Fox et al., 2016), the Solar Orbiter mission (Müller et al., 2020), as well as the ground-based 4-meter Daniel K. Inouye Solar Telescope (DKIST; Rimmele et al., 2020), located on Haleakala, Maui, Hawaii.

As with all the instruments mentioned, the choice of observational data obtained from either space- or ground-based telescopes depends on their respective advantages or disadvantages. Various factors need to be taken into consideration, such as the data quality itself, costs, telescope size, accessibility to the data, and many others. Space-based missions have the evident advantage of providing observations free of the Earth's atmosphere spectral limitations, giving access to the full electromagnetic spectrum (e.g. Fig. 2.11), and free of perturbations due to the turbulence and other thermal variations (“seeing”; Masson, 1994), but the aperture and size of the spacecraft are limited directly by the rocket used to carry them into orbit. They are also restricted by the telemetry capacity for data acquisition, and usually, they are considerably more expensive than the ground-based telescopes facilities. On the other hand, ground-based telescopes offer the advantage of being only size-limited by available funding, and they allow for easier upgrades and adaptations to evolving scientific needs and new capabilities. However, they face the challenge of location constraints like variable atmosphere conditions that can degrade the quality of the observed data. As a consequence of the presence of the seeing, the incoming adjacent rays of light follow different paths and result in the perturbation of initially parallel wavefronts, causing clear effects like blurring, deformation, and displacement of the collected images. Because of these limitations, the adaptive optics (AO) system has become an essential tool employed to correct atmospheric distortions in real-time, allowing for sharper and more detailed images (Hardy, 1998).

2.3.1 Adaptive Optics (AO) system

The main purpose of an Adaptive Optics (AO) system is to correct wavefront aberrations caused by the turbulent atmosphere above the telescope (Tyson and Hart, 2011). Turbulent motions in the atmosphere create vortices with varying temperatures and densities, leading to fluctuations in the refractive index as light propagates

through the turbulent medium, causing deformations in the incoming wavefronts.

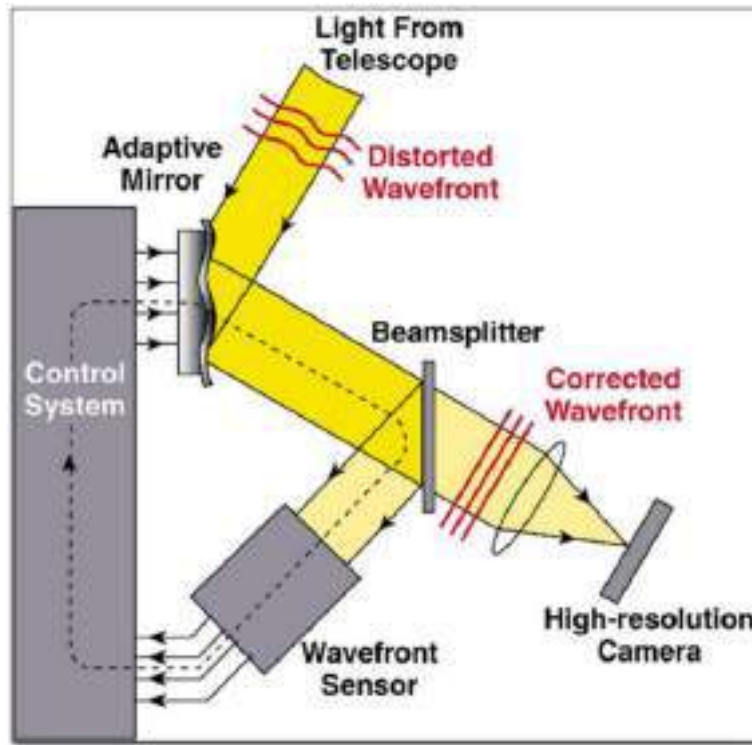


Fig. 2.12: Sketch describing the basic principles of the AO system. The deformable mirror moves to reconstruct the wavefront deformed by the seeing atmosphere. Image from (Rimmele and Marino, 2011)

The design and performance requirements of an AO system include the Fried parameter r_0 or coherence length which measures the optical transmission quality through the atmosphere, the Greenwood frequency f_c which depends on the turbulence and wind speed in the atmosphere, and the atmospheric turbulence profile $C_n^2(h)$ (e.g., Mao et al., 2023). The Kolmogorov model (Kolmogorov, 1991) is the most widely adopted model for describing atmospheric turbulence which takes into account the energy introduced into the system through wind flows at a large scale which cascades down to smaller scales until it is eventually dissipated at molecular scales. The range between the larger (outer) scales and molecular (inner) scales, is characterised by the turbulent power of temperature fluctuations Φ_T as a function of the spatial wavenumber $\kappa = 2\pi/l$, as follows,

$$\Phi_T(\kappa) \propto \kappa^{-\frac{5}{3}}. \quad (2.3)$$

Figure 2.12 shows a simplified diagram of how AO systems work. The three main components of any AO setup are the wavefront sensor (WFS) which measures the wavefront distortions by sensing gradients at different positions on a plane, the wavefront corrector (WFC), or deformable mirror which is responsible for correcting

the differences caused by the phase aberrations, and finally, the processing unit which computes the WFS information and modulates the motions of the deformable mirror. This arrangement enables the recovery of the image information before the deformation caused by the turbulent atmosphere. Among the AO systems, there are various configurations including the DST AO76 (Rimmele, 2004), the Kiepenheuer Institute AO system (KAOS; von der Lühe, 2003) used by the Vacuum Tower Telescope (VTT), Multi-Conjugate AO system (MCAO; Rigaut et al., 2000) implemented at the GREGOR telescope, and the Ground Layer AO (GLAO; Ren et al., 2015) tested by Rimmele et al. (2010) with the National Solar Observatory DST. Since the reconstruction of the wavefront by the AO is not perfect, a post-processing stage is necessary after the data acquisition.

2.3.2 Solar Image Reconstruction

Adaptive optics systems reduce significantly the aberrations caused by the Earth's atmosphere, but the remaining high-order distortions must be minimised by post-processing methods and techniques. There are multiple methods of image reconstruction, among the two most widely used are the Speckle imaging and the Multi-Frame Blind Deconvolution (MFBD) methods.

The **Speckle imaging** variants include the speckle interferometry (von der Lühe, 1993; Wöger et al., 2008), and the phase-diversity and phase-diverse speckle (Löfdahl and Scharmer, 1994; Valenzuela et al., 2010). The principle of the speckle method is to reconstruct the complex Fourier transform of the image from separate amplitudes and phase of a statistical sample of the seeing, applied to 100 short exposure frames (Labeyrie, 1970; von der Lühe, 1984). Because the low-contrast features are typical in solar observations, multiple improvements have been applied and adapted accordingly with the telescopes and instruments properties (e.g., sTools for the HiFI instrument mounted in GREGOR; Kuckein et al., 2017).

The **MFBD** method (Schulz, 1993; van Kampen and Paxman, 1998; Scharmer et al., 2010) and the modified version named Multi-Object Multi-Frame Blind Deconvolution (MOMFBD; Van Noort et al., 2005) estimate both an unknown object convolved with an unknown point spread function (PSF). This is an unstable problem because an uncountable number of PSF/object combinations exist, and multiple solutions for a given observation. Various constraints are introduced into the method, such as the PSF related to the telescope, and the use of multiple frames (minimum images ~ 5), to help obtain a more unique solution.

Nowadays, using a different machine and deep learning techniques, new improvements in image restoration methods have started to emerge in this field (e.g. Asensio Ramos et al., 2023).

A deeper description of the different classical restoration techniques is beyond the scope of this thesis, but we encourage the readers to the review Löfdahl et al. (2007) and the other references mentioned here.

2.3.3 Proper Motions

Proper motion refers to the astrometric measurement of the changes in the apparent position of astronomical objects (stars, planets, galaxies, and so on) on the celestial sphere. Although several authors conducted studies to calculate apparent motion on the Sun (Leighton et al., 1962; Noyes and Leighton, 1963; Simon and Leighton, 1964; Simon, 1967), the most widely accepted method used to compute flow fields on the solar surface is the local correlation technique (LCT) algorithm applied for the first time by November and Simon (1988). The LCT algorithm is built upon a fundamental yet robust concept of "maximising" and identifying the optimal local alignment between two consecutive images. A proper motion is defined as the displacement that maximises the spatially localised cross-correlation between the two consecutive images $J_t(\mathbf{x})$ and $J_{t+\tau}(\mathbf{x})$ with a temporal separation t and $t + \tau$ using an apodisation window $W(\mathbf{x})$ (usually a Gaussian window). The cross-correlation displacement function is given by:

$$C(\delta, \mathbf{x}) = \int J_t\left(\zeta - \frac{\delta}{2}\right) J_{t+\tau}\left(\zeta + \frac{\delta}{2}\right) W(x - \zeta) d\zeta, \quad (2.4)$$

where δ is the displacement vector (dx, dy) , whereas \mathbf{x} is the two-dimensional central point (x, y) .

The application of different LCT methods, or other techniques to calculate the apparent motions, needs to consider several pre-processing steps like co-alignment, subsonic filtering of the natural frequencies of the p-modes or 5 minutes oscillations (Title and Tarbell, 1986), shrinking effect corrections (Lisle and Toomre, 2004), and rotation, among others. Also, other post-processing steps must be followed to obtain good results such as de-projection when the observations are far from the disk center.

Proper motion tracking techniques have been developed and applied to detecting the apparent dynamics of the magnetic elements, driving the implementation of new techniques such as the inductive local correlation tracking (ILCT; Welsch et al., 2004), which basically introduces the normal component of induction equation and uses the LCT output velocities as an ansatz ensuring the consistency of the calculated apparent motions in magnetograms. Magnetic elements, such as sunspots and magnetic loops, exhibit complex motion patterns that can be characterised and quantified through proper motion measurements. By analysing the apparent motions of these magnetic features, scientists can gain insights into the mechanisms driving their formation, evolution, and dissipation. This knowledge contributes to

our understanding of the solar dynamo, which is responsible for generating the Sun's magnetic field.

Other types of algorithms have been developed for the detection of proper motions on intensity images as well as on magnetograms. Among the most used tracking techniques, we have the Coherent Structure Tracking (CST; Roudier et al., 1999), which uses segmentation of the intensity images and detects coherent structures to subsequently track them, and the ball-tracking technique (BT; Potts et al., 2004), which, in principle, introduces floating balls on the intensity images that follow the average motion of the continuum changes and the granules. In the case of tracking magnetic element motions, the most sophisticated technique is perhaps the differential affine velocity estimator (DAVE; Schuck, 2006) technique, which basically minimises the magnetic induction equation restrained by a completely affine velocity profile.

In recent years, advancements in observational techniques, image processing, and data analysis have expanded the capabilities of proper motion studies in solar physics. Different investigations have been conducted using these different techniques to infer the dynamics and connection between the apparent motions of the solar plasma and the Sun's magnetic field. Furthermore, deep learning algorithms have been also developed to infer horizontal proper motions in the solar photosphere (see Díaz Baso and Asensio Ramos, 2018).

2.4 Space and ground-based telescopes

During the course of this research, we utilised various data products from different telescopes and instruments, each of which will be comprehensively described in the subsequent sections.

2.4.1 Helioseismic and Magnetic Imager (HMI)

The SDO spacecraft was launched on February 11, 2011. This mission includes three scientific instruments: the AIA, the HMI and the Extreme Ultraviolet Variability Experiment (EVE; Woods et al., 2012). A scheme of the SDO spacecraft and its instrument payload is shown in Fig. 2.13.

The HMI instrument is designed to investigate the dynamics of the convection zone, the solar interior oscillations, the solar variability, and the evolution of the different magnetic field activity. HMI produces full-disk observations in the Fe I absorption line at $6173.3 \pm 0.1 \text{ \AA}$ with an optical resolution of $\sim 1 \text{ arcsecond}$. Figure 2.14 shows all the components included in the instrument. The main components are the refractor telescope with a clear aperture of 14 cm, a polarization selector, a narrow band tuneable filter, and two CCD cameras of $4096 \times 4096 \text{ pixels}^2$ and a detector

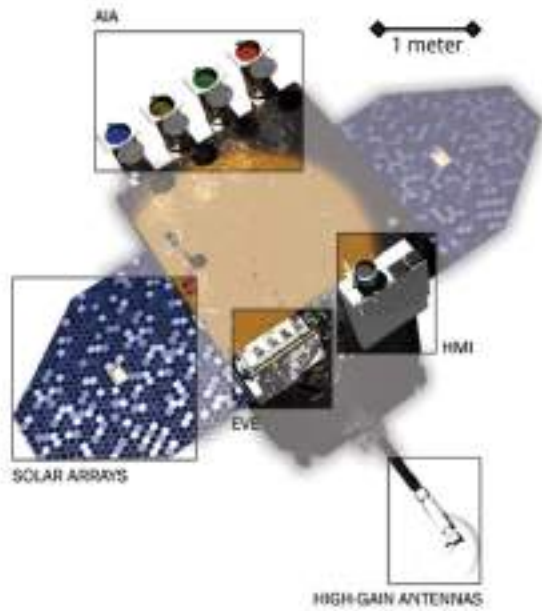


Fig. 2.13: Instruments mounted on the SDO mission, with a measurement scale referring to the real size of the spacecraft.

resolution of ~ 0.504 . One camera is dedicated to a 45 second cadence Doppler and LOS field sequences, meanwhile, the other camera is dedicated to a 90 second cadence vector field sequences.

The basic data products obtained from the HMI instrument are the Dopplergrams, continuum brightness proxy (intensity filtergrams), LOS magnetic flux images, and vector magnetic field maps. The three first mentioned are available at a 45 seconds cadence, whereas each vector magnetic field map is an array of 24 images consisting of six spectral wavelength points and the four Stokes parameters (IQUV) averaged over 12 minutes. Additionally, in the Joint Science Operation Center (JSOC¹), derived data from the Milne-Edington inversion of the Stokes parameters, and the proper disambiguated vector magnetic field maps are inferred and stored in the data center. The continuous, long-term and full-disk observations of HMI, allow us to observe different solar features with duration of several hours, days or even months for long-lived Active Regions to study their evolution and behaviour.

2.4.2 Solar Optical Telescope (SOT)

The Hinode satellite (Solar-B) led by the Institute of Space and Astronautical Science of the Japan Aerospace eXploration Agency (ISAS/JAXA) was launched on September 22, 2006. The Hinode mission is comprised of three scientific instruments onboard: the EUV Imaging Spectrometer (EIS; Culhane et al., 2007), the X-Ray Telescope (XRT; Golub et al., 2007) and the Solar Optical Telescope (SOT; Tsuneta et al., 2008b).

¹ <http://jsoc.stanford.edu>

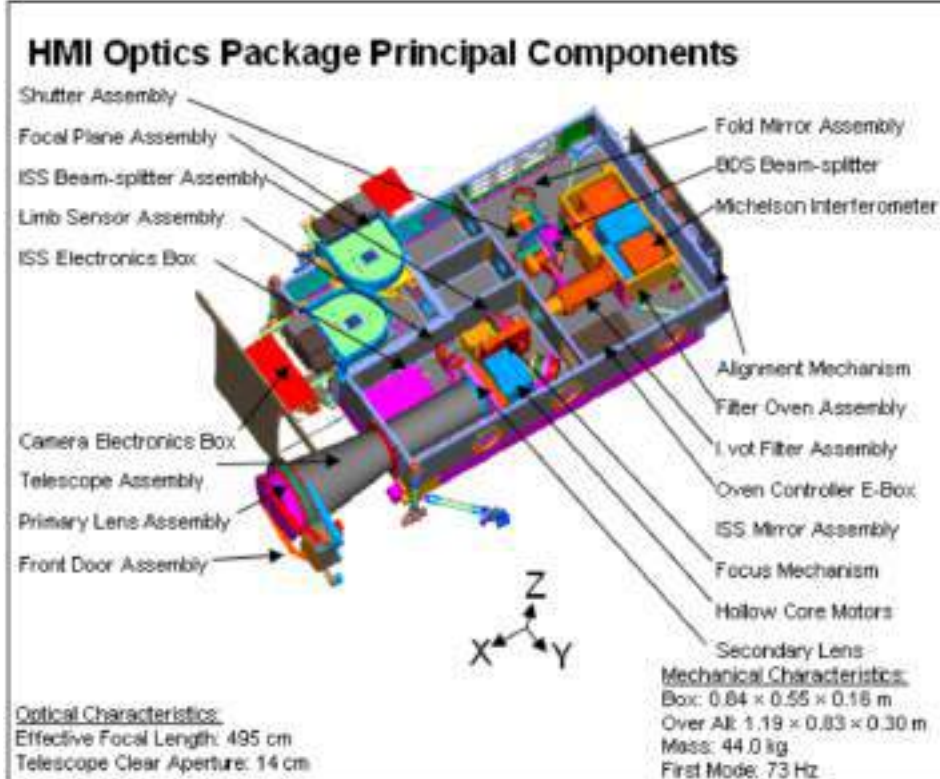


Fig. 2.14: Sketch of the composition of the HMI instrument.

The SOT consists of the main telescope with an aperture of 50 cm or optical telescope assembly (OTA), and the focal plane package (FPP) which includes the SpectroPolarimeter (SP) with a region of interest of 320×151 arcseconds with a spatial sampling of 0.16 arcseconds per pixel, the Narrow-band Filter Imager (NFI) covering an area of 328×164 arcseconds with a spatial sampling of 0.08 arcseconds/pixel and the Broad-band Filter Imager (BFI) with a maximum FOV of 218×109 arcseconds and a spatial sampling of 0.053 arcseconds/pixel. The BFI and NFI combined cover observations from the lower photosphere (including G-band observations) up to the chromosphere (e.g., Ca II K line), whereas the SP instrument provides high spectral resolution in all Stokes parameters in two magnetically sensitive lines of Fe I at 6302 \AA . The SOT goals are focused on open scientific questions related to local helioseismology, local and global dynamo, flux tube nature, magnetic field evolution, and magnetic reconnection, among others. Its high-resolution observations makes it also well suited to study small-scale magnetic structures such as MBPs.

2.4.3 GREGOR and the High-resolution Fast Imager

The GREGOR 1.5 m solar telescope is the largest solar telescope based in Europe, located at the Observatorio del Teide on the Canary Islands, Spain. The main science aims include the understanding of the interaction between plasma convective

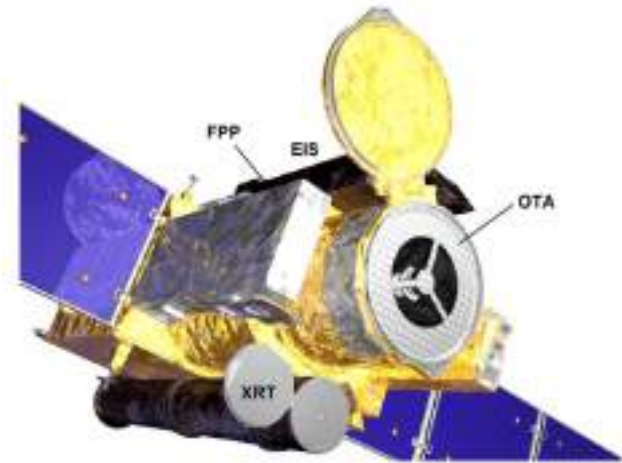


Fig. 2.15: Diagram of the location of the different instruments onboard of the Hinode spacecraft.

granulation and the magnetic field on the solar surface, the study of fine structures and features in ARs, the investigation of the role of local and global solar magnetism in the solar variability, among others (Schmidt et al., 2012; Kleint et al., 2020).

As it was mentioned in Sec. 2.3, one of the advantages of the ground-based telescopes is the possibility to update and improve the telescopes and instruments. GREGOR has multiple instruments installed, such as the Broad-Band Imager (BBI), the GREGOR Fabry Pérot Interferometer (GFPI), the GRating Infrared Spectrograph (GRIS), and the recently upgraded HiFI+ (Denker et al., 2023). The upgrade consists of three cameras with two synchronised sCMOS (16-bit digitisation) or CMOS² (12-bit digitisation) detectors each. HiFI+ offers near-diffraction limited imaging at high cadence in six spectral windows. The first camera (HiFI+ 1) takes images in the G-band at 4307 Å and the blue continuum at 4506 Å. This camera covers an area on the solar surface of 70.7×59.6 arcseconds (2560×2160 pixels), with an average time cadence of 20 seconds using Speckle masking or MOMFBD restoration to obtain the best image. The HiFI+ 2 camera captures images in the H α line center at 6563 Å with a FOV of 76.5×60.5 arcseconds or 1536×1216 pixels, with high time cadence imaging of 6 seconds using the MOMFBD restoration method. The HiFI+ 3 camera takes images in the Ca II H line at 3968 Å and TiO band centered at 7057 Å, covering a region of 48.2×30.8 arcseconds (1536×1216 pixels) and 76.5×60.5 arcseconds (1536×1216 pixels), respectively. After the image selection and applying the Speckle masking image restoration, the time cadence obtained by the HiFI+ 3 is 6 seconds. Due to the high spatial and temporal resolution of this instrument, it is suitable for the study of small-scale magnetic flux tubes as observed in the form of MBPS, and to analyse their temporal evolution during their short lifetimes.

² CMOS sensor: Complementary Metal Oxide Semiconductor sensor. sCMOS: scientific CMOS

Bibliography

- Aschwanden, Markus J. (2004). *Physics of the Solar Corona. An Introduction* (cit. on pp. 8, 13).
- Asensio Ramos, A., S. Esteban Pozuelo, and C. Kuckein (June 2023). „Accelerating Multiframe Blind Deconvolution via Deep Learning“. In: *arXiv e-prints*, arXiv:2306.12078, arXiv:2306.12078. DOI: [10.48550/arXiv.2306.12078](https://doi.org/10.48550/arXiv.2306.12078). arXiv: [2306.12078 \[astro-ph.IM\]](https://arxiv.org/abs/2306.12078) (cit. on p. 22).
- Balmer, J. J. (Jan. 1885). „Notiz über die Spectrallinien des Wasserstoffs“. In: *Annalen der Physik* 261.5, pp. 80–87. DOI: [10.1002/andp.18852610506](https://doi.org/10.1002/andp.18852610506) (cit. on p. 10).
- Beck, C., L. R. Bellot Rubio, R. Schlichenmaier, and P. Sütterlin (Sept. 2007). „Magnetic properties of G-band bright points in a sunspot moat“. In: *A&A* 472.2, pp. 607–622. DOI: [10.1051/0004-6361:20065620](https://doi.org/10.1051/0004-6361:20065620). arXiv: [0707.1232 \[astro-ph\]](https://arxiv.org/abs/0707.1232) (cit. on p. 17).
- Benz, Arnold O. (Dec. 2017). „Flare Observations“. In: *Living Reviews in Solar Physics* 14.1, 2, p. 2. DOI: [10.1007/s41116-016-0004-3](https://doi.org/10.1007/s41116-016-0004-3) (cit. on p. 14).
- Bharti, Lokesh, Rajmal Jain, and S. N. A. Jaaffrey (Aug. 2007). „Evidence for Magnetoconvection in Sunspot Umbral Dots“. In: *Astrophysical Journal* 665.1, pp. L79–L82. DOI: [10.1086/521024](https://doi.org/10.1086/521024) (cit. on p. 15).
- Brandenburg, Axel and Kandaswamy Subramanian (Oct. 2005). „Astrophysical magnetic fields and nonlinear dynamo theory“. In: *Physics Reports* 417.1-4, pp. 1–209. DOI: [10.1016/j.physrep.2005.06.005](https://doi.org/10.1016/j.physrep.2005.06.005). arXiv: [astro-ph/0405052 \[astro-ph\]](https://arxiv.org/abs/astro-ph/0405052) (cit. on p. 6).
- Brooks, David H., Harry P. Warren, and Peter R. Young (Apr. 2011). „EUV Spectral Line Formation and the Temperature Structure of Active Region Fan Loops: Observations with Hinode/EIS and SDO/AIA“. In: *Astrophysical Journal* 730.2, 85, p. 85. DOI: [10.1088/0004-637X/730/2/85](https://doi.org/10.1088/0004-637X/730/2/85). arXiv: [1101.5240 \[astro-ph.SR\]](https://arxiv.org/abs/1101.5240) (cit. on p. 13).
- Cavallini, F. and K. Reardon (Jan. 2006). „IBIS instrumental characteristics and first results“. In: *Memorie della Società Astronomica Italiana Supplementi* 9, p. 55 (cit. on p. 20).
- Charbonneau, Paul (Aug. 2014). „Solar Dynamo Theory“. In: *Annual Review of A&A* 52, pp. 251–290. DOI: [10.1146/annurev-astro-081913-040012](https://doi.org/10.1146/annurev-astro-081913-040012) (cit. on p. 6).
- Cheung, Mark C. M. and Hiroaki Isobe (July 2014). „Flux Emergence (Theory)“. In: *Living Reviews in Solar Physics* 11.1, 3, p. 3. DOI: [10.12942/lrsp-2014-3](https://doi.org/10.12942/lrsp-2014-3) (cit. on pp. 6, 14).
- Chitre, S. M. and G. Shaviv (Sept. 1967). „A Model of the Sunspot Umbra“. In: *Solar Physics* 2.2, pp. 150–157. DOI: [10.1007/BF00155915](https://doi.org/10.1007/BF00155915) (cit. on p. 15).

- Collados, M., R. López, E. Páez, et al. (Nov. 2012). „GRIS: The GREGOR Infrared Spectrograph“. In: *Astronomische Nachrichten* 333.9, p. 872. DOI: [10.1002/asna.201211738](https://doi.org/10.1002/asna.201211738) (cit. on p. 20).
- Cook, J. W., P. A. Lund, J. -D. F. Bartoe, et al. (1987). „Statistical Properties of Small High-Velocity Events in the Solar Transition Region“. In: *Cool Stars, Stellar Systems and the Sun*. Ed. by J. L. Linsky and R. E. Stencel. Vol. 291, pp. 150–153. DOI: [10.1007/3-540-18653-0_122](https://doi.org/10.1007/3-540-18653-0_122) (cit. on p. 12).
- Culhane, J. L., L. K. Harra, A. M. James, et al. (June 2007). „The EUV Imaging Spectrometer for Hinode“. In: *Solar Physics* 243.1, pp. 19–61. DOI: [10.1007/s01007-007-0293-1](https://doi.org/10.1007/s01007-007-0293-1) (cit. on p. 25).
- de Pontieu, Bart, Scott McIntosh, Viggo H. Hansteen, et al. (Nov. 2007). „A Tale of Two Spicules: The Impact of Spicules on the Magnetic Chromosphere“. In: *Publications of the Astronomical Society of Japan* 59, S655. DOI: [10.1093/pasj/59.sp3.S655](https://doi.org/10.1093/pasj/59.sp3.S655). arXiv: [0710.2934 \[astro-ph\]](https://arxiv.org/abs/0710.2934) (cit. on pp. 11, 18).
- del Toro Iniesta, J. C. (Jan. 2001). „Sunspot Magnetic Fields“. In: *Magnetic Fields Across the Hertzsprung-Russell Diagram*. Ed. by G. Mathys, S. K. Solanki, and D. T. Wickramasinghe. Vol. 248. Astronomical Society of the Pacific Conference Series, p. 35 (cit. on p. 15).
- del Toro Iniesta, José Carlos (2003). *Introduction to Spectropolarimetry* (cit. on p. 6).
- Del Zanna, Giulio, Jenna Samra, Austin Monaghan, et al. (Mar. 2023). „Coronal Densities, Temperatures, and Abundances during the 2019 Total Solar Eclipse: The Role of Multi-wavelength Observations in Coronal Plasma Characterization“. In: *Astrophysical Journals* 265.1, 11, p. 11. DOI: [10.3847/1538-4365/acad68](https://doi.org/10.3847/1538-4365/acad68). arXiv: [2212.11889 \[astro-ph.SR\]](https://arxiv.org/abs/2212.11889) (cit. on p. 13).
- Deng, Na, Debi Prasad Choudhary, Alexandra Tritschler, et al. (Dec. 2007). „Flow Field Evolution of a Decaying Sunspot“. In: *Astrophysical Journal* 671.1, pp. 1013–1021. DOI: [10.1086/523102](https://doi.org/10.1086/523102). arXiv: [0709.3340 \[astro-ph\]](https://arxiv.org/abs/0709.3340) (cit. on p. 17).
- Denker, Carsten, Christoph Kuckein, Meetu Verma, et al. (May 2018). „High-cadence Imaging and Imaging Spectroscopy at the GREGOR Solar Telescope—A Collaborative Research Environment for High-resolution Solar Physics“. In: *The Astrophysical Journal Supplement* 236.1, 5, p. 5. DOI: [10.3847/1538-4365/aab773](https://doi.org/10.3847/1538-4365/aab773). arXiv: [1802.10146 \[astro-ph.IM\]](https://arxiv.org/abs/1802.10146) (cit. on p. 20).
- Denker, Carsten, Meetu Verma, Aneta Wiśniewska, et al. (Jan. 2023). „Improved High-resolution Fast Imager“. In: *Journal of Astronomical Telescopes, Instruments, and Systems* 9, 015001, p. 015001. DOI: [10.1117/1.JATIS.9.1.015001](https://doi.org/10.1117/1.JATIS.9.1.015001) (cit. on p. 27).
- Díaz Baso, C. J. and A. Asensio Ramos (June 2018). „Enhancing SDO/HMI images using deep learning“. In: *A&A* 614, A5, A5. DOI: [10.1051/0004-6361/201731344](https://doi.org/10.1051/0004-6361/201731344). arXiv: [1706.02933 \[astro-ph.SR\]](https://arxiv.org/abs/1706.02933) (cit. on p. 24).
- Domingo, V., B. Fleck, and A. I. Poland (Apr. 1995). „SOHO: The Solar and Heliospheric Observatory“. In: *Space Science Reviews* 72.1-2, pp. 81–84. DOI: [10.1007/BF00768758](https://doi.org/10.1007/BF00768758) (cit. on p. 14).
- Doschek, G. A. (Feb. 1997). „Emission Measures and Electron Densities for the Solar Transition Region“. In: *Astrophysical Journal* 476.2, pp. 903–917. DOI: [10.1086/303640](https://doi.org/10.1086/303640) (cit. on p. 12).

- Edlén, B. (Jan. 1945). „The identification of the coronal lines (George Darwin Lecture)“. In: *Monthly Notices of the Royal Astronomical Society* 105, p. 323. DOI: [10.1093/mnras/105.6.323](https://doi.org/10.1093/mnras/105.6.323) (cit. on p. 13).
- Foukal, Peter (2013). *Solar astrophysics, 3rd, Revised Edition* (cit. on p. 14).
- Fox, N. J., M. C. Velli, S. D. Bale, et al. (Dec. 2016). „The Solar Probe Plus Mission: Humanity’s First Visit to Our Star“. In: *Space Science Reviews* 204.1-4, pp. 7–48. DOI: [10.1007/s11214-015-0211-6](https://doi.org/10.1007/s11214-015-0211-6) (cit. on p. 20).
- García-Rivas, M., J. Jurčák, and N. Bello González (May 2021). „Magnetic properties on the boundary of an evolving pore“. In: *A&A* 649, A129, A129. DOI: [10.1051/0004-6361/202039661](https://doi.org/10.1051/0004-6361/202039661). arXiv: [2102.08459 \[astro-ph.SR\]](https://arxiv.org/abs/2102.08459) (cit. on pp. v, vii, 3).
- Golub, L., E. DeLuca, G. Austin, et al. (June 2007). „The X-Ray Telescope (XRT) for the Hinode Mission“. In: *Solar Physics* 243.1, pp. 63–86. DOI: [10.1007/s11207-007-0182-1](https://doi.org/10.1007/s11207-007-0182-1) (cit. on p. 25).
- Goode, P. R., R. Coulter, N. Gorceix, V. Yurchyshyn, and W. Cao (June 2010). „The NST: First results and some lessons for ATST and EST“. In: *Astronomische Nachrichten* 331.6, p. 620. DOI: [10.1002/asna.201011387](https://doi.org/10.1002/asna.201011387) (cit. on p. 20).
- Gough, D. O. and M. J. Thompson (Jan. 1990). „The effect of rotation and a buried magnetic field on stellar oscillations“. In: *Monthly Notices of the Royal Astronomical Society* 242, pp. 25–55. DOI: [10.1093/mnras/242.1.25](https://doi.org/10.1093/mnras/242.1.25) (cit. on p. 6).
- Green, Lucie M., Tibor Török, Bojan Vršnak, Ward Manchester, and Astrid Veronig (Feb. 2018). „The Origin, Early Evolution and Predictability of Solar Eruptions“. In: *Space Science Reviews* 214.1, 46, p. 46. DOI: [10.1007/s11214-017-0462-5](https://doi.org/10.1007/s11214-017-0462-5). arXiv: [1801.04608 \[astro-ph.SR\]](https://arxiv.org/abs/1801.04608) (cit. on p. 1).
- Grotian, W. (Mar. 1939). „Zur Frage der Deutung der Linien im Spektrum der Sonnenkorona“. In: *Naturwissenschaften* 27.13, pp. 214–214. DOI: [10.1007/BF01488890](https://doi.org/10.1007/BF01488890) (cit. on p. 13).
- Hale, George E. (Dec. 1908). „The Zeeman Effect in the Sun“. In: *Publications of the Astronomical Society of the Pacific* 20.123, p. 287. DOI: [10.1086/121847](https://doi.org/10.1086/121847) (cit. on p. 6).
- Handy, B. N., L. W. Acton, C. C. Kankelborg, et al. (July 1999). „The transition region and coronal explorer“. In: *Solar Physics* 187.2, pp. 229–260. DOI: [10.1023/A:1005166902804](https://doi.org/10.1023/A:1005166902804) (cit. on p. 14).
- Hansen, C. J., S. D. Kawaler, and V. Trimble (2004). „Stellar Interiors“. In: 2nd ed. New York: Springer-Verlag. Chap. 5, p. 241 (cit. on p. 6).
- Hardy, John W. (1998). *Adaptive Optics for Astronomical Telescopes* (cit. on p. 20).
- Harra, Louise (Feb. 2000). „Solar activity studies through coronal X-ray observations“. In: *Astronomy, physics and chemistry of H⁺₃*. Vol. 358, pp. 641–655. DOI: [10.1098/rsta.2000.0550](https://doi.org/10.1098/rsta.2000.0550) (cit. on p. 14).
- Hathaway, D. H., J. G. Beck, R. S. Bogart, et al. (Apr. 2000). „The Photospheric Convection Spectrum“. In: *Solar Physics* 193, pp. 299–312. DOI: [10.1023/A:1005200809766](https://doi.org/10.1023/A:1005200809766) (cit. on p. 9).
- Holweger, H. (Jan. 1967). „Ein empirisches Modell der Sonnenatmosphäre mit lokalem thermodynamischem Gleichgewicht“. In: *Zeitschrift für Astrophysik* 65, p. 365 (cit. on p. 10).

- Jurčák, J., L. R. Bellot Rubio, and M. Sobotka (Apr. 2014). „Orphan penumbrae: Submerging horizontal fields“. In: *A&A* 564, A91, A91. doi: [10.1051/0004-6361/201322340](https://doi.org/10.1051/0004-6361/201322340). arXiv: [1402.6558 \[astro-ph.SR\]](https://arxiv.org/abs/1402.6558) (cit. on p. 15).
- Jurčák, J., R. Rezaei, N. Bello González, R. Schlichenmaier, and J. Vomlel (Mar. 2018). „The magnetic nature of umbra-penumbra boundary in sunspots“. In: *A&A* 611, L4, p. L4. doi: [10.1051/0004-6361/201732528](https://doi.org/10.1051/0004-6361/201732528). arXiv: [1801.08983 \[astro-ph.SR\]](https://arxiv.org/abs/1801.08983) (cit. on pp. 14, 17).
- Keys, Peter H., Aaron Reid, Mihalis Mathioudakis, et al. (Sept. 2019). „The magnetic properties of photospheric magnetic bright points with high-resolution spectropolarimetry“. In: *Monthly Notices of the Royal Astronomical Society* 488.1, pp. L53–L58. doi: [10.1093/mnrasl/slz097](https://doi.org/10.1093/mnrasl/slz097). arXiv: [1906.07687 \[astro-ph.SR\]](https://arxiv.org/abs/1906.07687) (cit. on pp. 17, 80).
- Kleint, Lucia, Thomas Berkefeld, Miguel Esteves, et al. (Sept. 2020). „GREGOR: Optics redesign and updates from 2018-2020“. In: *Astronomy and Astrophysics* 641, A27, A27. doi: [10.1051/0004-6361/202038208](https://doi.org/10.1051/0004-6361/202038208). arXiv: [2006.11875 \[astro-ph.IM\]](https://arxiv.org/abs/2006.11875) (cit. on p. 27).
- Kolmogorov, A. N. (July 1991). „The Local Structure of Turbulence in Incompressible Viscous Fluid for Very Large Reynolds Numbers“. In: *Proceedings of the Royal Society of London Series A* 434.1890, pp. 9–13. doi: [10.1098/rspa.1991.0075](https://doi.org/10.1098/rspa.1991.0075) (cit. on p. 21).
- Kosugi, T., K. Matsuzaki, T. Sakao, et al. (June 2007). „The Hinode (Solar-B) Mission: An Overview“. In: *Solar Physics* 243.1, pp. 3–17. doi: [10.1007/s11207-007-9014-6](https://doi.org/10.1007/s11207-007-9014-6) (cit. on pp. 1, 14).
- Kuckein, C., C. Denker, M. Verma, et al. (Oct. 2017). „sTools - a data reduction pipeline for the GREGOR Fabry-Pérot Interferometer and the High-resolution Fast Imager at the GREGOR solar telescope“. In: *Fine Structure and Dynamics of the Solar Atmosphere*. Ed. by S. Vargas Domínguez, A. G. Kosovichev, P. Antolin, and L. Harra. Vol. 327, pp. 20–24. doi: [10.1017/S1743921317000114](https://doi.org/10.1017/S1743921317000114). arXiv: [1701.01670 \[astro-ph.IM\]](https://arxiv.org/abs/1701.01670) (cit. on p. 22).
- Labeyrie, A. (May 1970). „Attainment of Diffraction Limited Resolution in Large Telescopes by Fourier Analysing Speckle Patterns in Star Images“. In: *A&A* 6, p. 85 (cit. on p. 22).
- Leighton, Robert B., Robert W. Noyes, and George W. Simon (Mar. 1962). „Velocity Fields in the Solar Atmosphere. I. Preliminary Report.“ In: *Astrophysical Journal* 135, p. 474. doi: [10.1086/147285](https://doi.org/10.1086/147285) (cit. on p. 23).
- Lemen, James R., Alan M. Title, David J. Akin, et al. (Jan. 2012). „The Atmospheric Imaging Assembly (AIA) on the Solar Dynamics Observatory (SDO)“. In: *Solar Physics* 275.1-2, pp. 17–40. doi: [10.1007/s11207-011-9776-8](https://doi.org/10.1007/s11207-011-9776-8) (cit. on p. 8).
- Lisle, J. and J. Toomre (Oct. 2004). „Cause of Shrinking Sun Effect in Local Correlation Tracking and Impacts on the Mapping of Ssw Flows“. In: *SOHO 14 Helio- and Asteroseismology: Towards a Golden Future*. Ed. by D. Danesy. Vol. 559. ESA Special Publication, p. 556 (cit. on p. 23).
- Liu, Yanxiao, Yongyuan Xiang, Robertus Erdélyi, et al. (Mar. 2018). „Studies of Isolated and Non-isolated Photospheric Bright Points in an Active Region Observed by the New Vacuum Solar Telescope“. In: *Astrophysical Journal* 856.1, 17, p. 17. doi: [10.3847/1538-4357/aab150](https://doi.org/10.3847/1538-4357/aab150) (cit. on p. 17).
- Löfdahl, M. G., M. J. van Noort, and C. Denker (Jan. 2007). „Solar image restoration“. In: *Modern solar facilities - advanced solar science*. Ed. by Franz Kneer, Klaus G. Puschmann, and Axel D. Wittmann, p. 119 (cit. on p. 23).

- Löfdahl, Mats G. and Goran B. Scharmer (Sept. 1994). „Application of phase-diversity to solar images“. In: *Image Reconstruction and Restoration*. Ed. by Timothy J. Schulz and Donald L. Snyder. Vol. 2302. Society of Photo-Optical Instrumentation Engineers (SPIE) Conference Series, pp. 254–267. DOI: [10.1117/12.188043](https://doi.org/10.1117/12.188043) (cit. on p. 22).
- Lyot, B. (Jan. 1931). „L'Etude de la Couronne Solaire en Dehors des Eclipses.“ In: *L'Astronomie* 45, pp. 248–253 (cit. on p. 13).
- Magnetic Fields in the Solar System* (Jan. 2018). Vol. 448. Astrophysics and Space Science Library. DOI: [10.1007/978-3-319-64292-5](https://doi.org/10.1007/978-3-319-64292-5) (cit. on p. 6).
- Mallia, E. A. (Nov. 1968). „A Study of Weak Molecular and Atomic Lines in the Photospheric Spectrum“. In: *Solar Physics* 5.3, pp. 281–302. DOI: [10.1007/BF00147141](https://doi.org/10.1007/BF00147141) (cit. on p. 18).
- Mao, Jiandong, Yingnan Zhang, Juan Li, et al. (2023). „Novel Detection of Atmospheric Turbulence Profile Using Mie-Scattering Lidar Based on Non-Kolmogorov Turbulence Theory“. In: *Entropy* 25.3. DOI: [10.3390/e25030477](https://doi.org/10.3390/e25030477) (cit. on p. 21).
- Martínez Pillet, V. (July 2002). „Decay of sunspots“. In: *Astronomische Nachrichten* 323, pp. 342–348. DOI: [10.1002/1521-3994\(200208\)323:3/4<342::AID-ASNA342>3.0.CO;2-5](https://doi.org/10.1002/1521-3994(200208)323:3/4<342::AID-ASNA342>3.0.CO;2-5) (cit. on p. 17).
- Masson, Colin R. (Jan. 1994). „Seeing [invited]“. In: *Very High Angular Resolution Imaging*. Ed. by J. G. Robertson and William J. Tango. Vol. 158, p. 1 (cit. on p. 20).
- Meyer, F., H. U. Schmidt, and N. O. Weiss (June 1977). „The stability of sunspots.“ In: *Monthly Notices of the Royal Astronomical Society* 179, pp. 741–761. DOI: [10.1093/mnras/179.4.741](https://doi.org/10.1093/mnras/179.4.741) (cit. on p. 16).
- Moses, Dan, J. W. Cook, J. -D. F. Bartoe, et al. (Aug. 1994). „Solar Fine-Scale Structures in the Corona, Transition Region, and Lower Atmosphere“. In: *Astrophysical Journal* 430, p. 913. DOI: [10.1086/174461](https://doi.org/10.1086/174461) (cit. on p. 12).
- Mullan, Dermott J. (2010). *Physics of the Sun. A first course*. Boca Ratón, London, New York: CRC Press. Taylor & Francis Group (cit. on pp. 5, 11).
- Muller, R., Th. Roudier, and J. C. Hulot (Sept. 1989). „Perturbation of the Granular Pattern by the Presence of Magnetic Flux Tubes“. In: *Solar Physics* 119.2, pp. 229–243. DOI: [10.1007/BF00146177](https://doi.org/10.1007/BF00146177) (cit. on p. 18).
- Müller, D., O. C. St. Cyr, I. Zouganelis, et al. (Oct. 2020). „The Solar Orbiter mission. Science overview“. In: *Astronomy and Astrophysics* 642, A1, A1. DOI: [10.1051/0004-6361/202038467](https://doi.org/10.1051/0004-6361/202038467). arXiv: [2009.00861 \[astro-ph.SR\]](https://arxiv.org/abs/2009.00861) (cit. on p. 20).
- November, Laurence J. and George W. Simon (Oct. 1988). „Precise Proper-Motion Measurement of Solar Granulation“. In: *Astrophysical Journal* 333, p. 427. DOI: [10.1086/166758](https://doi.org/10.1086/166758) (cit. on pp. 1, 23).
- Noyes, Robert W. and Robert B. Leighton (Oct. 1963). „Velocity Fields in the Solar Atmosphere. II. The Oscillatory Field.“ In: *Astrophysical Journal* 138, p. 631. DOI: [10.1086/147675](https://doi.org/10.1086/147675) (cit. on p. 23).
- Parker, E. N. (May 1970). „The Origin of Magnetic Fields“. In: *Astrophysical Journal* 160, p. 383. DOI: [10.1086/150442](https://doi.org/10.1086/150442) (cit. on p. 5).
- (June 1979). „Sunspots and the physics of magnetic flux tubes. I. The general nature of the sunspots.“ In: *Astrophysical Journal* 230, pp. 905–923. DOI: [10.1086/157150](https://doi.org/10.1086/157150) (cit. on p. 6).

- Parker, Eugene N. (Sept. 1955). „Hydromagnetic Dynamo Models.“ In: *Astrophysical Journal* 122, p. 293. DOI: [10.1086/146087](https://doi.org/10.1086/146087) (cit. on p. 6).
- Pesnell, W. Dean, B. J. Thompson, and P. C. Chamberlin (Jan. 2012). „The Solar Dynamics Observatory (SDO)“. In: *Solar Physics* 275.1-2, pp. 3–15. DOI: [10.1007/s11207-011-9841-3](https://doi.org/10.1007/s11207-011-9841-3) (cit. on pp. 1, 14).
- Potts, H. E., R. K. Barrett, and D. A. Diver (Sept. 2004). „Balltracking: An highly efficient method for tracking flow fields“. In: *A&A* 424, pp. 253–262. DOI: [10.1051/0004-6361:20035891](https://doi.org/10.1051/0004-6361:20035891) (cit. on p. 24).
- Priest, E. R. and T. G. Forbes (Jan. 2002). „The magnetic nature of solar flares“. In: *A&A Reviews* 10.4, pp. 313–377. DOI: [10.1007/s001590100013](https://doi.org/10.1007/s001590100013) (cit. on p. 14).
- Reiners, A. and G. Basri (Mar. 2009). „On the magnetic topology of partially and fully convective stars“. In: *A&A* 496.3, pp. 787–790. DOI: [10.1051/0004-6361:200811450](https://doi.org/10.1051/0004-6361:200811450). arXiv: [0901.1659 \[astro-ph.SR\]](https://arxiv.org/abs/0901.1659) (cit. on p. 6).
- Ren, Deqing, Laurent Jolissaint, Xi Zhang, et al. (May 2015). „Solar Ground-Layer Adaptive Optics“. In: *Publications of the Astronomical Society of the Pacific* 127.951, p. 469. DOI: [10.1086/681672](https://doi.org/10.1086/681672) (cit. on p. 22).
- Riethmüller, T. L., S. K. Solanki, V. Zakharov, and A. Gandorfer (Dec. 2008). „Brightness, distribution, and evolution of sunspot umbral dots“. In: *A&A* 492.1, pp. 233–243. DOI: [10.1051/0004-6361:200810701](https://doi.org/10.1051/0004-6361:200810701). arXiv: [0812.0477 \[astro-ph\]](https://arxiv.org/abs/0812.0477) (cit. on p. 15).
- Rigaut, Francois J., Brent L. Ellerbroek, and Ralf Flicker (2000). „Principles, limitations, and performance of multiconjugate adaptive optics“. In: *Adaptive Optical Systems Technology*. Ed. by Peter L. Wizinowich. Vol. 4007. International Society for Optics and Photonics. SPIE, pp. 1022–1031. DOI: [10.1117/12.390311](https://doi.org/10.1117/12.390311) (cit. on p. 22).
- Rimmele, T. R., F. Woeger, J. Marino, et al. (July 2010). „Solar multiconjugate adaptive optics at the Dunn Solar Telescope“. In: *Adaptive Optics Systems II*. Ed. by Brent L. Ellerbroek, Michael Hart, Norbert Hubin, and Peter L. Wizinowich. Vol. 7736. Society of Photo-Optical Instrumentation Engineers (SPIE) Conference Series, 773631, p. 773631. DOI: [10.1117/12.857485](https://doi.org/10.1117/12.857485) (cit. on p. 22).
- Rimmele, Thomas R. (Oct. 2004). „Recent advances in solar adaptive optics“. In: *Advances in Adaptive Optics*. Ed. by Domenico Bonaccini Calia, Brent L. Ellerbroek, and Roberto Ragazzoni. Vol. 5490. Society of Photo-Optical Instrumentation Engineers (SPIE) Conference Series, pp. 34–46. DOI: [10.1117/12.551764](https://doi.org/10.1117/12.551764) (cit. on p. 22).
- Rimmele, Thomas R. and Jose Marino (June 2011). „Solar Adaptive Optics“. In: *Living Reviews in Solar Physics* 8.1, 2, p. 2. DOI: [10.12942/lrsp-2011-2](https://doi.org/10.12942/lrsp-2011-2) (cit. on p. 21).
- Rimmele, Thomas R., Mark Warner, Stephen L. Keil, et al. (Dec. 2020). „The Daniel K. Inouye Solar Telescope - Observatory Overview“. In: *Solar Physics* 295.12, 172, p. 172. DOI: [10.1007/s11207-020-01736-7](https://doi.org/10.1007/s11207-020-01736-7) (cit. on p. 20).
- Roudier, Th., M. Rieutord, J. M. Malherbe, and J. Vigneau (Sept. 1999). „Determination of horizontal velocity fields at the sun’s surface with high spatial and temporal resolution“. In: *A&A* 349, pp. 301–311 (cit. on p. 24).
- Rutten, R. J., D. Kiselman, L. Rouppe van der Voort, and B. Plez (Jan. 2001). „Proxy Magnetometry of the Photosphere: Why are G-Band Bright Points so Bright?“ In: *Advanced Solar Polarimetry – Theory, Observation, and Instrumentation*. Ed. by Michael Sigwarth. Vol. 236. Astronomical Society of the Pacific Conference Series, p. 445 (cit. on p. 18).

- Samanta, Tanmoy, Hui Tian, Vasyl Yurchyshyn, et al. (Nov. 2019). „Generation of solar spicules and subsequent atmospheric heating“. In: *Science* 366.6467, pp. 890–894. DOI: [10.1126/science.aaw2796](https://doi.org/10.1126/science.aaw2796). arXiv: [2006.02571 \[astro-ph.SR\]](https://arxiv.org/abs/2006.02571) (cit. on p. 18).
- Sánchez Almeida, J., I. Márquez, J. A. Bonet, I. Domínguez Cerdeña, and R. Muller (July 2004). „Bright Points in the Internetwork Quiet Sun“. In: *Astrophysical Journal* 609.2, pp. L91–L94. DOI: [10.1086/422752](https://doi.org/10.1086/422752). arXiv: [astro-ph/0405515 \[astro-ph\]](https://arxiv.org/abs/astro-ph/0405515) (cit. on p. 17).
- Scharmer, G. B., M. G. Löfdahl, T. I. M. van Werkhoven, and J. de la Cruz Rodríguez (Oct. 2010). „High-order aberration compensation with multi-frame blind deconvolution and phase diversity image restoration techniques“. In: *A&A* 521, A68, A68. DOI: [10.1051/0004-6361/201014800](https://doi.org/10.1051/0004-6361/201014800). arXiv: [1007.1236 \[astro-ph.IM\]](https://arxiv.org/abs/1007.1236) (cit. on p. 22).
- Scharmer, G. B., G. Narayan, T. Hillberg, et al. (Dec. 2008). „CRISP Spectropolarimetric Imaging of Penumbral Fine Structure“. In: *Astrophysical Journal Letters* 689.1, p. L69. DOI: [10.1086/595744](https://doi.org/10.1086/595744). arXiv: [0806.1638 \[astro-ph\]](https://arxiv.org/abs/0806.1638) (cit. on p. 20).
- Scharmer, Goran B., Klas Bjelksjo, Tapio K. Korhonen, Bo Lindberg, and Bertil Petterson (Feb. 2003). „The 1-meter Swedish solar telescope“. In: *Innovative Telescopes and Instrumentation for Solar Astrophysics*. Ed. by Stephen L. Keil and Sergey V. Avakyan. Vol. 4853. Society of Photo-Optical Instrumentation Engineers (SPIE) Conference Series, pp. 341–350. DOI: [10.1117/12.460377](https://doi.org/10.1117/12.460377) (cit. on p. 19).
- Scherrer, P. H., J. Schou, R. I. Bush, et al. (Jan. 2012). „The Helioseismic and Magnetic Imager (HMI) Investigation for the Solar Dynamics Observatory (SDO)“. In: *Solar Physics* 275.1-2, pp. 207–227. DOI: [10.1007/s11207-011-9834-2](https://doi.org/10.1007/s11207-011-9834-2) (cit. on p. 1).
- Schmidt, W., O. von der Lühe, R. Volkmer, et al. (Nov. 2012). „The 1.5 meter solar telescope GREGOR“. In: *Astronomische Nachrichten* 333.9, p. 796. DOI: [10.1002/asna.201211725](https://doi.org/10.1002/asna.201211725) (cit. on pp. 20, 27).
- Schmieder, B. and G. Aulanier (June 2012). „New perspectives on solar prominences“. In: *EAS Publications Series*. Ed. by M. Faurobert, C. Fang, and T. Corbard. Vol. 55. EAS Publications Series, pp. 149–161. DOI: [10.1051/eas/1255021](https://doi.org/10.1051/eas/1255021) (cit. on p. 11).
- Schrijver, Carolus J. (Mar. 2009). „Driving major solar flares and eruptions: A review“. In: *Advances in Space Research* 43.5, pp. 739–755. DOI: [10.1016/j.asr.2008.11.004](https://doi.org/10.1016/j.asr.2008.11.004). arXiv: [0811.0787 \[astro-ph\]](https://arxiv.org/abs/0811.0787) (cit. on p. 15).
- Schrijver, Karel, Fran Bagenal, Tim Bastian, et al. (Oct. 2019). *Principles Of Heliophysics: a textbook on the universal processes behind planetary habitability*, arXiv:1910.14022, arXiv:1910.14022. DOI: [10.48550/arXiv.1910.14022](https://doi.org/10.48550/arXiv.1910.14022). arXiv: [1910.14022 \[astro-ph.SR\]](https://arxiv.org/abs/1910.14022) (cit. on p. 5).
- Schuck, P. W. (Aug. 2006). „Tracking Magnetic Footpoints with the Magnetic Induction Equation“. In: *Astrophysical Journal* 646, pp. 1358–1391 (cit. on pp. 1, 24).
- Schulz, T. J. (May 1993). „Multiframe blind deconvolution of astronomical images.“ In: *Journal of the Optical Society of America A* 10.5, pp. 1064–1073. DOI: [10.1364/JOSAA.10.001064](https://doi.org/10.1364/JOSAA.10.001064) (cit. on p. 22).
- Schüssler, M., S. Shelyag, S. Berdyugina, A. Vögler, and S. K. Solanki (Nov. 2003). „Why Solar Magnetic Flux Concentrations Are Bright in Molecular Bands“. In: *Astrophysical Journal Letters* 597.2, pp. L173–L176. DOI: [10.1086/379869](https://doi.org/10.1086/379869) (cit. on p. 18).

- Sheeley N. R., Jr., J. R. Stauffer, J. C. Thomassie, and H. P. Warren (Feb. 2017). „Tracking the Magnetic Flux in and around Sunspots“. In: *Astrophysical Journal* 836.1, 144, p. 144. DOI: [10.3847/1538-4357/836/1/144](https://doi.org/10.3847/1538-4357/836/1/144) (cit. on p. 17).
- Shibata, Kazunari and Tetsuya Magara (Dec. 2011). „Solar Flares: Magnetohydrodynamic Processes“. In: *Living Reviews in Solar Physics* 8.1, 6, p. 6. DOI: [10.12942/lrsp-2011-6](https://doi.org/10.12942/lrsp-2011-6) (cit. on pp. 11, 14).
- Simon, G. W. and R. B. Leighton (Oct. 1964). „Velocity Fields in the Solar Atmosphere. III. Large-Scale Motions, the Chromospheric Network, and Magnetic Fields.“ In: *Astrophysical Journal* 140, p. 1120. DOI: [10.1086/148010](https://doi.org/10.1086/148010) (cit. on p. 23).
- Simon, W. G. (Jan. 1967). „Observations of Horizontal Motions in Solar Granulation: Their Relation to Supergranulation“. In: *Zeitschrift für Astrophysik* 65, p. 345 (cit. on p. 23).
- Sliney, D. H. (Feb. 2016). „What is light? The visible spectrum and beyond“. In: *Eye* 30, pp. 222–229. DOI: [10.1038/eye.2015.252](https://doi.org/10.1038/eye.2015.252) (cit. on p. 19).
- Sobotka, M. and K. G. Puschmann (Sept. 2009). „Morphology and evolution of umbral dots and their substructures“. In: *A&A* 504.2, pp. 575–581. DOI: [10.1051/0004-6361/200912365](https://doi.org/10.1051/0004-6361/200912365). arXiv: [0907.4236 \[astro-ph.SR\]](https://arxiv.org/abs/0907.4236) (cit. on p. 15).
- Solanki, Sami K. (Jan. 2003). „Sunspots: An overview“. In: *A&A Reviews* 11.2-3, pp. 153–286. DOI: [10.1007/s00159-003-0018-4](https://doi.org/10.1007/s00159-003-0018-4) (cit. on pp. 14, 15).
- Spiegel, E. A. and J. -P. Zahn (Nov. 1992). „The solar tachocline.“ In: *A&A* 265, pp. 106–114 (cit. on p. 6).
- Steiner, O. (2000). „Chromosphere: Magnetic Canopy“. In: *Encyclopedia of Astronomy and Astrophysics*. Ed. by P. Murdin, 2264, p. 2264. DOI: [10.1888/0333750888/2264](https://doi.org/10.1888/0333750888/2264) (cit. on p. 11).
- Steiner, O., J. Bruls, and P. H. Hauschildt (Jan. 2001). „Why are G-Band Bright Points Bright?“ In: *Advanced Solar Polarimetry – Theory, Observation, and Instrumentation*. Ed. by Michael Sigwarth. Vol. 236. Astronomical Society of the Pacific Conference Series, p. 453 (cit. on p. 18).
- Stenflo, J. O. (Sept. 2013). „Solar magnetic fields as revealed by Stokes polarimetry“. In: *A&A Reviews* 21, 66, p. 66. DOI: [10.1007/s00159-013-0066-3](https://doi.org/10.1007/s00159-013-0066-3). arXiv: [1309.5454 \[astro-ph.SR\]](https://arxiv.org/abs/1309.5454) (cit. on p. 6).
- Stix, Michael (2002). *The sun: an introduction* (cit. on p. 17).
- Strecker, H., W. Schmidt, R. Schlichenmaier, and M. Rempel (May 2021). „On the (in)stability of sunspots“. In: *A&A* 649, A123, A123. DOI: [10.1051/0004-6361/202040199](https://doi.org/10.1051/0004-6361/202040199). arXiv: [2103.11487 \[astro-ph.SR\]](https://arxiv.org/abs/2103.11487) (cit. on p. 16).
- Thomas, J. H. (Jan. 2010). „Theoretical Models of Sunspot Structure and Dynamics“. In: *Magnetic Coupling between the Interior and Atmosphere of the Sun*. Vol. 19. Astrophysics and Space Science Proceedings, pp. 229–242. DOI: [10.1007/978-3-642-02859-5_17](https://doi.org/10.1007/978-3-642-02859-5_17). arXiv: [0903.4106 \[astro-ph.SR\]](https://arxiv.org/abs/0903.4106) (cit. on pp. 14, 17).
- Thompson, M. J., A. Balogh, J. L. Culhane, et al. (2009). *The Origin and Dynamics of Solar Magnetism*. Vol. 32. DOI: [10.1007/978-1-4419-0239-9](https://doi.org/10.1007/978-1-4419-0239-9) (cit. on p. 2).
- Title, A. M. and T. D. Tarbell (Sept. 1986). „Properties of Granulation from Filtered Movies of Spacelab 2 SOUP Images“. In: *Bulletin of the American Astronomical Society*. Vol. 18, p. 992 (cit. on p. 23).

- Title, A. M., T. D. Tarbell, G. W. Simon, et al. (Jan. 1986). „White-light movies of the solar photosphere from the soup instrument on spacelab 2“. In: *Advances in Space Research* 6.8, pp. 253–262. doi: [10.1016/0273-1177\(86\)90447-3](https://doi.org/10.1016/0273-1177(86)90447-3) (cit. on p. 9).
- Toriumi, Shin and Haimin Wang (May 2019). „Flare-productive active regions“. In: *Living Reviews in Solar Physics* 16.1, 3, p. 3. doi: [10.1007/s41116-019-0019-7](https://doi.org/10.1007/s41116-019-0019-7). arXiv: [1904.12027 \[astro-ph.SR\]](https://arxiv.org/abs/1904.12027) (cit. on p. 1).
- Trujillo Bueno, J., A. Asensio Ramos, and N. Shchukina (Dec. 2006). „The Hanle Effect in Atomic and Molecular Lines: A New Look at the Sun’s Hidden Magnetism“. In: *Solar Polarization* 4. Ed. by R. Casini and B. W. Lites. Vol. 358. Astronomical Society of the Pacific Conference Series, p. 269. doi: [10.48550/arXiv.astro-ph/0612678](https://doi.org/10.48550/arXiv.astro-ph/0612678). arXiv: [astro-ph/0612678 \[astro-ph\]](https://arxiv.org/abs/astro-ph/0612678) (cit. on p. 6).
- Tsuneta, S., K. Ichimoto, Y. Katsukawa, et al. (June 2008a). „The Solar Optical Telescope for the Hinode Mission: An Overview“. In: *Solar Physics* 249.2, pp. 167–196. doi: [10.1007/s11207-008-9174-z](https://doi.org/10.1007/s11207-008-9174-z). arXiv: [0711.1715 \[astro-ph\]](https://arxiv.org/abs/0711.1715) (cit. on p. 1).
- (June 2008b). „The Solar Optical Telescope for the Hinode Mission: An Overview“. In: *Solar Physics* 249.2, pp. 167–196. doi: [10.1007/s11207-008-9174-z](https://doi.org/10.1007/s11207-008-9174-z). arXiv: [0711.1715 \[astro-ph\]](https://arxiv.org/abs/0711.1715) (cit. on p. 25).
- Astronomical Adaptive Optics Systems and Applications IV* (Sept. 2011). Vol. 8149. Society of Photo-Optical Instrumentation Engineers (SPIE) Conference Series (cit. on p. 20).
- Utz, D., A. Hanslmeier, C. Möstl, et al. (Apr. 2009). „The size distribution of magnetic bright points derived from Hinode/SOT observations“. In: *A&A* 498.1, pp. 289–293. doi: [10.1051/0004-6361/200810867](https://doi.org/10.1051/0004-6361/200810867). arXiv: [0912.2637 \[astro-ph.SR\]](https://arxiv.org/abs/0912.2637) (cit. on p. 17).
- Utz, D., J. Jurčák, A. Hanslmeier, et al. (June 2013). „Magnetic field strength distribution of magnetic bright points inferred from filtergrams and spectro-polarimetric data“. In: *A&A* 554, A65, A65. doi: [10.1051/0004-6361/201116894](https://doi.org/10.1051/0004-6361/201116894). arXiv: [1304.5508 \[astro-ph.SR\]](https://arxiv.org/abs/1304.5508) (cit. on p. 17).
- Valenzuela, John R., Jeffrey A. Fessler, and Richard G. Paxman (Apr. 2010). „Joint estimation of Stokes images and aberrations from phase-diverse polarimetric measurements“. In: *Journal of the Optical Society of America A* 27.5, p. 1185. doi: [10.1364/JOSAA.27.001185](https://doi.org/10.1364/JOSAA.27.001185) (cit. on p. 22).
- van de Hulst, H. C. (Feb. 1950). „On the polar rays of the corona (Errata: 11 VIII)“. In: *Bulletin of the Astronomical Institutes of the Netherlands* 11, p. 150 (cit. on p. 12).
- van Kampen, William C. and Richard G. Paxman (Nov. 1998). „Multiframe blind deconvolution of infinite-extent objects“. In: *Propagation and Imaging through the Atmosphere II*. Ed. by Luc R. Bissonnette. Vol. 3433. Society of Photo-Optical Instrumentation Engineers (SPIE) Conference Series, pp. 296–307. doi: [10.1117/12.330227](https://doi.org/10.1117/12.330227) (cit. on p. 22).
- Van Noort, Michiel, Luc Rouppe Van Der Voort, and Mats G. Löfdahl (May 2005). „Solar Image Restoration By Use Of Multi-frame Blind De-convolution With Multiple Objects And Phase Diversity“. In: *Solar Physics* 228.1-2, pp. 191–215. doi: [10.1007/s11207-005-5782-z](https://doi.org/10.1007/s11207-005-5782-z) (cit. on p. 22).
- von der Luehe, O. (Feb. 1993). „Speckle imaging of solar small scale structure. I - Methods“. In: *Astronomy and Astrophysics* 268.1, pp. 374–390 (cit. on p. 22).

- von der Lühe, O. (May 1984). „Estimating Fried’s parameter from a time series of an arbitrary resolved object imaged through atmospheric turbulence.“ In: *Journal of the Optical Society of America A* 1, pp. 510–519. DOI: [10.1364/JOSAA.1.000510](https://doi.org/10.1364/JOSAA.1.000510) (cit. on p. 22).
- von der Lühe, Oskar (July 2003). „Sensitivity of Active and Passive High Resolution Techniques“. In: *Astronomische Nachrichten Supplement* 324.3, p. 23 (cit. on p. 22).
- Webb, D. F., T. A. Howard, C. D. Fry, et al. (May 2009). „Studying geoeffective interplanetary coronal mass ejections between the Sun and Earth: Space weather implications of Solar Mass Ejection Imager observations“. In: *Space Weather* 7.5, S05002, S05002. DOI: [10.1029/2008SW000409](https://doi.org/10.1029/2008SW000409) (cit. on p. 13).
- Welsch, B. T., G. H. Fisher, W. P. Abbett, and S. Regnier (Aug. 2004). „ILCT: Recovering Photospheric Velocities from Magnetograms by Combining the Induction Equation with Local Correlation Tracking“. In: *Astrophysical Journal* 610, pp. 1148–1156 (cit. on pp. 1, 23).
- Wöger, F., O. von der Lühe, and K. Reardon (Sept. 2008). „Speckle interferometry with adaptive optics corrected solar data“. In: *Astronomy and Astrophysics* 488.1, pp. 375–381. DOI: [10.1051/0004-6361:200809894](https://doi.org/10.1051/0004-6361:200809894) (cit. on p. 22).
- Wood, R. W. and Alexander Ellett (June 1923). „On the Influence of Magnetic Fields on the Polarisation of Resonance Radiation“. In: *Proceedings of the Royal Society of London Series A* 103.722, pp. 396–403. DOI: [10.1098/rspa.1923.0065](https://doi.org/10.1098/rspa.1923.0065) (cit. on p. 6).
- Woods, T. N., F. G. Eparvier, R. Hock, et al. (Jan. 2012). „Extreme Ultraviolet Variability Experiment (EVE) on the Solar Dynamics Observatory (SDO): Overview of Science Objectives, Instrument Design, Data Products, and Model Developments“. In: *Solar Physics* 275.1-2, pp. 115–143. DOI: [10.1007/s11207-009-9487-6](https://doi.org/10.1007/s11207-009-9487-6) (cit. on p. 24).
- Zeeman, P. (Feb. 1897). „The Effect of Magnetisation on the Nature of Light Emitted by a Substance“. In: *Nature* 55.1424, p. 347. DOI: [10.1038/055347a0](https://doi.org/10.1038/055347a0) (cit. on p. 6).
- Zirin, Harold (1988). *Astrophysics of the Sun*. 32 East 57th Street, New York, NY, 10022, USA: Cambridge University Press (cit. on p. 10).

Photospheric plasma and magnetic field dynamics during the formation of solar AR 11190

Jose Iván Campos Rozo^{1,2}, Dominik Utz^{1,3}, Santiago Vargas Domínguez², Astrid M. Veronig¹, and Tom Van Doorsselaere⁴

¹ IGAM, Institute of Physics, University of Graz, Universitätsplatz 5, 8010 Graz,
Austria

² Universidad Nacional de Colombia, Observatorio Astronómico Nacional, Ed. 413
Bogotá, Colombia

³ Instituto de Astrofísica de Andalucía IAA-CSIC, 18008 Granada, Spain

⁴ Centre for Mathematical Plasma Astrophysics, Department of Mathematics, KU
Leuven, 3001 Leuven, Belgium

The following article is published in ASTRONOMY & ASTROPHYSICS, Volume 622, article number A168, 14 pp. (2019). It is reproduced with the permission of EDP Sciences. The pdf document can be downloaded from the journal web-page and it is embedded one-to-one in this thesis. My own contribution to this work was at least 60%.

Photospheric plasma and magnetic field dynamics during the formation of solar AR 11190[★]

J. I. Campos Rozo^{1,2}, D. Utz^{1,3}, S. Vargas Domínguez², A. Veronig¹, and T. Van Doorsselaere⁴

¹ IGAM, Institute of Physics, University of Graz, Universitätsplatz 5, 8010 Graz, Austria
e-mail: jose.campos-rozo@uni-graz.at

² Universidad Nacional de Colombia, Observatorio Astronómico Nacional, Ed. 413 Bogotá, Colombia
e-mail: svargasd@unal.edu.co

³ Instituto de Astrofísica de Andalucía IAA-CSIC, 18008 Granada, Spain
e-mail: dominik.utz@uni-graz.at

⁴ Centre for Mathematical Plasma Astrophysics, Department of Mathematics, KU Leuven, 3001 Leuven, Belgium

Received 2 February 2018 / Accepted 15 December 2018

ABSTRACT

Context. The Sun features on its surface typical flow patterns called the granulation, mesogranulation, and supergranulation. These patterns arise due to convective flows transporting energy from the interior of the Sun to its surface. The other well known elements structuring the solar photosphere are magnetic fields arranged from single, isolated, small-scale flux tubes to large and extended regions visible as sunspots and active regions.

Aims. In this paper we will shed light on the interaction between the convective flows in large-scale cells as well as the large-scale magnetic fields in active regions, and investigate in detail the statistical distribution of flow velocities during the evolution and formation of National Oceanic and Atmospheric Administration active region 11190.

Methods. To do so, we employed local correlation tracking methods on data obtained by the Solar Dynamics Observatory in the continuum as well as on processed line-of-sight magnetograms.

Results. We find that the flow fields in an active region can be modelled by a two-component distribution. One component is very stable, follows a Rayleigh distribution, and can be assigned to the background flows, whilst the other component is variable in strength and velocity range and can be attributed to the flux emergence visible both in the continuum maps as well as magnetograms. Generally, the plasma flows, as seen by the distribution of the magnitude of the velocity, follow a Rayleigh distribution even through the time of formation of active regions. However, at certain moments of large-scale fast flux emergence, a second component featuring higher velocities is formed in the velocity magnitudes distribution.

Conclusions. The plasma flows are generally highly correlated to the motion of magnetic elements and vice versa except during the times of fast magnetic flux emergence as observed by rising magnetic elements. At these times, the magnetic fields are found to move faster than the corresponding plasma.

Key words. Sun: photosphere – Sun: granulation – Sun: evolution – Sun: magnetic fields – sunspots

1. Introduction

High-resolution observations have shown that the solar photosphere is a non-uniform layer formed by different structures that are constantly evolving at multiple spatial and temporal scales. Some of these features form patterns, so-called convective cells, granules, “or in more colloquial terms, bubbles” (Hansen et al. 2004). In the centre, these convective cells feature the emergence of hot plasma with vertical velocities of about 0.4 km s^{-1} , while towards their boundaries, the plasma motions become horizontal, moving to the intergranular lanes with velocities of 0.25 km s^{-1} (Title et al. 1986). Diverse studies have shown how granular cells can organize themselves in three main size scales: granulation ($\sim 1000 \text{ km}$; Bushby & Favier 2014), mesogranulation ($5\text{--}10 \text{ Mm}$; November et al. 1981), and supergranulation ($>20 \text{ Mm}$; Rieutord & Rincon 2010).

The evolution of the photospheric granulation pattern is determined by the expansion and the subsequent dissolution of granular cells (Rezaei et al. 2012; Palacios et al. 2012). When

granules start to show the appearance of bright rings, a dark centre, and fast outflows, they are called exploding granules (Title et al. 1986, 1989). This happens during the final expansion at the last stage of their life. Such explosive granules are considered important in the context of the whole solar granulation evolution (Rösch 1961; Musman 1972; Namba & van Rijnsbergen 1977). Understanding the behaviour of the different granulation scales and granular evolution is important in order to obtain more realistic quiet Sun models for the formation, as well as the evolution and decay of active regions (Roudier et al. 2003). The physical processes of the emergence of granular-scale magnetic fields are likely to be the same in the quiet Sun and active regions (Vargas Domínguez et al. 2012).

Large-scale granules (mesogranules and supergranules) have been associated to fast vertical upflows (Roudier et al. 2003; Guglielmino et al. 2010; Palacios et al. 2012; Verma et al. 2016). Moreover, exploding granules occur with certain preferences in mesogranular regions (e.g. Massaguer & Zahn 1980; Title et al. 1989) and during the emergence of magnetic field and its subsequent accumulation within mesogranular borders (Simon et al. 1988; Domínguez Cerdeña 2003; Ishikawa & Tsuneta 2011).

* Movie attached to Fig. 1 is available at <https://www.aanda.org>

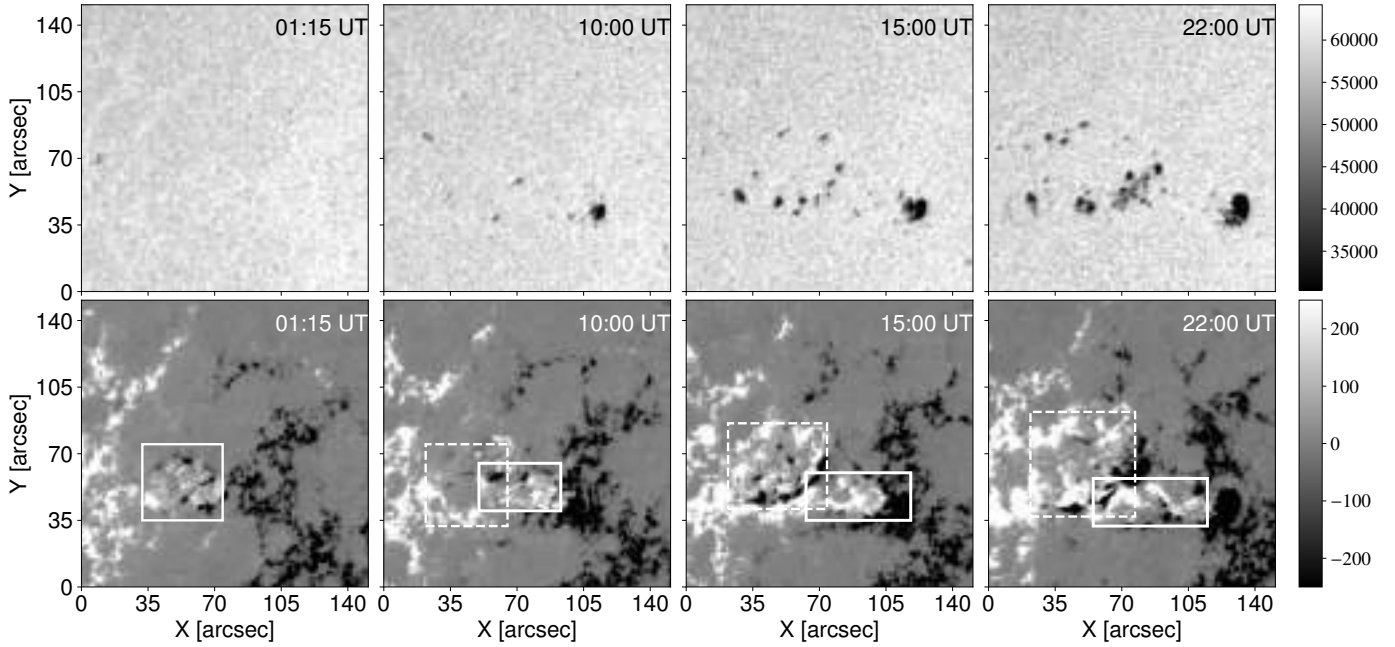


Fig. 1. Selected active region (AR) as observed on April 11, 2011 exhibits a complex configuration with sunspots harbouring partial penumbras and pores. *First row:* time evolution of the continuum images for AR 11190 that displays a rapid evolution. *Second row:* series of LOS magnetograms for AR 11190 with positive and negative (white and black) magnetic polarities used to track the evolution of emergent positive magnetic field. The solid box encloses the region of an initial positive magnetic emergence, while the dashed box outlines a second emergent cell evolving faster and thus pushing and suppressing the first emergence. The colour bar in the first row displays the intensity values clipped between 45% and 95% of the image featuring the largest intensity, whereas the colour bar in the second row shows the LOS magnetic field maps clipped in the range between -250 and $+250$ Gauss. A clearer understanding can be obtained by watching the full evolution of the active region in the movie provided, which shows the magnetic field on a false colour table from -2500 G to $+2500$ G, and the continuum maps normalized over the average of all the maximum (see [online](#) movie).

In this paper, we focus on the behaviour of such large-scale granular cells within the region of interest (ROI) and at the time when National Oceanic and Atmospheric Administration (NOAA) active region 11190 is formed. Such detailed studies were not possible, due to the lack of highly resolved, long, and sufficiently stable time series for the detailed investigation of the formation of an active region over days on spatial scales down to the granulation. With highly sophisticated space instruments like the Solar Dynamics Observatory (SDO, see [Pesnell et al. 2012](#)), used in this study, we can follow the long temporal evolution necessary for the formation and dissolution of whole active regions.

For the detailed flow investigations performed in this study, we need to identify the proper surface motions. Several authors have studied these kinds of proper motions using different approaches (e.g. [Hurlbert et al. 1995](#); [Simon et al. 1995](#); [Welsch et al. 2004](#); [Schuck 2006](#)). Among the most widely applied methods is the so-called local correlation tracking (LCT) technique. LCT was employed for the calculation of proper motions of the solar granulation for the first time by [November et al. \(1986\)](#), and subsequently by [November & Simon \(1988\)](#). The algorithm is based on finding the best cross-correlation between two consecutive images. It is well known that LCT can produce some errors due to the method itself when it measures the intensity changes as these changes can be related to plasma motions but also may reflect phase velocities (e.g. [Roudier et al. 1999](#); [Potts et al. 2003](#)). In addition, LCT may produce errors through phenomena such as the shrinking-sun effect ([Lisle & Toomre 2004](#)) caused by large stationary flows. However, one can correct for these errors and thus such artefacts can successfully be removed by subtracting the time average of the velocities from the flow maps. Some authors

(e.g. [Yi et al. 1992](#); [Molowny-Horas 1994](#); [Verma et al. 2013](#); [Louis et al. 2015](#); [Asensio Ramos et al. 2017](#)) have shown that in the worst cases the underestimations of velocities may amount to 20–30%.

2. Data and pre-processing

In this study we use time series of imaging data showing the formation and evolution of active region (AR) 11190. The data were acquired by the Helioseismic and Magnetic Imager (HMI) instrument ([Hoeksema et al. 2014](#)) on board the SDO spacecraft comprising continuum maps and line-of-sight (LOS) magnetograms.

The studied AR 11190 is shown in Fig. 1, and comprises the formation stage during the time interval for the whole 24 h on April 11, 2011 in continuum as well as in LOS magnetic field. The maps are acquired with a cadence of 45 s and a pixel resolution of ~ 0.504 arcsec (roughly 350 km) for both observable quantities (continuum, LOS magnetic field). As these data come already prepared at level 1.5, no primary data reduction such as flat fielding and dark current correction is necessary.

Figure 1 shows four different instances prior to the formation of AR 11190 in continuum and LOS magnetic field images. The video linked to the web url mentioned above shows clearly the emergence of the first magnetic bubble ([Ortiz et al. 2014](#); [de la Cruz Rodríguez et al. 2015](#)), and then a second even faster and more powerful magnetic emergence starts to occur, lifting more positive magnetic flux to the surface and pushing the previously emerged flux to the right.

The faster emergence is seen even more clearly in the evolution of magnetograms compared to the observations in the

continuum data. In this LOS magnetogram, a solid box (see second row in Fig. 1) encloses an initial positive magnetic field emergence, which starts during the first hours of the day, whereas a dashed box encloses the second magnetic emergence. The LOS maps displayed in the figure were clipped in the range $[-250, 250]$ Gauss.

Moreover, Fig. 1 (LOS maps) shows pre-existent positive and negative magnetic field regions. When the first magnetic bubble appears within the field of view (FOV), the positive and negative magnetic elements further away from the site of emergence (constituting in some way the background magnetic environment) do not change noticeably. At the same instant that the second magnetic bubble starts to emerge, it pushes the first emergence away from the location of newly emergent flux. Thus, soon after, all the previously emerged magnetic elements are pushed in the same right direction towards the negative magnetic elements. These magnetic elements in turn start to accumulate at certain locations, increase there in magnetic flux, and evolve for the first time into small magnetic pores that later on become the fully evolved AR 11190.

The software used for reducing HMI data (e.g. derotation, coalignment, and subsonic filtering procedures) was encoded in the Python language making use of the solar physics library named Sunpy (Mumford & Christe 2015). A graphical user interface (GUI) has been developed to facilitate the detection and application of the LCT method (see Campos Rozo & Vargas Dominguez 2014)¹. The ROI was chosen manually in such a way as to centre on the location where the emergence of fast and highly notable large-scale granules is happening. The size of the analyzed FOV is $150'' \times 150''$. All images were aligned and a subsonic filtering with a phase-velocity threshold of 4 km s^{-1} was applied to subtract the solar 5 min oscillation (November et al. 1981; Title et al. 1989). Moreover, due to the Sun being a hot plasma sphere and the sunspot locations spreading along different regions on the solar disc, flow map velocity components were properly deprojected (see Vargas Dominguez 2009, and references therein).

3. Results

We focused on the formation and emergence of AR 11190, and investigated in detail the evolution and behaviour of the plasma and magnetic field dynamics from horizontal and vertical velocities for different time ranges. The LCT technique applied is based on Eq. (1) proposed by November & Simon (1988),

$$C_{t,t+\tau}(\delta, \mathbf{x}) = \int J_t \left(\zeta - \frac{\delta}{2} \right) J_{t+\tau} \left(\zeta + \frac{\delta}{2} \right) W(\zeta - \zeta) \partial\zeta, \quad (1)$$

where $C_{t,t+\tau}(\delta, \mathbf{x})$ is a four-dimensional function depending on two consecutive images, the displacements between these images, and the localization of the apodization window $W(\mathbf{x})$; and J_t , $J_{t+\tau}$ are the intensity of the images at two consecutive time steps t and $t + \tau$. It is worth mentioning that the velocities estimated by LCT are not exclusively plasma motions but strictly speaking horizontal proper motions as the algorithm does not use plasma physical properties. The LCT algorithm applied in this work (see Yi et al. 1992; Molowny-Horas 1994) was adapted in Python to calculate the velocity fields using an apodization window adjusted for the comparable size of the features to be tracked. Authors such as Palacios et al.

(2012) have shown that the emergence of new magnetic flux as well as posterior AR formation are associated with explosive mesogranules.

For that reason we have chosen a full width at half maximum (FWHM) parameter of 12.5 arcsec (~ 9 Mm) corresponding to typical average sizes of ensembles of granules forming the mesogranular pattern, and a temporal averaging period of 2 h (average lifetimes for large-scale granulation patterns; see Hill et al. 1984; Rast 2003). These 2 h correspond to 160 frames in the data set². Vertical velocities are computed by the divergence from the horizontal velocities v_x and v_y obtained by the LCT algorithm via the idea of flux conservation (see November & Simon 1988; Márquez et al. 2006; Vargas Dominguez 2009) leading to the expression

$$v_z(v_x, v_y) = h_m \nabla \cdot v_h(v_x, v_y), \quad (2)$$

where h_m is a constant of proportionality representing the mass-flux scale height with a value of 150 ± 12 km (see November et al. 1987; November 1989). The flow maps are then plotted over these vertical velocities obtained from continuum maps as well as from magnetograms.

3.1. Horizontal and vertical flow maps

The studied AR shows exploding mesogranules in locations where the formation of the active region, as seen by a complex sunspot group, is initiated. There is a strong connection between the appearance of these emergent large-scale granules and rapid vertical upflows emerging from the same region.

Even when AR 11190 does not show strong emergences in the continuum maps, a strong emergence of positive magnetic field elements can be clearly observed in the magnetograms. Horizontal and vertical flow maps of proper motions as well as of magnetic field elements were calculated with the LCT algorithm to link the photospheric plasma dynamics with the magnetic field evolution.

Figure 2 shows the evolution of the magnetic flux and plasma emergence during the formation of AR 11190 as well as the behaviour of the plasma and the movement of the magnetic elements as observed in the LOS magnetograms at four different time. The horizontal and vertical velocities are plotted in each panel showing the behaviour and giving information about the proper motions of the plasma and the magnetic elements during the appearance of AR 11190.

The first panel displays the evolution and behaviour of the continuum maps. The horizontal velocities are represented by the arrows overplotted in the ROI, whereas the vertical velocities are represented by the background image. These velocities reveal several divergences at the following positions: $(x'', y'') = (70, 30), (30, 5), (70, 70)$, or $(50, 130)$.

We focus now on the emergence centred on the position $70'' \times 70''$ as it displays a comparably more rapid emergence of strong, as well as weak, positive magnetic field elements, as evidenced in the second row at the same location, which can be found at the other emergence sites. Although the other emergences indicate a certain correspondence of vertical motions between plasma and the LOS magnetic elements, they do not display horizontal motions of positive magnetic elements greater than 10 Gauss (lower limit used in the present work) emerging in those regions.

¹ The code can be found at <https://github.com/Hypnus1803/FlowMapsGUI>

² We wish to remark that given UT times on the images always correspond to the first image of such 160 images containing subsets.

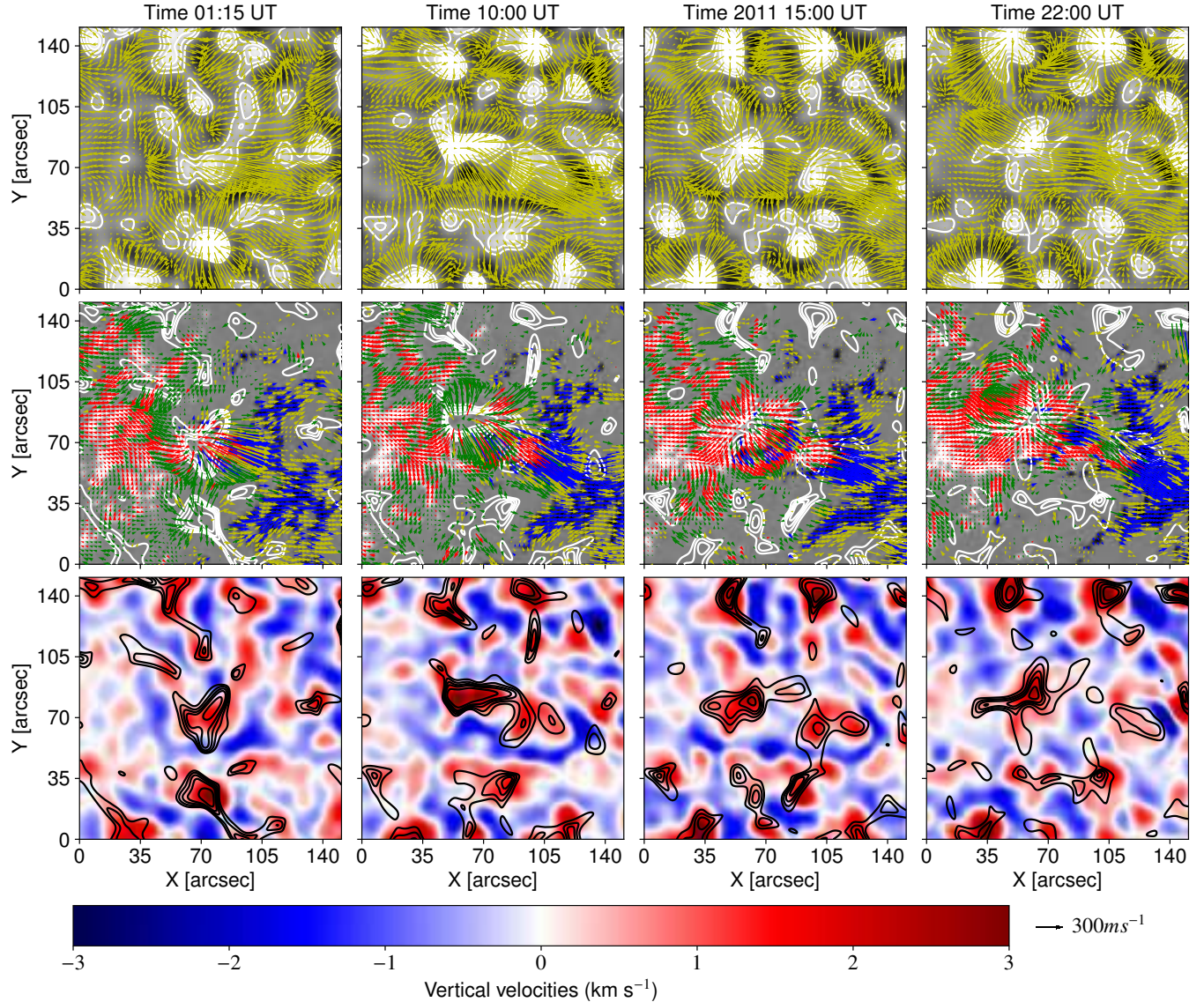


Fig. 2. Temporal evolution of the velocity fields within the ROI of AR 11190 at four different times computed by local correlation tracking (LCT) analysis. Horizontal and vertical velocities are inferred from continuum maps as well as from LOS magnetic field maps. *Top row:* horizontal proper motions (calculated by LCT technique applied to the continuum maps) with the background image being the vertical velocity map, and the contour lines representing positive vertical velocities with contour values of $[0.5, 1., 1.5, 2., 3] \text{ km s}^{-1}$. *Second row:* horizontal velocities of magnetic elements (calculated from LCT analysis over the LOS magnetograms) where the background image represents the LOS magnetic field strength map and the contour lines are ranged as before. The red arrows show the motions of magnetic elements with magnetic strengths greater than 50 Gauss, and the blue arrows display the average movements of negative magnetic elements with values lower than -50 Gauss . The green arrows display horizontal behaviour for weak positive magnetic elements, whereas the yellow arrows display the horizontal proper motions associated with weak negative magnetic field elements. *Third row:* comparison between the evolution of vertical velocities obtained from the continuum data set and the evolution of positive vertical velocities obtained from the LOS magnetic field data. The black arrow in the bottom right corner represents the length of a velocity vector featuring a magnitude of 300 ms^{-1} .

Before the appearance of the second emerging bubble, the motions of the magnetic elements follow the paths imposed by the plasma horizontal motions as well as the up- and down-flows. When the second magnetic emergence starts to appear, the proper motions seem to follow the new paths imposed by the new strong positive magnetic field elements, displaying a preferred motion in the positive x -direction (see also additional online movies). In the first row of Fig. 2, the contour lines show positive vertical velocities enclosing magnitudes of $[0.5, 1., 1.5, 2., 3] \text{ km s}^{-1}$ calculated from the continuum data set.

The second row in Fig. 2 features plotted contours of the vertical velocities calculated from the LOS magnetic field data

using the same contour values mentioned before. This panel shows also the horizontal motions of positive and negative magnetic elements in the LOS maps. It is possible to identify the moment when the second magnetic emergence starts to appear (row = 2, column = 2). This emergence shows fast motions but only associated with weak positive magnetic field elements that turn later into strong magnetic field elements.

In order to compare the dynamics of plasma and magnetic elements, Fig. 2, third row, shows in the background the vertical velocities from the continuum data set as well as overplotted contour lines representing the positive vertical velocities calculated from the LOS magnetic data cube. Although all vertical

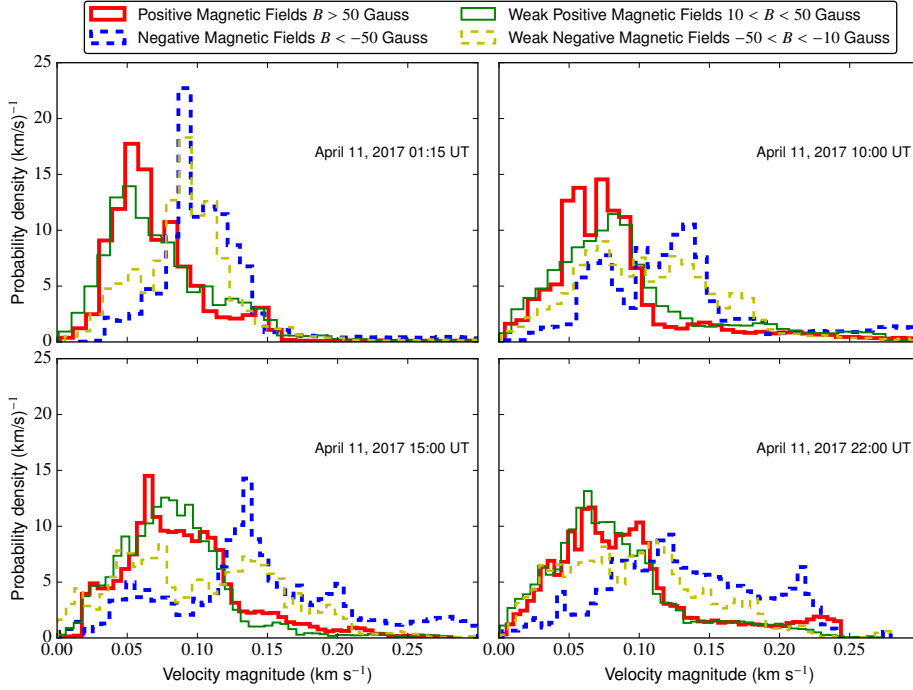


Fig. 3. Distribution of magnitudes of velocities ($v = \sqrt{v_x^2 + v_y^2}$; speeds) for weak and strong magnetic fields for the times shown in Fig. 2. Red and blue colours (thick lines) describe the velocity distributions for positive and negative magnetic fields greater than 50 Gauss, whereas green and yellow (thin lines) distributions represent the motions of the weaker magnetic elements. The ranges for both the weak positive and negative field strengths are $[10 < B < 50]$ and $-50 < B < -10$ Gauss. Here, B is the magnetic field strength as obtained from the magnetograms. The solid lines represent the positive magnetic polarity, whereas the dashed lines represent the negative magnetic fields.

velocities calculated from magnetic LOS elements are linked to plasma vertical velocities, the best observational correlation is registered for the emergence located in $70'' \times 70''$. Both flow patterns seem to evolve at the same rate and look alike.

However, to have an even more robust and quantitative overview of the ongoing and evolving flows, we will now have a detailed look at the distribution of the magnitudes ($\sqrt{v_x^2 + v_y^2}$; hereafter called speed) separated for the previously mentioned strong and weak fields, as well as for the two polarities.

The resulting distribution of speeds for the same four time instances (at the beginning of the first emergence, during the second emergence, after the second emergence, and to the end of the evolution) can be seen in Fig. 3. At the beginning of the first emergence (left upper panel) one can see a separation of the positive and negative polarities.

While the distributions for the positive magnetic field elements look more or less Rayleigh distributed (indicating a two dimensional freely, i.e. randomly, outflowing region), the same distribution for the negative magnetic elements features the appearance of a normal distribution, but offset from zero by a certain constant velocity, indicating a movement leading to a separation for the two polarities, where the negative magnetic elements tend to move towards the right side of the FOV. During and just after the second emergence (panels 2 and 3 in Fig. 3) the distributions seem to be truncated and merging at horizontal velocities of around 0.12 km s^{-1} . This behaviour can be explained by the idea that the created positive magnetic elements catch up with the negative elements towards the right side. After catching up, these negative elements then hinder the positive ones in moving faster. Thus the positive distribution gets truncated at higher velocities while the distribution for negative elements becomes truncated for low velocities as the positive elements push into the slowest negative ones thus either accelerating them to the same speed or annihilating them when they catch up. The last panel in Fig. 3 (lower right one) shows the evolved FOV where both kinds of magnetic elements seem to

approach very similar distributions and thus move and evolve together again.

Figure 4 displays the speeds of the horizontal proper motions (red dashed line) and the horizontal movements of magnetic elements (blue and solid line; now regardless of their polarity and strength). The upper panels in Fig. 4 show a correspondence between the plasma and magnetic field distributions, which means that both are moving following the same behaviour. As they are evolving (bottom panels), the velocity distribution of the magnetic elements shows an increase in its mean value, whereas the mean velocity obtained from the proper motions appears to decrease in value most likely being suppressed by the stronger magnetic fields. Due to the physical processes creating the flows, the best description of the distribution of speeds is generally given by a Rayleigh distribution (Eq. (3))³,

$$f(v, \sigma) = \frac{v}{\sigma^2} \exp\left(\frac{-v^2}{2\sigma^2}\right), v > 0, \quad (3)$$

where the scalar factor σ is associated with the mean velocity of such a distribution (Hoffman et al. 1975). The mean velocity for a quiet small region, using temporal averages of 2 h, is $v_{\text{Int}} = 72 \pm 8.8 \text{ ms}^{-1}$ for the continuum maps, whereas for LOS magnetogram data the value amounts to $v_{\text{LOS}} = 54 \pm 10.7 \text{ ms}^{-1}$. However, when the mean velocity is calculated over the chosen ROI, the horizontal proper motions obtained from the magnetic elements data ($v_{\text{LOS}} = 65 \pm 2.2 \text{ ms}^{-1}$) appear to be slightly larger than the continuum proper motions ($v_{\text{Int}} = 55 \pm 2.5 \text{ ms}^{-1}$). This difference can be explained by the second faster emergence of magnetic field. During this emergence the plasma takes some time until it starts to feel the influence of these new magnetic fields that emerge faster than the first appearance and start to push the old magnetic elements. In the photosphere most of the plasma is, due to the comparably low temperatures, in a neutral state. Thus, in the beginning of the flux emergence, only the

³ Mathematically, a Rayleigh distribution for the magnitude of a two-dimensional vector is formed when both vector components follow 0-centred normal distributions with equal σ (standard deviation), which is common for random walk processes (convective flows).

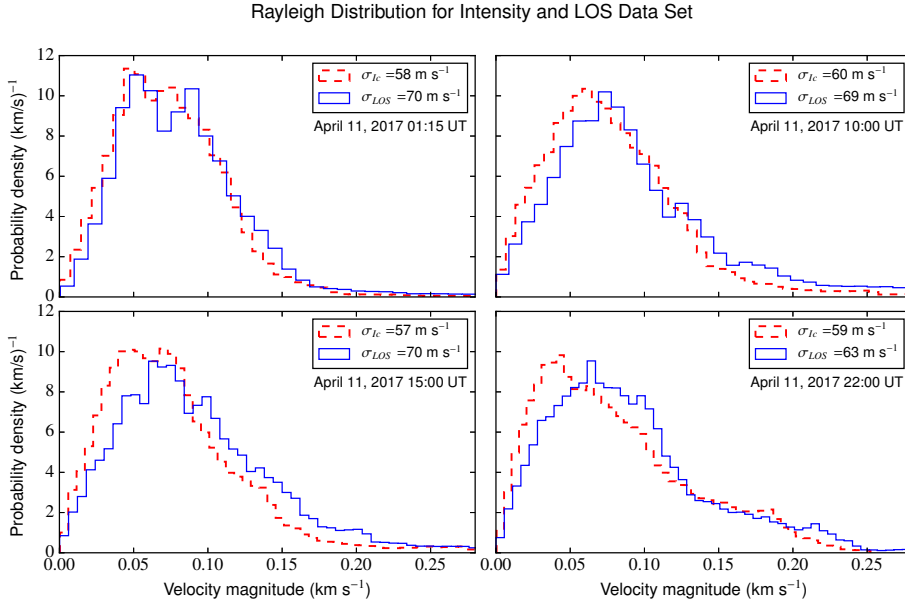


Fig. 4. Distribution of speeds. The red dashed line shows the distribution of v for the proper motions, whereas the blue and solid line shows the distribution of magnetic elements motion. The scale factor σ is associated with the mean velocity in this distribution.

present ions will react immediately, while some time is needed to transfer the momentum from the ions to the neutral gas. Therefore the proper motions linked to the continuum maps and their velocity distributions can lag behind the distributions of the magnetic elements. Besides, we have to have in mind that the formation height for the continuum maps can be slightly different from the formation height of the magnetograms. The existence of a strong concordance between both distributions, continuum and magnetic elements motions, is nevertheless evident even though the magnetic elements move horizontally slightly faster than the horizontal motions computed from continuum maps.

3.2. Distribution analysis

Figure 4 shows, for the velocity distribution of the magnetic field elements, distinct enhancements variable in position as well as amplitude. Due to this behaviour, we introduce and consider a combined distribution model made up of two components. While the major part of the histogram follows a Rayleigh distribution (first component) representing undisturbed quiet background flows, the second component will be generally related to the flux emergence process creating, for example, a tail of high velocity measurements. In addition to the increased velocity tail, it is also possible that during the flux emergence a bifurcation of the velocity distribution happens due to different velocity distributions for the two magnetic field polarities, meaning that one kind of magnetic element moves with a different characteristic speed than the other. Thus the bumpy nature can be explained by the flux emergence process and/or a bifurcation of the underlying velocity distributions for the two magnetic polarities. Due to the unknown nature of the second distribution, we will employ fitting tests with a combination of either two Rayleigh distributions (see Eq. (4)) or a combination of one Rayleigh component and one Gaussian component (see Eq. (5)):

$$f(v, \sigma_{R_1}) + f(v, \sigma_{R_2}) = A_1 \cdot \frac{v}{\sigma_{R_1}^2} \exp\left(\frac{-v^2}{2\sigma_{R_1}^2}\right) + B_1 \cdot \frac{v}{\sigma_{R_2}^2} \exp\left(\frac{-v^2}{2\sigma_{R_2}^2}\right), \quad (4)$$

$$f(v, \sigma_{R_3}) + f(v, \mu_G, \sigma_G) = A_2 \cdot \frac{v}{\sigma_{R_3}^2} \exp\left(\frac{-v^2}{2\sigma_{R_3}^2}\right) + \frac{B_2}{\sqrt{2\pi}\sigma_G} \exp\left(\frac{-(v - \mu_G)^2}{2\sigma_G^2}\right). \quad (5)$$

In these equations σ represents either the previously introduced scalar parameter of a Rayleigh distribution or the standard deviation in the case of the Gaussian. Constants A_x and B_x are the amplitudes or weighting parameters for the two components of the distribution with $x = 1$ representing the double Rayleigh distribution and $x = 2$ corresponding to the Rayleigh and Gaussian combined distribution. Finally, μ_G represents the mean value of the Gaussian distribution. By applying such a model, we would implicitly assume that the flux emergence leads in a part of the FOV to a secondary Rayleigh distribution or a Gaussian one most likely featuring higher velocities than the background flow distribution.

Three test cases at different time instants of such two-component modelling of the flows in the FOV of the flux emergence are shown in Fig. 5. The upper part of the figure shows a set of six panels created from the LCT analysis of magnetograms. The first row of these panels shows the combination of two Rayleigh components while the lower row shows the combination of a Rayleigh component and the Gaussian distribution. The lower set of panels is arranged in the same way but created from the LCT analysis of the continuum maps. These three cases were chosen visually from Fig. 6a at times that showed remarkable changes in the evolution of the depicted parameters. In these three test cases it becomes clear that sometimes the combination of two Rayleigh components fits better, while in other cases the combination of a Rayleigh component with a Gaussian component gives a better fit.

From these modelling efforts, we can learn that it is not straightforward and clear whether the additional component should be of Rayleigh or of Gaussian type. For instance, for the speed histograms created from the continuum maps as depicted in the first column, it is easy to observe that the combination of a Rayleigh distribution with a Gaussian distribution fits better compared to the combination of two Rayleigh distributions. This is also true for the distribution created by the LOS

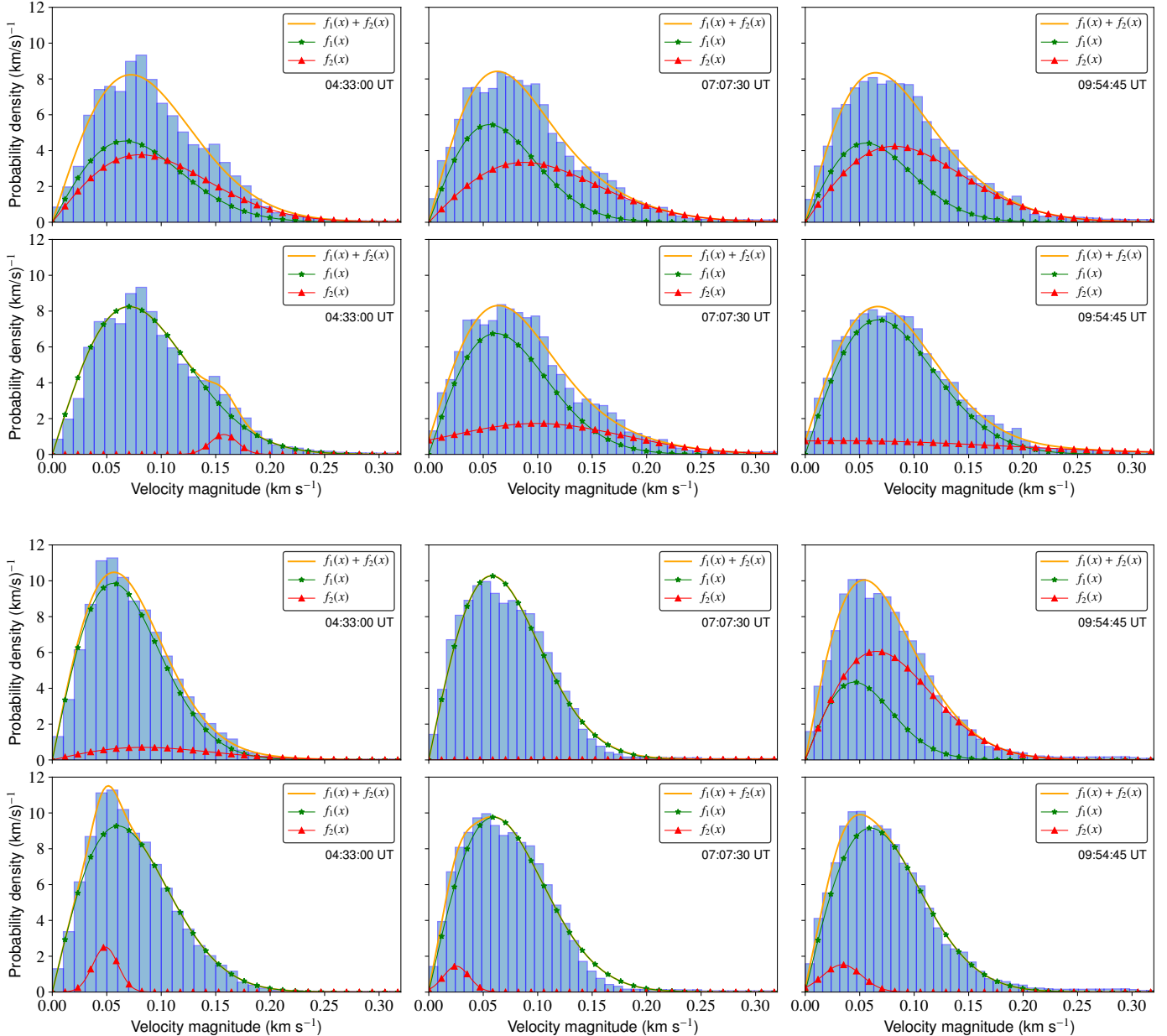


Fig. 5. Plots show three test cases for the proposed combination of two-component distributions for the continuum flow maps (*lower set of panels*) as well as for the magnetic elements motions (*upper set of panels*). First row in both six panel sets: case of combining two Rayleigh distributions for the total fit. They display the two independent Rayleigh components as well as the sum of the two components to form the whole measured velocity distribution for three different times. Second row for each: case of the combination of a Rayleigh background component with a variable Gaussian component. Times are in universal time (UT).

magnetic field data set. The middle column of distributions created from the magnetograms as well as continuum maps seem to be equally well fitted by both kinds of combined distributions, while the last column shows that the distributions would be better fitted by the two Rayleigh components combination. The second finding is that clearly the amplitude of the secondary component is variable in position as well as in amplitude.

We do not wish to introduce a model with too many free parameters and thus we will continue with these models that only comprise the mentioned two components. However, to shed more light on the goodness of these combinations, we will now investigate in more detail the temporal evolution of the parameters of such two-component models. Later, we will then also study the goodness of the fit of the combined models to ascer-

tain which one is more likely to represent the flows in the FOV during flux emergence events.

Figure 6 displays an example of how the fit parameters behave during the time evolution on April 11, 2011. The left column shows the behaviour for the LOS magnetic field data set, whereas the right column gives the information about the proper motions obtained from the continuum maps. Figures 6a and b present the parameters A_1 , B_1 , σ_{R_1} , and σ_{R_2} , calculated using a python least-square algorithm for the case of applying the sum of two Rayleigh distributions (Eq. (4)) for the LOS data set, as well as for the continuum data. Parameter σ_{R_1} is related to the background velocity at those places of the ROI where the plasma or the magnetic elements are not affected by flux emergence. One can clearly observe in Fig. 6a the existence of three

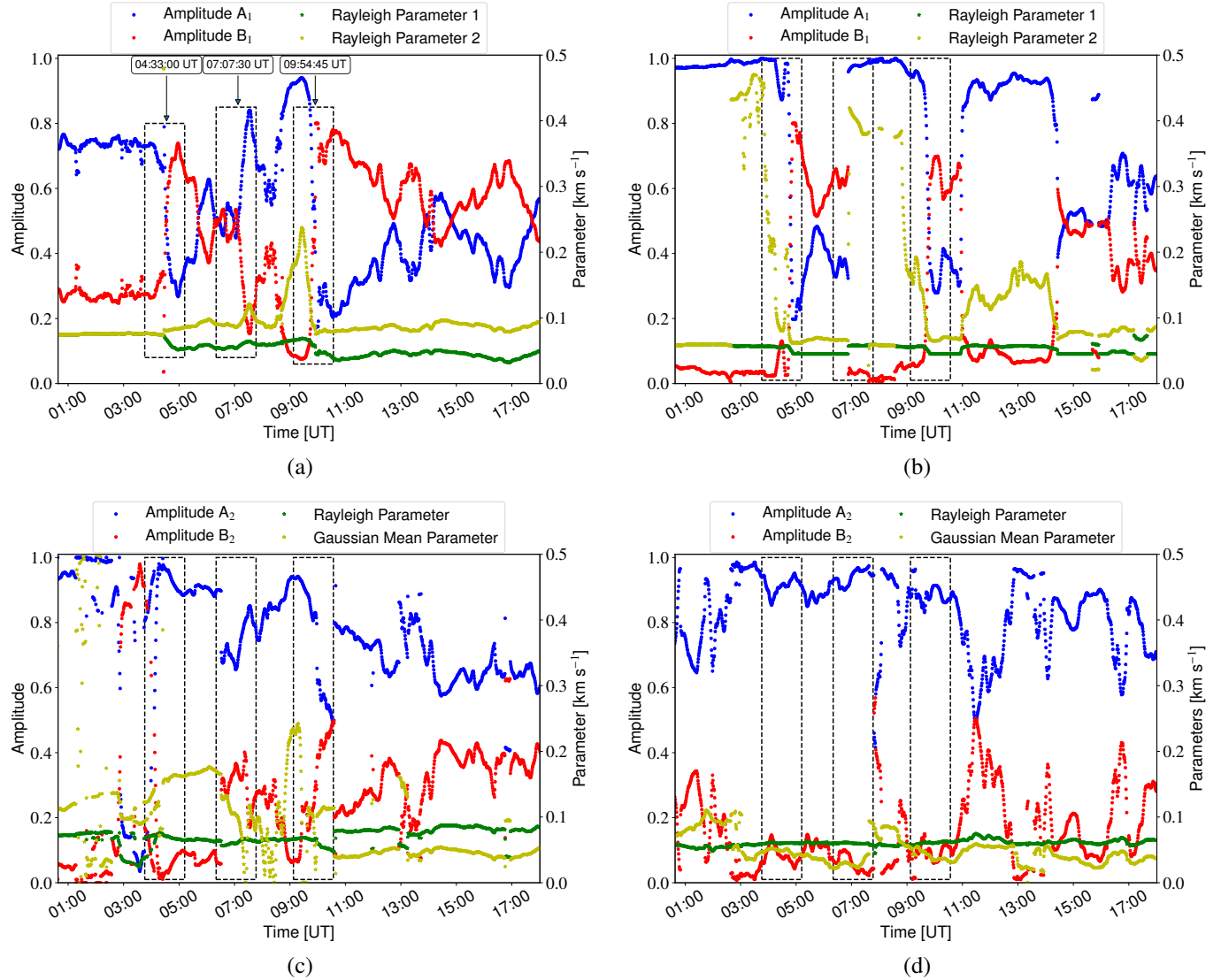


Fig. 6. Temporal evolution of the parameters associated with the proposed distributions in Eqs. (4) and (5). *First row:* behaviour of the parameters for the sum of two Rayleigh functions. *Second row:* time evolution for the combination of one Rayleigh function and one Gaussian function. The temporal evolution followed by the amplitudes (dimensionless – left axis) is plotted with circle markers, whereas the temporal evolution for the functional parameters are shown with star markers (right axis in km s^{-1}). The blue and green markers are associated to the first Rayleigh function component in both proposed distributions, whereas the red, and yellow markers represent the second component, which is either a second Rayleigh function or a Gaussian function. The left side of the panels are calculated from the LOS magnetograms, whereas the right side panels are obtained from the continuum maps. The dashed rectangles enclose the three time instants shown in Fig. 5.

strong deviations at three different times (marked dashed rectangles, and their respective times) that affect all the parameters at the same time (see also discussion above). It is easy to observe in Fig. 6a how, at the beginning of the evolution, σ_{R_1} and σ_{R_2} appear to have the same value, which means that the FOV is governed by a single type of background motion and is not yet affected by the first magnetic emergence. At 04:33 UT, the behaviour changes drastically showing a splitting between the σ_{R_1} and σ_{R_2} parameters. Moreover, the amplitude B_1 becomes larger than the amplitude A_1 giving more importance to the second component at this moment of evolution. The second time shows a small enhancement of the Rayleigh parameter for the second component. However, in this instance the amplitude A_1 becomes greater than B_1 . This change may be associated with the beginning of the second magnetic emergence. The third and the strongest change in the Rayleigh parameters related to the second distribution happens at 09:54:45 UT. At this point the second

magnetic emergence becomes more active, associated with an increased number of positive magnetic field elements. Figure 6b, which shows the evolution of the Rayleigh combination for the continuum maps (horizontal proper motion), shows clearly several parameter jumps at the same times, although the behaviour in general of the parameters looks more chaotic. However, one can observe that the splitting between both Rayleigh parameters happens already earlier for the horizontal proper motions compared to the flows obtained from the magnetic elements. The combination between a Rayleigh and a Gaussian distribution for the magnetic motions (Fig. 6c) shows in general that the Gaussian mean value is larger than the Rayleigh parameter. However, this behaviour changes after the third marked time (dashed rectangle), when the Rayleigh parameter becomes larger than the Gaussian mean. Contrary to these statements, Fig. 6d seems to show that in general the Rayleigh parameter governs the behaviour of the continuum horizontal proper motions except

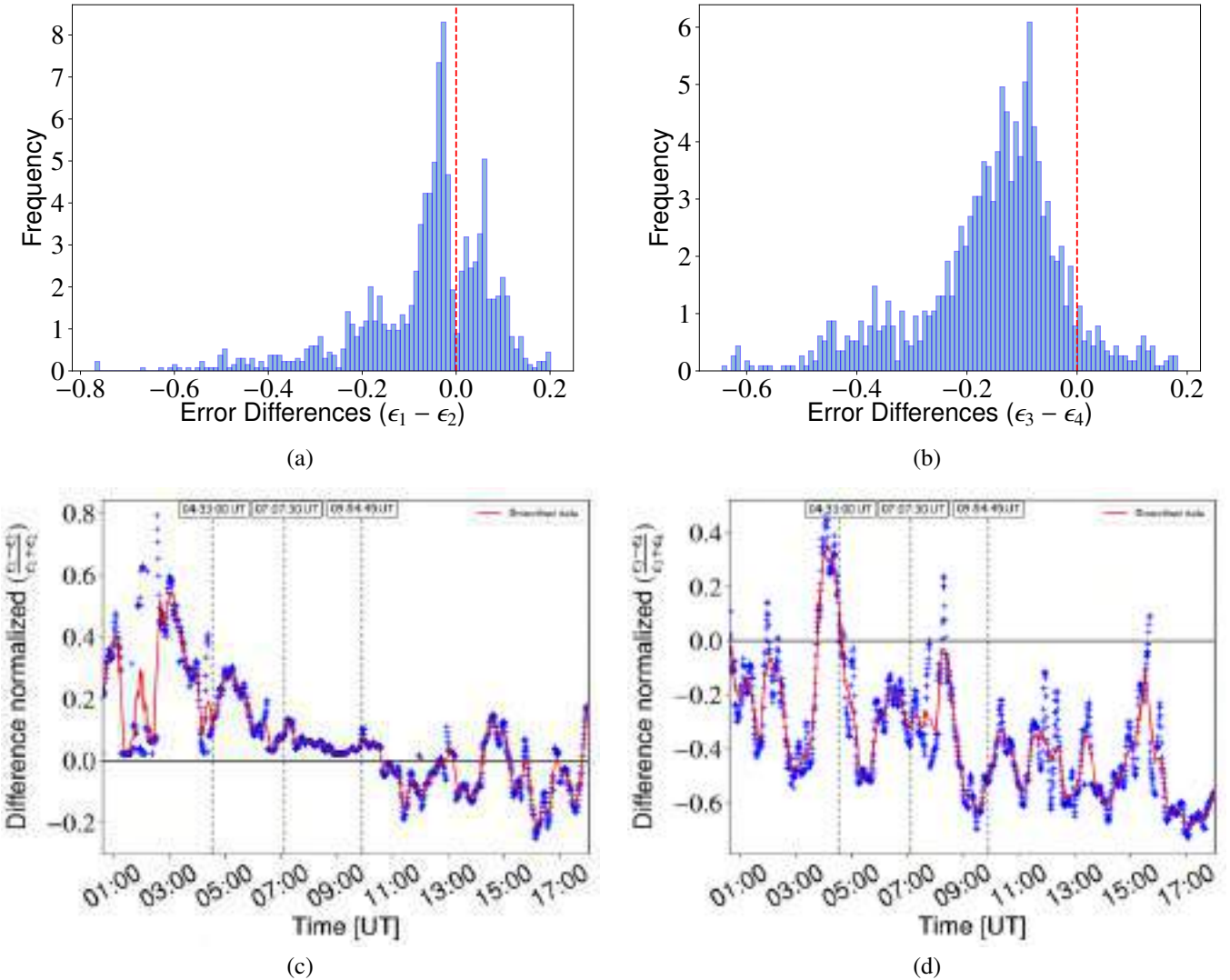


Fig. 7. Normalized reduced χ^2 value (ϵ_i) was calculated for the two fitting combinations to decide the goodness of a fit, that is, which combination of functions would fit the flow maps better. *Panels a and b:* distribution for the difference between ϵ_1 and ϵ_2 , for the distributions obtained from the LOS magnetograms, as well as for the difference between ϵ_3 and ϵ_4 , for the distributions obtained from the continuum maps. Normalized reduced chi squared values ϵ_1 and ϵ_3 are related to Eq. (4), whereas ϵ_2 and ϵ_4 are related to Eq. (5). *Panels c and d:* temporal evolution of the changes of these differences between corresponding ϵ_i .

at certain times that are not obviously correlated to the changes mentioned before. In general, the amplitude A_2 is greater than B_2 , implying that the contribution of this fit component to the overall speed histogram fit is marginal.

To decide which of the proposed two-component functions fits the data better, a quality test for the goodness of fitting must be done. In a first step, we compared statistically the goodness of fitting of the two models with each other. For this purpose, we obtained the normalized reduced χ^2 values⁴ for both combinations of fitting functions, as well as for the LOS magnetic field data and continuum maps, namely the parameters ϵ_1 and ϵ_2 , as well as ϵ_3 and ϵ_4 for i) the sum of the two Rayleigh functions and ii) the combination consisting of one Rayleigh and one Gaussian function, respectively. Then we subtracted the two χ^2 values from each other, $\epsilon_1 - \epsilon_2$ and $\epsilon_3 - \epsilon_4$, respectively, and created a histogram plot for this difference. The result can be seen in the upper panel of Fig. 7.

⁴ Normalized means in this context that the values were normalized to the maximum chi square number obtained during the considered time evolution.

The vertical red dashed line in Figs. 7a and b marks the zero line which in principle should separate the two domains of preferential fitting for the two different models. The distributions obtained from these differences between ϵ_1 and ϵ_2 , as well as between ϵ_3 and ϵ_4 , deduced from the magnetic field and continuum data, show two different regions. It is clearly observable in Fig. 7a that the zero line divides the distribution in two distinct regions. For values larger than 0, the best fitting is given straightforwardly by the sum of one Rayleigh function and a Gaussian function, whereas for values lower than 0 we would argue that clearly the best fitting can be obtained via a combination of two Rayleigh distributions for the LOS magnetic field data. Accordingly, we can see in Fig. 7b that the difference between ϵ_3 and ϵ_4 is normally distributed, and shifted to negative values indicating that in general the better fitting could be obtained by the combination of two Rayleigh components.

Figures 7c and d show the temporal evolution for $(\epsilon_1 - \epsilon_2) / (\epsilon_1 + \epsilon_2)$ and $(\epsilon_3 - \epsilon_4) / (\epsilon_3 + \epsilon_4)$, which can be interpreted as a “quasi-polarization” between both combinations and thus gives information about the

times when which combination would actually fit the obtained velocity distribution better. Figure 7c shows that previous to the first time instant (04:33 UT), the best fitting is given by the combination of one Rayleigh and a Gaussian distribution. After the second time instant (07:07:30 UT), even if the values are over the zero line, it is possible to argue that both combinations fit equally well. Then, after the third time instant (09:54:45 UT), the evolution shows that the best fitting is given by the combination of two Rayleigh distributions. On the other hand, Fig. 7d shows that in general for the continuum horizontal proper motions, the distributions will be well fitted by the combination of two Rayleigh distributions, with the exception of some isolated short time instants that appear to coincide with the previously outlined three special points of time we already discussed in Fig. 6. On this occasions it appears that the best fitting is given using the combination of one Rayleigh and one Gaussian distribution.

4. Discussion

In this work we have analysed time series of images displaying the formation of a solar active region in both continuum maps and LOS magnetograms. Results expose the presence of large-scale granular cells prior to the formation of the active region. The horizontal proper motions show strong outflows (divergences) at the same places where strong upflows can be identified. Although the calculated vertical velocities show upflows in different sectors within the FOV, these emergences do not exhibit strong and remarkable horizontal velocities. Besides, such upflows are generally only related to the appearance and motion of weak magnetic fields (<10 Gauss). This is in strong contrast to the horizontal velocities detected roughly in the centre of the FOV. Here it seems as if the strong upflows are also associated to the formation of AR 11190. Generally we would like to state that the behaviour of the continuum proper motions and the magnetic field element motions are strongly linked. This becomes also very clear in the third row in Fig. 2, where both the vertical velocities obtained from the horizontal velocities (background map) and the contours resulting from the positive vertical velocities obtained from the LOS magnetic field data are depicted together and display a strong correlation. This can be clearly seen by applying a Pearson correlation analysis between the vertical velocities from continuum maps and from the LOS magnetic field.

Figure 8 shows exactly such calculated correlation and its temporal evolution. The vertical dashed lines represent the same instants as mentioned in the Fig. 6. All of them are close to points where the Pearson coefficient evolution changes its slope. In Fig. 8 we can see how the correlation starts at a value of around 0.65 indicating a good correlation before dropping at 2:00 UT to a local minimum. This means that in the beginning of the time series the plasma flows and the magnetic field element motions are well coupled. However, during the first magnetic emergence, the motions become partly decoupled. This can be due to the idea that in the first moment the newly emerging magnetic field is so powerful and strong that it can weaken the coupling conditions for a moment, expand faster than the local surrounding plasma, and only slightly later start also to push away the plasma. From about 3:00 UT to 4:00 UT the coupling between the continuum proper motions and magnetic element motions are gradually restored, just to be broken again and even more strongly by the second emergence just after the first time instant mentioned above. This time the coupling gets even more weakened indicating a stronger emergence and stronger magnetic fields. Subsequently, after the second time instant, this leads in the

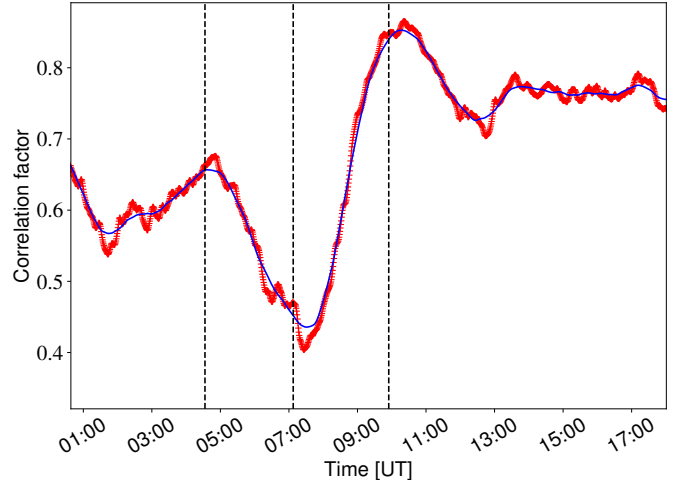


Fig. 8. Pearson coefficients for the vertical velocities in the region at the centre of the FOV. The size of the window was $90'' \times 65''$.

aftermath to a stronger coupling of the continuum and magnetic field element motions most likely due to the governance of the magnetic field over the plasma owing to the strong emergence. After the third time instant, the flows become more stable and reach a high plateau of coupling with a correlation coefficient of up to 0.75. Thus we would conclude that, at least during the emergence of the second magnetic bubble, the magnetic field was strong enough to govern the plasma flows, while in other cases normal convection might advect smaller magnetic elements.

Moreover, we can see in Fig. 8 that the maximum of correlation happens co-temporarily with the large parameter deviations as shown in Fig. 6a, identifiable in velocity distributions calculated for the magnetic field elements indicating again that the flow field is changing at these moments due to the emergence of new magnetic flux via the magnetic bubbles.

As we have seen and outlined in the results section, the velocity distributions, obtained from the flow maps, are well represented by the combination of two separate components. The proposed two different combinations as given by Eqs. (4) and (5) feature both a Rayleigh distribution, which we would think of as fitting the undisturbed background flows, that is, the regions of the FOV not affected by the flux emergence event, plus a second component, which is variable in position and relative strength as it applies for the occupied and effected area of the flux emergence process.

The open question to settle is, which one of the proposed components generally fits better? The Gaussian or the Rayleigh distribution? We believe that it might not be clear as there could be a kind of phase transition between both distributions. A Rayleigh distribution is formed for the magnitude of the velocity when both vector components x and y are Gaussian distributed (in the ideal case) with zero mean velocity and equal standard deviation, for example by a random walk process. Thus this kind of a distribution is also a good candidate for the background flow and it might be a good candidate during weak emergences in which the additional flow component still follows more or less a random walk but presumably with higher amplitudes. However, in the case of a strong flux emergence it is highly likely that all velocities in a larger and affected FOV area get directed away from the centre. Therefore, while the velocity amplitudes might still be stronger and weaker, in some way the distribution becomes one dimensional (only radially orientated away from

the centre of emergence) and hence the component representing the affected flux emergence pixels follows to a greater extent a Gaussian distribution instead of the Rayleigh one. A clearer insight could be gained by investigating in the future the formation of several active regions and looking then, with an even higher focus, on the velocity distributions to study these last details, as well as if and how, the secondary component changes.

After the detailed discussion of the results above, we wish to contextualize our work within the larger field of solar physics. The evolution of active regions is an ongoing research field, especially in regards to the build up of magnetic energy for solar eruptions, so-called flares (see e.g. Kilcik et al. 2018; Ye et al. 2018). This is generally done by having a detailed look into the magnetic field evolution as well as its configuration over time (e.g. Dacie et al. 2016). Such investigations are often directly performed by analysis of magnetograms but increasingly commonly also by magnetic field extrapolations (e.g. Thalmann & Wiegemann 2008). Another possibility for such analysis comes via simulations and modelling Cheung & DeRosa 2012. It is very clear that for a successful modelling of the process of energy build up, detailed knowledge about the velocity fields transporting the magnetic field above the solar surface, as well as shredding and twisting the field lines, is of great importance. The detailed measurement of flow fields, and derivation of the velocity distributions, are not only important for the evolution of the active regions themselves, but indeed also necessary for large-scale flux transport models such as the advective flux transport (AFT) model (see e.g. Ugarte-Urra et al. 2015). Thus a better knowledge of the velocity fields will also help in the understanding of the global dynamo acting on the Sun. Such flux transport models describe in a simplified way how the magnetic field emerges (e.g. in active regions), is shredded, and then transported via the velocity fields, including the meridional circulation and differential rotation, to the poles, where the fields finally get submerged. Thus a better parametrization of the velocity fields as done for example in this study will be of importance for such modelling efforts. A final interesting field for which this research might yield a new approach is the field of flux emergence studies. Authors like Golovko & Salakhutdinova (2015) have pointed out that flux emergence can be detected in image data by algorithms using sophisticated multi-fractal spectral analysis and segmentation. On the other hand, we have shown now that not only the structures within the FOV are changed (classically the granulation pattern gets elongated, which can be used within segmentation algorithms) but that the flow field changes remarkably leading to changed velocity distributions. Thus by investigating the flow field statistics, one can also detect and characterize flux emergence events.

5. Conclusion

In this paper we looked into the details of the evolving flow patterns in velocity maps during the formation of active region 11190. The used data were obtained from the SDO/HMI instrument as continuum maps and magnetograms to investigate both the continuum proper motions as well as the magnetic field element motions during two emergence events of positive flux leading in consequence to the formation of the active region. Generally we found a high congruence between the plasma flows and the motions of the magnetic elements. This congruence is weakened and distorted during the emergence of new magnetic flux. Moreover, the speeds in the FOV can be fitted in general very accurately with a Rayleigh distribution. Nevertheless, during the flux emergence events the Rayleigh distributions get distorted and at least a secondary flow field com-

ponent should be added. It is plausible that this component can be either a secondary Rayleigh distribution with a larger width (higher velocities) during the emergence or a Gaussian component. The stronger the emergence, the more likely it is that the secondary component follows a Gaussian distribution, which can be related to the idea that strong emergences lead to radial outflows and, in that sense, to a one-dimensional flow distribution (only a v_r component exists, while normally the flow velocities are made up of a v_x and a v_y component). In order to support the statement about the necessity of a two-component distribution, where the second component is formed due to the strong changes in the flow pattern occurring during the formation of AR 11190, we analysed the evolution of a quiet Sun region during the same day. We found that for a quiet Sun flow-field distribution it is sufficient to use a single Rayleigh distribution to fit the speeds distribution (see Fig. A.2). It is also possible to observe the temporal evolution of the fitting parameters over 4 h (see Fig. A.3), and conclude that they do not show strong enhancements compared to their general behaviour.

Acknowledgements. This research received support by the Austrian Science Fund (FWF) P27800. Jose Iván Campos Rozo and Santiago Vargas Domínguez acknowledge funding from Universidad Nacional de Colombia research project code 36127: Magnetic field in the solar atmosphere. Additional funding was possible through an Odysseus grant of the Fund for Scientific Research-Flanders (FWO Vlaanderen), the IAP P7/08 CHARM (Belspo), and GOA-2015-014 (KU Leuven). This work has also received funding from the European Research Council (ERC) under the European Union's Horizon 2020 research and innovation programme (grant agreement No 724326). Jose Iván Campos Rozo is grateful to the National University, the Research Direction, and the National Astronomical Observatory of Colombia for providing him with a travel grant under the project for new professors and researchers to spend a part of his thesis time at KU Leuven enabling him to collaborate with Prof. T. Van Doorsselaere for this study. He also wishes to acknowledge the whole KU-Leuven University for the space and the academic support provided during his stay in Leuven. HMI/SDO data are courtesy of NASA/SDO and the AIA, EVE, and HMI science teams, and they were obtained from the Joint Science Operation Center (JSOC). Part of this research has been created by using SunPy libraries, an open-source and free community-developed solar data analysis package written in Python. We wish to express our gratitude to the editor of A&A, and the anonymous referee for his or her suggestions and comments about the present work, which improved the study considerably.

References

- Asensio Ramos, A., Requerey, I. S., & Vitas, N. 2017, *A&A*, **604**, A11
- Bushby, P. J., & Favier, B. 2014, *A&A*, **562**, A72
- Campos Rozo, J. I., & Vargas Domínguez, S. 2014, *Cent. Eur. J. Chem.*, **38**, 67
- Cheung, M. C. M., & DeRosa, M. L. 2012, *ApJ*, **757**, 147
- Dacie, S., Démoulin, P., van Driel-Gesztelyi, L., et al. 2016, *A&A*, **596**, A69
- de la Cruz Rodríguez, J., Hansteen, V., Bellot-Rubio, L., & Ortiz, A. 2015, *ApJ*, **810**, 145
- Domínguez Cerdeña, I. 2003, *A&A*, **412**, L65
- Golovko, A. A., & Salakhutdinova, I. I. 2015, *Astron. Rep.*, **59**, 776
- Guglielmino, S. L., Bellot Rubio, L. R., Zuccarello, F., et al. 2010, *ApJ*, **724**, 1083
- Hansen, C. J., Kawaler, S. D., & Trimble, V. 2004, *Stellar Interiors*, 2nd edn. (New York: Springer-Verlag), 241
- Hill, F., Gough, D., & Toomre, J. 1984, *Mem. Soc. Astron. It.*, **55**, 153
- Hoeksema, J. T., Liu, Y., Hayashi, K., et al. 2014, *Sol. Phys.*, **289**, 3483
- Hoffman, D., Karst, O. J., & Hoblit, F. M. 1975, *J. Ship Res.*, **19**, 172
- Hurlburt, N. E., Schrijver, C. J., Shine, R. A., & Title, A. M. 1995, in *Helioseismology, ESA SP*, 376, 239
- Ishikawa, R., & Tsuneta, S. 2011, *ApJ*, **735**, 74
- Kilcik, A., Yurchyshyn, V., Sahin, S., et al. 2018, *MNRAS*, **477**, 293
- Lisle, J., & Toomre, J. 2004, in SOHO 14 Helio- and Asteroseismology: Towards a Golden Future, ed. D. Danesy, *ESA SP*, **559**, 556
- Louis, R. E., Ravindra, B., Georgoulis, M. K., & Küker, M. 2015, *Sol. Phys.*, **290**, 1135
- Márquez, I., Sánchez Almeida, J., & Bonet, J. A. 2006, *ApJ*, **638**, 553

- Massaguer, J. M., & Zahn, J.-P. 1980, [A&A](#), **87**, 315
- Molowny-Horas, R. 1994, [Sol. Phys.](#), **154**, 29
- Musman, S. 1972, [Sol. Phys.](#), **26**, 290
- Namba, O., & van Rijsbergen, R. 1977, in Problems of Stellar Convection, eds. E. A. Spiegel, & J. P. Zahn (Berlin: Springer Verlag), [Lect. Notes Phys.](#), **71**, 119
- November, L. J. 1989, [ApJ](#), **344**, 494
- November, L. J., & Simon, G. W. 1988, [ApJ](#), **333**, 427
- November, L. J., Toomre, J., Gebbie, K. B., & Simon, G. W. 1981, [ApJ](#), **245**, L123
- November, L. J., Simon, G. W., Tarbell, T. D., & Title, A. M. 1986, [BAAS](#), **18**, 665
- November, L. J., Simon, G. W., Tarbell, T. D., Title, A. M., & Ferguson, S. H. 1987, in [NASA Conference Publication](#), eds. G. Athay, & D. S. Spicer, 2483
- Ortiz, A., Bellot Rubio, L. R., Hansteen, V. H., de la Cruz Rodríguez, J., & Rouppe van der Voort, L. 2014, [ApJ](#), **781**, 126
- Palacios, J., Blanco Rodríguez, J., Vargas Domínguez, S., et al. 2012, [A&A](#), **537**, A21
- Pesnell, W. D., Thompson, B. J., & Chamberlin, P. C. 2012, [Sol. Phys.](#), **275**, 3
- Potts, H. E., Barrett, R. K., & Diver, D. A. 2003, [Sol. Phys.](#), **217**, 69
- Rast, M. P. 2003, [ApJ](#), **597**, 1200
- Rezaei, R., Bello González, N., & Schlichenmaier, R. 2012, [A&A](#), **537**, A19
- Rieutord, M., & Rincon, F. 2010, [Sol. Phys.](#), **7**, 2
- Rösch, J. 1961, [Il Nuovo Cimento](#), **22**, 313
- Roudier, T., Rieutord, M., Malherbe, J. M., & Vigneau, J. 1999, [A&A](#), **349**, 301
- Roudier, T., Lignières, F., Rieutord, M., Brandt, P. N., & Malherbe, J. M. 2003, [A&A](#), **409**, 299
- Schuck, P. W. 2006, [ApJ](#), **646**, 1358
- Simon, G. W., Title, A. M., & Weiss, N. O. 1995, [ApJ](#), **442**, 886
- Simon, G. W., Title, A. M., Topka, K. P., et al. 1988, [ApJ](#), **327**, 964
- SunPy Community, Mumford, S. J., Christe, S., et al. 2015, [Comput. Sci. Discovery](#), **8**, 014009
- Thalmann, J. K., & Wiegelmann, T. 2008, [A&A](#), **484**, 495
- Title, A. M., Tarbell, T. D., Acton, L., Duncan, D., & Simon, G. W. 1986, [Adv. Space Res.](#), **6**, 253
- Title, A. M., Tarbell, T. D., Topka, K. P., et al. 1989, [ApJ](#), **336**, 475
- Ugarte-Urra, I., Upton, L., Warren, H. P., & Hathaway, D. H. 2015, [ApJ](#), **815**, 90
- Vargas Domínguez, S. 2009, PhD Thesis, University of La Laguna
- Vargas Domínguez, S., van Driel-Gesztelyi, L., & Bellot Rubio, L. R. 2012, [Sol. Phys.](#), **278**, 99
- Verma, M., Steffen, M., & Denker, C. 2013, [A&A](#), **555**, A136
- Verma, M., Denker, C., Balthasar, H., et al. 2016, [A&A](#), **596**, A3
- Welsch, B. T., Fisher, G. H., Abbott, W. P., & Regnier, S. 2004, [ApJ](#), **610**, 1148
- Ye, Y., Korsos, M. B., & Erdélyi, R. 2018, ArXiv e-prints [arXiv:1801.00430]
- Yi, Z., Darvann, T., & Molowny-Horas, R. 1992, [Software for Solar Image Processing – Proceedings from Last Mini Workshop](#), Tech. Rep.

Appendix A: Comparison with quiet Sun

To show the necessity of the combined speed distribution in active regions, we wish to replicate the analysis for a quiet Sun region within the period of our data set (from 16:00 UT to 20:00 UT on the same day)⁵. Figure A.1 shows on the left-hand side the full disc Sun on the day of observations, with the two analysed regions of interest marked by rectangles. The continuum maps and magnetograms of the two regions are shown in the right panels. Clearly the magnetic field activity is very high in the active region, while it is practically non-existent in the quiet Sun (as expected). We applied the LCT algorithm on the chosen quiet Sun region. The data comprise 320 images with the same cadence as described before and a total time of 4 h. The parameters for the LCT algorithm are the same as in the case for the active region. The principal first outcome can be seen in Fig. A.2.

Here we show the histograms of the speeds at three different times, which are independent and not related to the AR 11190 analysis. It becomes clear that a single Rayleigh distribution fits very well the whole histogram and it is not necessary, compared to the active region data, to fit the histogram with a more complex two-component distribution.

As this could be only a special case for three times, we also replicated Fig. 6 for the quiet Sun as shown in Fig. A.3. The evolution of the parameters shows no significant events (like strong parameter deviations), except for a few small occasional changes for the combination of Rayleigh distribution with a Gaussian component. Thus, again we can see that within the quiet Sun the expected result was realized, namely, the possibility to create a good single Rayleigh component fit. This is fully understandable as this principal distribution will be formed due to random x/y motions created from the turbulent convection.

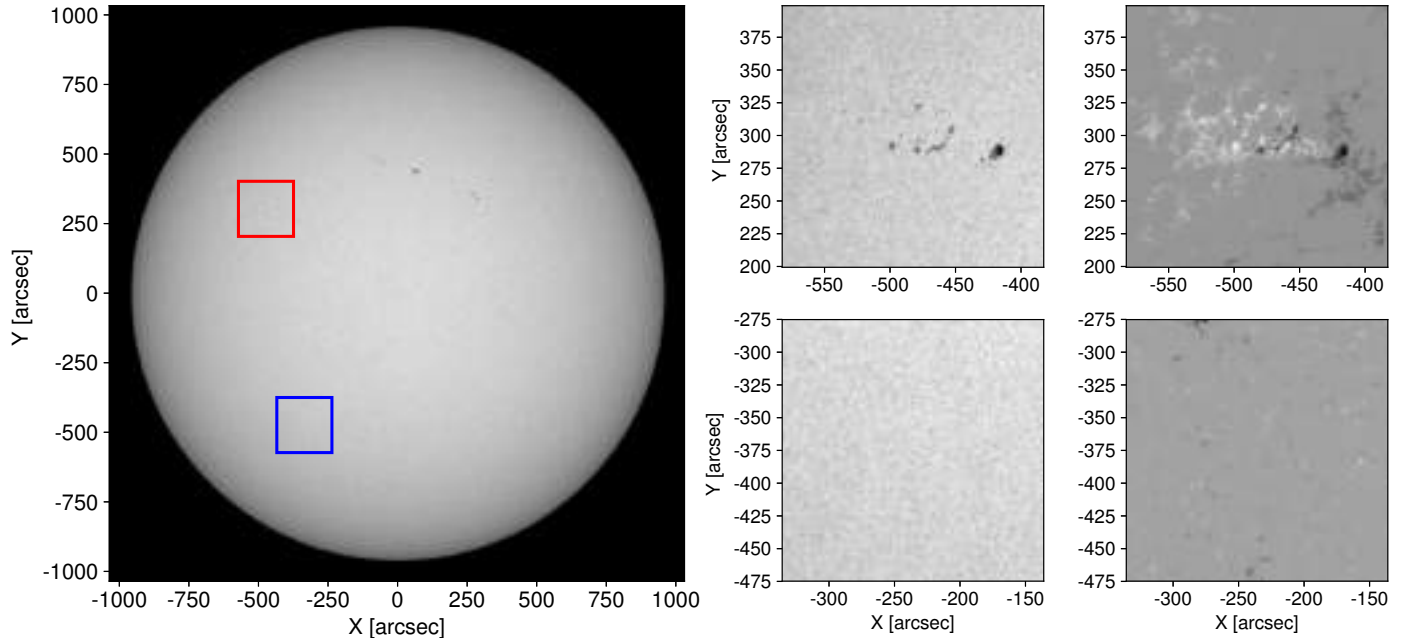


Fig. A.1. Overview of the analysed regions. *Left panel:* full disc Sun as seen by SDO/HMI on the day of observations. The two regions of interest are marked by a red square – active region NOAA 11190 – and blue square – quiet Sun region. *Right panel, top row from left to right:* a continuum map of the NOAA 11190 (red square) followed by the corresponding magnetogram is shown. *Bottom row:* same, but for the quiet Sun region. Time shown is April, 11 2011 at 17:45 UT.

⁵ An analysis of a plage region would complement this study perfectly, however, due to the considerable size of the current study and the necessary analysis, we postpone such an analysis to a future investigation.

Testcases for the proposed combination of two component distributions for plasma intensity data

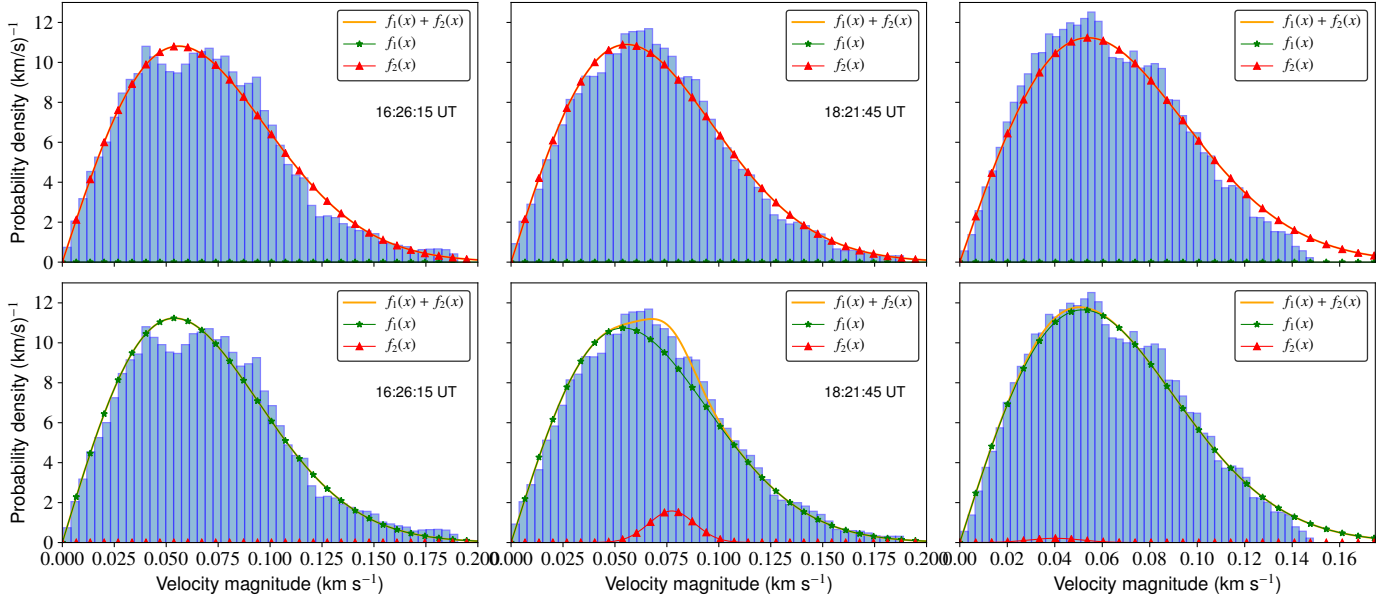


Fig. A.2. Similar to Fig. 5, but for the quiet Sun region as outlined in Fig. A.1 for three different test cases showing only the distributions obtained from the continuum maps. Thus the arrangement of the panels is as follows: *top row*: histograms of velocity as computed from the continuum maps for three different times applying a double Rayleigh component distribution fit, *bottom panels*: combination of Rayleigh and Gaussian distribution (all cases obtained from continuum maps).

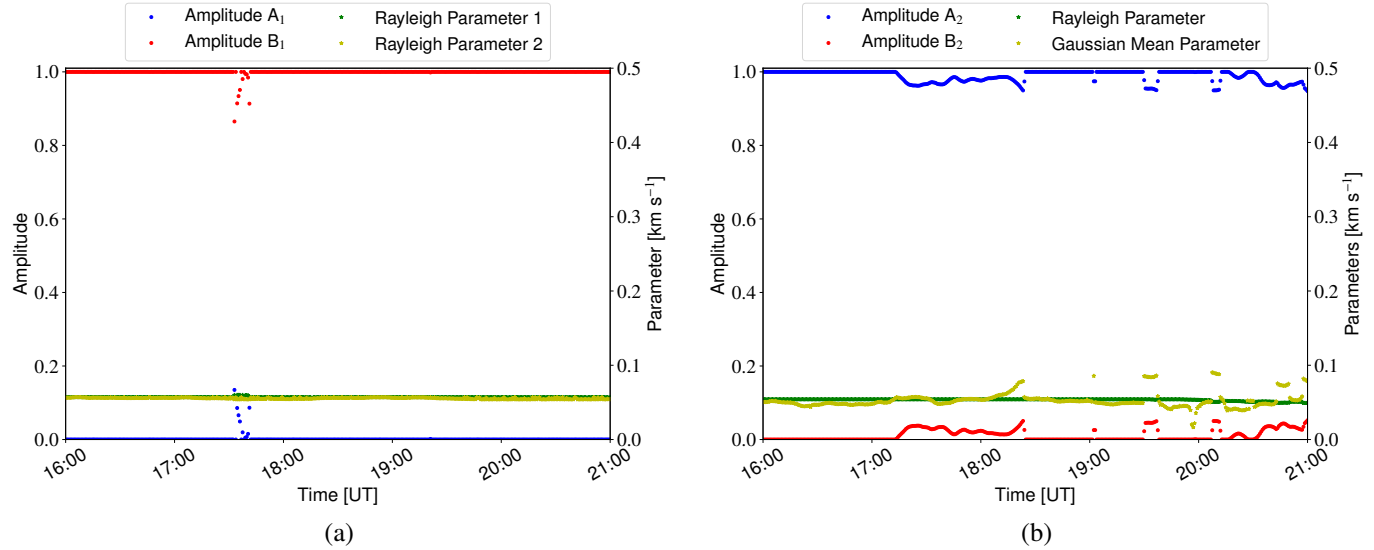


Fig. A.3. Similar to Fig. 6, but for the quiet Sun region as outlined in Fig. A.1 and only showing the continuum proper motion case (due to quiet Sun conditions, not enough moving magnetic elements are available to obtain velocity distributions).

Exploring magnetic field properties at the boundary of solar pores: A comparative study based on SDO-HMI observations

Jose Iván Campos Rozo^{1,2}, Dominik Utz^{1,3}, Santiago Vargas Domínguez², Astrid M. Veronig¹, and Arnold Hanslmeier¹

¹ IGAM, Institute of Physics, University of Graz, Universitätsplatz 5, 8010 Graz, Austria

² Universidad Nacional de Colombia, Observatorio Astronómico Nacional, Ed. 413 Bogotá, Colombia

³ Neuroimaging Science and Support Center-NISSL, Institute of Neurology, Kepler University Hospital, Wagner-Jauregg-Weg 15, 4020 Linz, Austria

The following article is published in ASTRONOMY & ASTROPHYSICS, Volume 674, article number A91, 9 pp. (2023). It is reproduced with the permission of EDP Sciences. The pdf document can be downloaded from the journal web page and it is embedded one-to-one in this thesis. My own contribution to this work was at least 60%.

Exploring magnetic field properties at the boundary of solar pores: A comparative study based on SDO-HMI observations*

J. I. Campos Rozo¹, S. Vargas Domínguez², D. Utz³, A. M. Veronig¹, and A. Hanslmeier¹

¹ IGAM, Institute of Physics, University of Graz, Universitätsplatz 5, 8010 Graz, Austria
e-mail: jose.campos-rozo@uni-graz.at

² Universidad Nacional de Colombia, Observatorio Astronómico Nacional, Teusaquillo, Bogotá, Colombia

³ Neuroimaging Science and Support Center-NISSL, Institute of Neurology, Kepler University Hospital, Wagner-Jauregg-Weg 15, 4020 Linz, Austria

Received 12 March 2023 / Accepted 19 April 2023

ABSTRACT

Context. The Sun's magnetic fields play an important role in various solar phenomena. Solar pores are regions of intensified magnetic field strength compared to the surrounding photospheric environment, and their study can help us better understand the properties and behaviour of magnetic fields in the Sun. In this work, we investigate the properties of magnetic fields on the boundaries of solar pores, specifically focusing on the evolution of the vertical magnetic field.

Aims. Up to now, there exists only a single study on magnetic field properties at the boundary region of a pore. Therefore, the main goal of this work is to increase the statistics of magnetic properties determining the pore boundary region. To this aim, we study the change of the vertical magnetic field on the boundaries of six solar pores and their time evolution.

Methods. We analyse six solar pores using data from the Helioseismic and Magnetic Imager instrument on board the Solar Dynamics Observatory. We apply image processing techniques to extract the relevant features of the solar pores and determine the boundary conditions of the magnetic fields. For each pore, the maximal vertical magnetic field is determined, and the obtained results are compared with the above-mentioned previous study.

Results. We find the maximal vertical magnetic field values on the boundaries of the studied solar pores to range from 1400 G to 1600 G, with a standard deviation between 7.8% and 14.8%. These values are lower than those reported in the mentioned preceding study. However, this can be explained by differences in spatial resolution as well as the type of data we used. For all the pores, we find that the magnetic inclination angle lies in a range of $30 \pm 7^\circ$, which is consistent with the idea that the magnetic field configuration in solar pores is mainly vertical.

Conclusions. The vertical magnetic field is an important factor in determining the boundary of solar pores, and it plays a more relevant role than the intensity gradient. The obtained information will be useful for future studies on the formation and evolution of magnetic structures of the Sun. Additionally, this study highlights the importance of high spatial resolution data for the purpose of accurately characterising the magnetic properties of solar pores. Overall, the findings of this work contribute to the understanding of the magnetic field properties of the Sun and will be crucial for improving models of solar dynamics and magnetic flux emergence.

Key words. Sun: magnetic fields – Sun: photosphere – sunspots

1. Introduction

During the past few years, the study of the Sun has experienced an incredible advancement with the launch of space-based telescopes and instruments, such as the Parker Solar Probe (Fox et al. 2016) and the Solar Orbiter (Müller et al. 2020) as well as the first light from the ground-based four-meter solar telescope the *Daniel K. Inouye* Solar Telescope (Rimmele et al. 2020), located on Haleakalā, Maui, Hawaii. The understanding of the (small-scale) dynamics of the Sun, the interaction of the plasma and the magnetic fields, and the processes leading to large-scale eruptions in the solar atmosphere require deeper study and understanding.

The emergence of magnetic flux from the solar interior causes the formation of various features that can be observed in the solar photosphere with different sizes, lifetimes, and magnetic field strengths (Cheung & Isobe 2014). The most distinguished magnetic features encountered over the solar surface are sunspots (see Solanki 2003, for a full overview regarding

sunspots), which can occur and form larger entities through the solar atmosphere called active regions. It is well known that sunspots are regions harbouring a very concentrated and organised magnetic field, reaching values from 1500 G to 3500 G (Sobotka 1999; Solanki 2003). Thus, the magnetic field is strong enough to freeze the plasma and is thus able to reduce the plasma dynamics and its apparent motions in the surrounding environment (e.g., Campos Rozo et al. 2019). The sunspot magnetic field features can be divided into two major parts, umbra and penumbra, which have different magnetic and thermodynamic properties (Borrero & Ichimoto 2011; Rezaei et al. 2012). Because of the strong intensity contrast differences, these two components of sunspots can be easily identified by visual inspection.

Mature sunspots are of predominant interest due to their involvement in complex magnetic field evolution and interaction with the upper atmospheric layers as well as being the sources of the most energetic solar eruptions, such as flares and coronal mass ejections (e.g., reviews by Green et al. 2018; Toriumi & Wang 2019). Solar pores, tiny sunspots lacking penumbrae, are worthy of attention since most of the time

* Movie associate to Fig. 1 is available at <https://www.aanda.org>

Table 1. Solar pores analysed in this work.

Pore number	Starting datetime	Ending datetime	# Hours
1	2011-07-10 06:59:11	2011-07-11 18:58:26	36
2	2013-08-23 23:59:07	2013-08-25 11:58:22	36
3	2014-06-02 05:59:09	2014-06-03 17:59:09	36
4	2015-01-18 17:58:54	2015-01-20 04:58:09	35
5	2015-05-22 11:59:08	2015-05-23 20:47:08	33
6	2018-05-12 05:59:09	2018-05-13 08:59:05	27

Notes. Time and positional ranges of the analysed solar pores in universal time (UT).

they constitute the first stage of a sunspot’s evolution. However, it is worth noting that not all solar pores evolve into sunspots.

It is possible that the evolution of some pores into sunspots may be attributed to the emergence of additional flux, which has the potential to alter the magnetic field topology around a pore. Such emergence events are often responsible for the creation and observation of moving magnetic features, which can be detected around certain pores prior to the formation of a penumbra. These moving magnetic features could provide a crucial link to the pre-existing magnetic topology and indicates the potential formation of filamentary substructures (Keppens & Martinez Pillet 1996; Leka & Skumanich 1998; Zuccarello et al. 2009; Sainz Dalda et al. 2012).

Pores mainly harbour a simple configuration of vertical magnetic fields and are therefore particularly suitable for studying the interaction and evolution of emerging magnetic fields with a convective pattern around them (Vargas Domínguez & Utz 2022). As a result of a convective collapse, whereby magnetic flux concentrations become too dense for convective motions to penetrate them, the trapped magnetic field can inhibit the emergence of new magnetic flux, forming the solar pores (Kitiashvili 2013). Many studies go deep into the analysis of the pore’s structure and dynamics while embedded in the granular pattern (e.g., Sobotka et al. 1999; Dorotovič et al. 2002; Vargas Domínguez et al. 2010; Ermolli et al. 2017, and references therein). Recently, Gilchrist-Millar et al. (2021) probed whether pores perform as magnetic waveguides, after detection of propagating magnetohydrodynamic wave activity above them. Solar pores have been the subject of numerous observational and theoretical investigations, yielding substantial advancements in our comprehension of these enigmatic features. Nonetheless, several questions related to their behaviour and characteristics persist. These include inquiries into the relationship between solar pores and sunspots, the evolution of magnetic fields in solar pores over time, the potential impact of solar pores on the upper solar atmospheric layers, and the contribution of solar pores to the overall solar activity cycle.

In this paper, we study the magnetic properties of a sample of isolated solar pores that do not evolve into sunspots using a space-based time series of photospheric filtergrams and magnetograms from the Helioseismic and Magnetic Imager (HMI; Hoeksema et al. 2014) on board the Solar Dynamics Observatory (SDO; Pesnell et al. 2012). In Sect. 2, we describe the data

and the processing used in this study. The analysis and results are presented in Sect. 3. Finally, we discuss our findings in the context of the magnetic properties of pores on their boundaries in Sect. 4.

2. Observational data and processing

The task of identifying isolated solar pores exhibiting substantial areas and robust lifetimes (exceeding 24 h) is a challenging task. To successfully execute this endeavour, we used photospheric observations obtained from a space-based telescope. We studied data from the HMI instrument on board SDO, which observes the full solar disk at 6173 Å with a pixel resolution of $\sim 0.504 \text{ arcsec pixel}^{-1}$. The instrument offers a diverse range of data products, including continuum intensity images captured at cadences of 45 s and 720 s (12 min), line-of-sight (LOS) magnetic field measurements acquired concurrently with the intensity maps, Milne-Eddington inversions deduced from the Stokes vector observations utilising the Very Fast Inversion of the Stokes Vector (Borrero et al. 2011) at a cadence of 12 min. The HMI data products can be accessed via the Joint Science Operations Center (JSOC) database¹.

For this study, we analysed six solar pores (see Table 1) that evolved over a period of about 36 hours. We selected solar pores that evolved when they were located close to the solar disk centre and chose an observation window when the distance of the pores from the central meridian was larger than 0.9 (as given by μ) in order to avoid projection effects during the analysis. Another condition for our six pores under study was that their calculated areas must be greater than $\sim 0.6 \text{ Mm}^2$ (5 pix^2) during the analysis time range. Moreover, another requirement was that they did not break up into smaller micropores and spread out over larger areas during this interval. A sample of the pores is displayed in Figs. 1 and 2 at time instances when their evolution was close to the maximum area during their lifetimes. All the six studied solar pores were tracked over a field of view of $30 \times 30 \text{ arcsec}^2$.

The HMI continuum maps were corrected applying the centre-to-limb variation algorithm² to account for the limb-darkening effect and also normalised over the mean intensity value of the surrounding quiet Sun (i.e., regions where the absolute value of the LOS magnetic field is less than 50 G). The threshold for the pore intensity boundary was defined in a manner similar to García-Rivas et al. (2021), varying the different levels for the intensity threshold in the range of 0.4–0.6 and identifying the best match to the solar pore boundary by visual inspection, which was determined as 55% of the intensity values of the normalised map (example of intensity contours are shown in Fig. 2 by the red solid contours).

In an effort to compute diverse magnetic parameters on the boundary of the solar pores, we utilised the HMI vector magnetogram products denoted as “hmi.B_720s”, available on the JSOC website. In particular, we used the azimuth, inclination, and strength of the total magnetic field vector. We resolved the ambiguity of the azimuth angle through the utilisation of the disambiguation angle maps integrated into the hmi.B_720s products. As the observations are gauged in the LOS reference system, it was imperative to re-project the azimuth and inclination magnetic angles to the local reference frame system via the r_frame_sphduo algorithm, a component of the AZAM software package. We subsequently calculated the vertical magnetic field component from the local reference frame inclination and

¹ <http://jsoc.stanford.edu/>

² See routine hazel.util.i0_allen in HAZEL2.

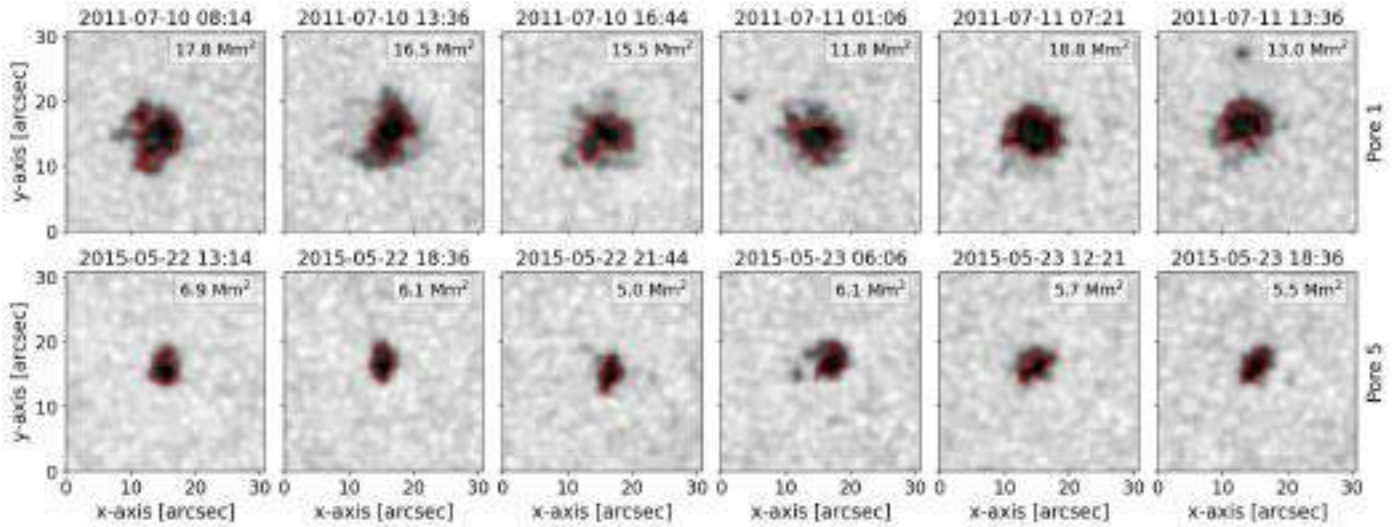


Fig. 1. Time evolution of two of the studied pores with the 55% intensity contours overplotted (red solid line). From left to right, snapshots during the pore's lifetime. The first row shows the evolution of pore 1, which revealed strong changes of the area. The second row shows pore 5, which revealed a quasi-stable area evolution. The accompanying movie shows the evolution of each of the six pores under study.

total field strength. It should be noted that pores 2 and 6 (see Fig. 3) exhibit negative polarity, and the values for the inclination magnetic angle correspond to $180^\circ - \gamma$, where γ represents the angle. Similarly, the vertical magnetic field was corrected by calculating the absolute values to the pores of negative polarity. Figure 3 depicts the magnetic parameters employed in the present analysis, with special emphasis on the vertical magnetic field (B_{ver}) in order to ascertain the critical threshold value at the boundaries of solar pores. All the calculations and algorithms used in the present work have been written (or adapted) in Python, and the specialised library for solar physics Sunpy³ (Mumford 2015).

3. Analysis and results

Various investigations have been conducted to establish the boundary demarcation between the umbra and penumbra (Jurčák et al. 2018; Schmassmann et al. 2018), as well as the interface between the photospheric plasma granulation and the border of solar pores (García-Rivas et al. 2021). Such studies have established threshold values of the vertical magnetic field to define the boundary of these features during their lifetime evolution. In the present work, we examine the evolution of the magnetic parameters, namely, inclination, total magnetic field, and vertical magnetic field, obtained from the boundaries of the studied pores as well as the areas enclosed by the boundary contours (see Fig. 4).

Figure 5 illustrates the temporal evolution of the analysed magnetic field parameters. These parameters were extracted and calculated as follows: First, the 55% threshold contour was derived for the intensity maps. That contour line was then plotted over the magnetic field parameters maps (see Fig. 3) to extract the quantities of interest along the boundary line of the pores. In a final step, the extracted values were then averaged. The time evolution of the magnetic parameters is displayed in Fig. 5. The evolution of the magnetic field inclination, which indicates an average of approximately 30° , is depicted by the green pattern in Fig. 5.

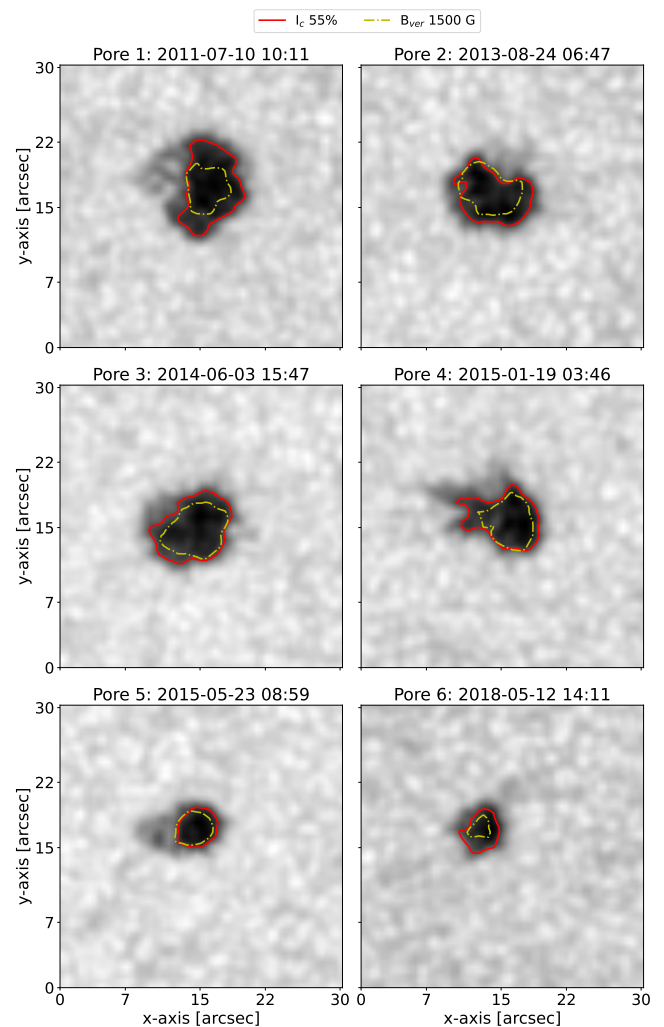


Fig. 2. HMI continuum maps of the six different solar pores studied that evolved with values of μ greater than 0.9. The red contours outline an intensity value of 55% I_c , and the yellow contours outline the level of the maximum vertical magnetic field B_{ver} found in the present work.

³ <https://sunpy.org/>

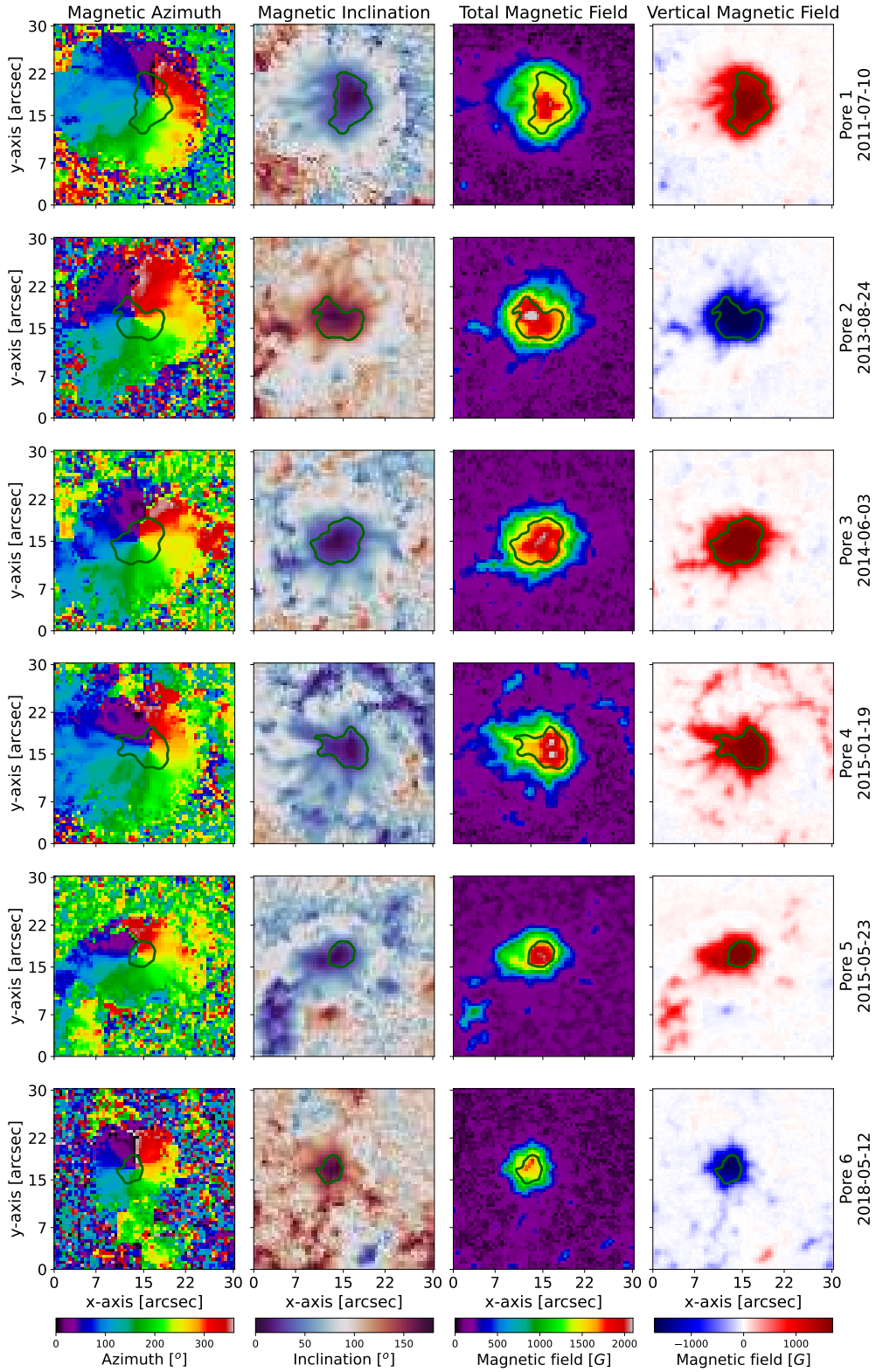


Fig. 3. Snapshot of each pore during the 36-h analysis interval. The contour in every panel outlines the pore intensity value corresponding to 55% of I_c , as in Fig. 2. From left to right: azimuth, inclination, total magnetic field strength, and vertical magnetic field.

A summary of the statistical values is presented in Table 2. The column labelled “Average over the whole data” displays the values computed over the entire period of the boundary evolution, whereas the column labelled “Maximal vertical field” indicates the values computed when the vertical

magnetic field values on the pore boundary attain the maximum value during the pore’s evolution. A description of the individual magnetic parameters analysed for the six studied solar pores is presented in the following subsections.

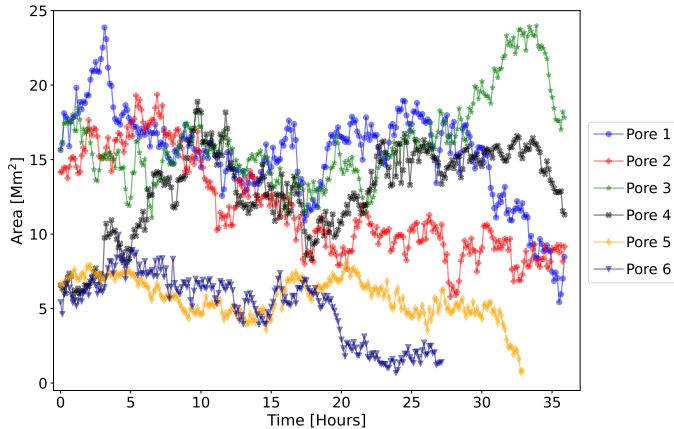


Fig. 4. Temporal evolution of the areas calculated from the enclosed region determined by the contours obtained from the continuum maps for the six pores under study (cf. red contours in Figs. 1 and 2).

3.1. Magnetic field inclination γ

It is well established in the scientific literature that the magnetic field in solar pores is predominantly vertical (e.g., Rucklidge et al. 1995; Sobotka 2002; Rempel et al. 2009; Jurčák 2011). This is also evidenced by the temporal evolution of the magnetic field inclination angle on the boundaries of solar pores, which varies on average in the range of 26–33°, as depicted in Fig. 5. By comparing the values in Table 2 and the areas of the pores in Fig. 4, we found that the larger the pores are, the higher is the mean inclination angle on their intensity boundaries. This is in agreement with the results obtained for sunspots (see Fig. 2 in Jurčák et al. 2018).

3.2. Total magnetic field strength B

For the six solar pores under study, we obtained that the values of the total magnetic field strength on the boundaries of the pores exhibit an average range of approximately 1400 G extending up to values greater than 1600 G, with a mean standard deviation of 10% during their evolution. Again, larger pores tend to have greater magnetic field strengths on their boundaries, which is consistent with the behaviour found for sunspots (see Fig. 2 in Jurčák et al. 2018). Figure 5 provides evidence that the time evolution of these values remains relatively constant over the pore's lifetime, indicating a certain level of stability for the magnetic field values on the boundaries of the solar pores. Moreover, at the times when the vertical magnetic field attains its maximum value, the strength of the total magnetic field in the studied solar pores reaches values greater than 1600 G, and the absolute maximum is approximately 1750 G. This value is still smaller than the maximum values of the vertical component of the magnetic field strength found during the stable phase of the evolution of the solar pore studied by García-Rivas et al. (2021; i.e., ~1920 G), who used the same intensity threshold but deconvolved HMI data. Also, Schmassmann et al. (2018) found a larger value of the total magnetic field strength on the umbral boundary of a stable sunspot: ~2170 G. They used the same HMI data product as we did but employed an intensity threshold of 50% of the quiet Sun intensity (whereas we used a 55% threshold). In this work, the magnetic field strength on the boundary of all the six pores during the stable phase of their evolution (when their areas did not change drastically) is thus weaker than what has been obtained in previous studies. Although the values are

not directly comparable, as we either used different datasets or different intensity thresholds than previous studies, we mention them as a reference to differentiate our results.

3.3. Vertical magnetic field strength B_{ver}

The vertical magnetic field vector, B_{ver} , shows a behaviour similar to the total magnetic field strength. On the boundary of a pore in a stable phase, García-Rivas et al. (2021) reported a maximum value of approximately 1730 G, while Schmassmann et al. (2018) reported a value of around 1630 G. We found significantly lower values for the vertical component of the magnetic field on the boundaries of the pores under study. The maximum values are around 1500 G, and the global maximum reached in pore 3 (see Table 2) is approximately 1570 G. However, as explained previously, one has to be cautious when comparing the values of our study with previous ones, as the methods, instruments, and data are slightly different. During the studied evolution periods of the pores, we found the mean value of the vertical component of the magnetic field to be between 1300 G and 1400 G. Similar to the evolution of the magnetic field strength, we did not observe significant variations of B_{ver} during the time periods studied.

Finally, Figs. 6 and 7 illustrate distinct correlations between the overall magnetic field strength, vertical field strength, magnetic field inclination, and the surface area of each pore over its lifespan. The red and blue colours correspond to two distinct time ranges defined by the moment when the vertical magnetic field reached its maximum value (indicated by the vertical dotted line in Fig. 5) during the pore's lifetime. The straight lines displayed in the figures represent separate linear fits that were applied to the data points in each of the two distinct phases.

Overall, all analysed pores demonstrate similar behaviour, although pores 4 and 5 exhibit greater dispersions. Figure 6 reveals that the magnetic field tends to be more vertical, with smaller inclination angles, during periods of maximum vertical magnetic field strength. In addition, Fig. 7 discloses the strong correlation between the magnetic inclination angle and the areas of the pores. In all cases, the maximum values of the vertical magnetic field strength are observed when the magnetic field inclination is close to either a global or local minimum and coupled with a global or local maximum of the magnetic field strength. This is not surprising, as the vertical magnetic field is directly correlated with these two parameters due to it is calculated as $B_{\text{ver}} = B \cdot \cos(\gamma)$.

4. Discussion and conclusions

All of the six stable pores selected for this study exhibit distinct physical properties. For instance, as shown in Fig. 4, there is significant potential for variation in the temporal evolution of the pore area. Even the smallest structures in the group, pores 5 and 6, persist for over 24 h before their areas decrease to values below the threshold of $\sim 5 \text{ pix}^2$ set as the minimum area. It is worth noting that pore 5 does not exhibit a substantial change in the areas, although it does have tiny fragmentations, as determined by the intensity threshold estimation, during the analysed time period, whereas other pores, such as pores 1 and 2, display significant alterations in their areas.

Despite the variability observed among the pores under study, they exhibit remarkably similar physical properties along their boundaries. Specifically, all pores examined in this study demonstrate a consistent behaviour in terms of the magnetic inclination angle evolution over the pore's lifetime, with an average value

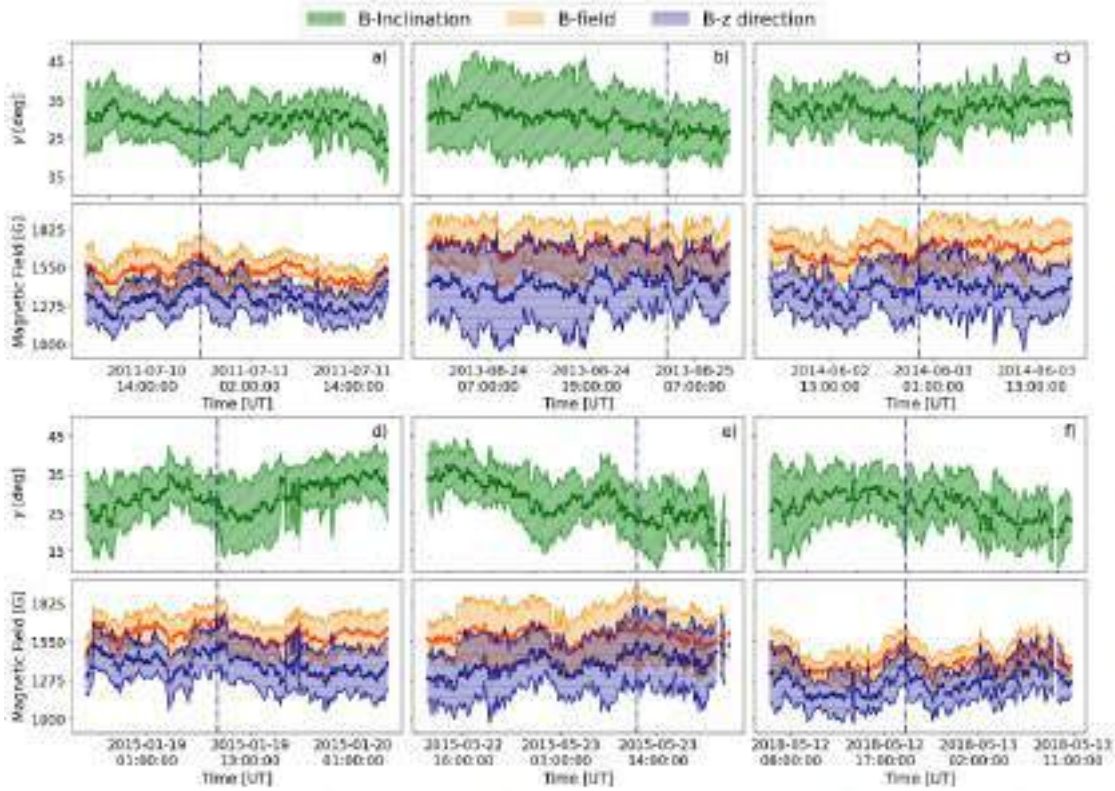


Fig. 5. Time evolution of the magnetic parameters obtained from the pore's boundary contours. The main, thicker line in each plot represents the mean value obtained from the contours over each respective magnetic parameter, whereas the corresponding shaded areas refer to the standard deviation also calculated from the contours. Figure displays the magnetic field inclination angle (green pattern), the total magnetic field strength (orange pattern), and the vertical magnetic field (blue pattern) for the six pores under study. The vertical dotted line in each panel denotes the time instant when the vertical magnetic field average over the boundary contour reached its maximum value.

of approximately 30° . This result is in agreement with the statistical analysis of pores by Keppens & Martinez Pillet (1996). However, we observe significantly stronger total and vertical magnetic field strengths of approximately 1560 G and 1345 G at the boundaries of the pores studied in this work, in comparison to the mean values reported by Keppens & Martinez Pillet (1996) of approximately 1400 G and 900 G, respectively. Nevertheless, the derived values for both the total and vertical magnetic field strengths are lower than those reported for stable sunspot and pore boundaries by Schmässmann et al. (2018) and García-Rivas et al. (2021), respectively.

We note that the solar pores analysed in this work primarily consist of isolated and stable cases with weaker and more dispersed magnetic fields compared to those embedded in active regions. Active regions, which include sunspots, exhibit concentrated magnetic fields that can produce intense flares and coronal mass ejections, ultimately affecting the configuration of the entire region. Isolated stable pores tend to persist for longer periods with relatively stable magnetic field configurations and little to no accompanying activity. In contrast, active region pores are typically associated with more intense forms of solar activity and impulsive energy releases, such as flares and coronal mass ejections, and their magnetic fields are typically more dynamic and complex. Therefore, considering their differences in magnetic field strength and behaviour, isolated stable pores and active region pores can be distinguished as distinct features of the solar atmosphere. Nonetheless, it is important to note that this study only considered rather isolated stable pores, and the analysis of complex active regions exhibiting pores would be an interesting study by itself, but it is beyond the scope of this paper.

Table 2. Magnetic parameter statistics.

Pore number	Magnetic parameter	Average over the whole data	Maximal vertical field
1	Inclination [$^\circ$]	29 ± 6	26 ± 8
	Total field [G]	1526 ± 105	1655 ± 125
	Vertical field [G]	1322 ± 133	1480 ± 150
	Inclination [$^\circ$]	30 ± 9	23 ± 5
2	Total field [G]	1610 ± 138	1665 ± 111
	Vertical field [G]	1386 ± 222	1524 ± 121
	Inclination [$^\circ$]	33 ± 6	25 ± 7
3	Total field [G]	1566 ± 130	1602 ± 73
	Vertical field [G]	1312 ± 163	1440 ± 112
	Inclination [$^\circ$]	30 ± 7	24 ± 9
4	Total field [G]	1613 ± 131	1746 ± 134
	Vertical field [G]	1390 ± 170	1573 ± 201
	Inclination [$^\circ$]	28 ± 7	21 ± 8
5	Total field [G]	1598 ± 202	1653 ± 210
	Vertical field [G]	1394 ± 216	1533 ± 226
	Inclination [$^\circ$]	27 ± 8	24 ± 10
6	Total field [G]	1425 ± 99	1589 ± 75
	Vertical field [G]	1258 ± 140	1425 ± 152

Notes. The columns display the mean values plus or minus the standard deviation calculated from the contours obtained on the boundary of the intensity images. The inclination values are given in degrees [$^\circ$], whereas the total and vertical field values are given in Gauss [G].

The main objective of this study was to increase the sample of the analysed boundary conditions of the magnetic field parameters in solar pores, focusing on the vertical magnetic field as the main

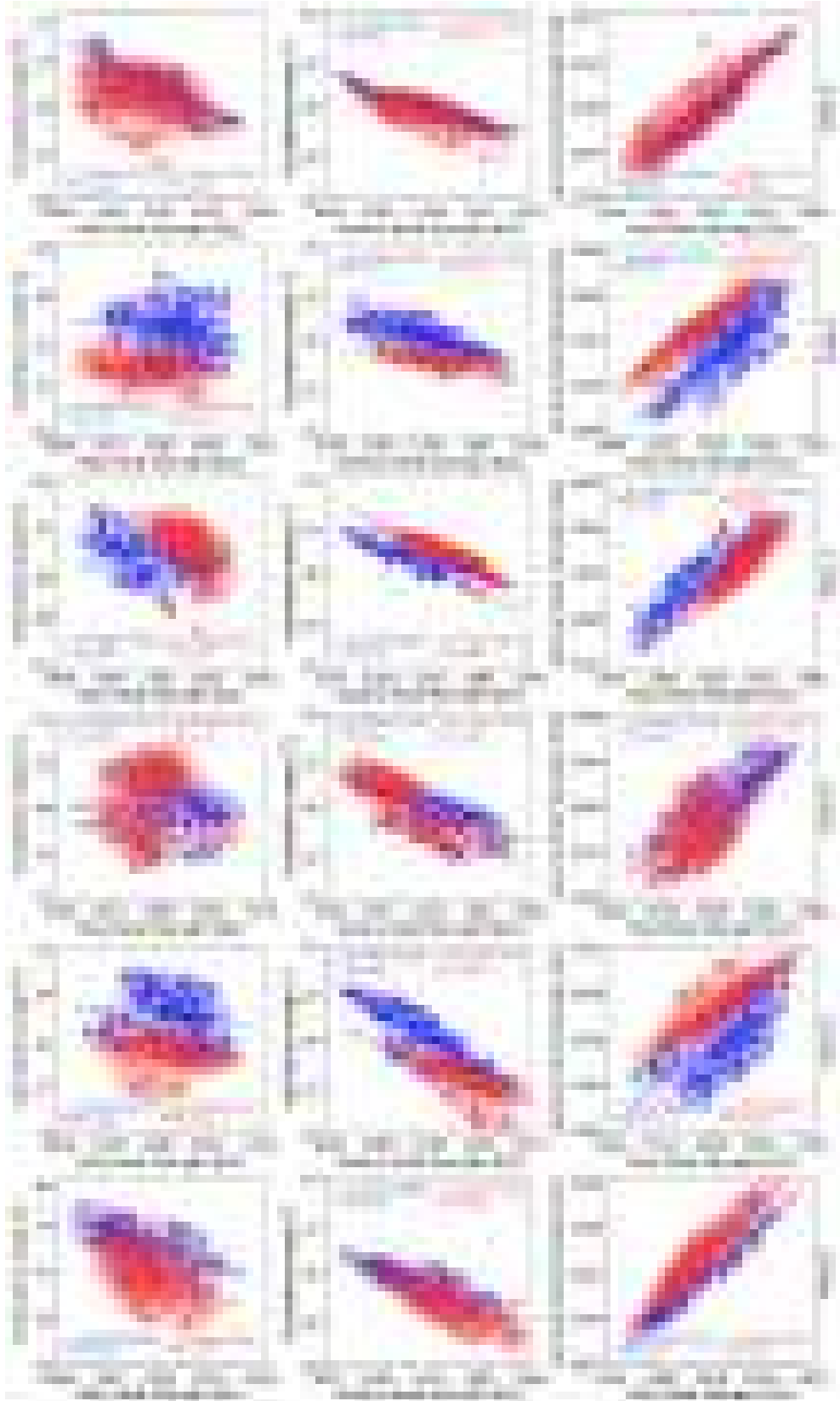


Fig. 6. Scatter plot displaying the correlation between magnetic parameters derived from the boundary of the studied pores. The red colour represents the correlation between parameters during the time period before the maximum vertical magnetic field is reached (see Fig. 5), while the blue colour represents the correlation for the time period after that instant. The shaded background contours depict the kernel density estimate plot of the correlation distribution. The insets give the parameters of the linear fit and the Pearson correlation coefficient separately for the two phases.

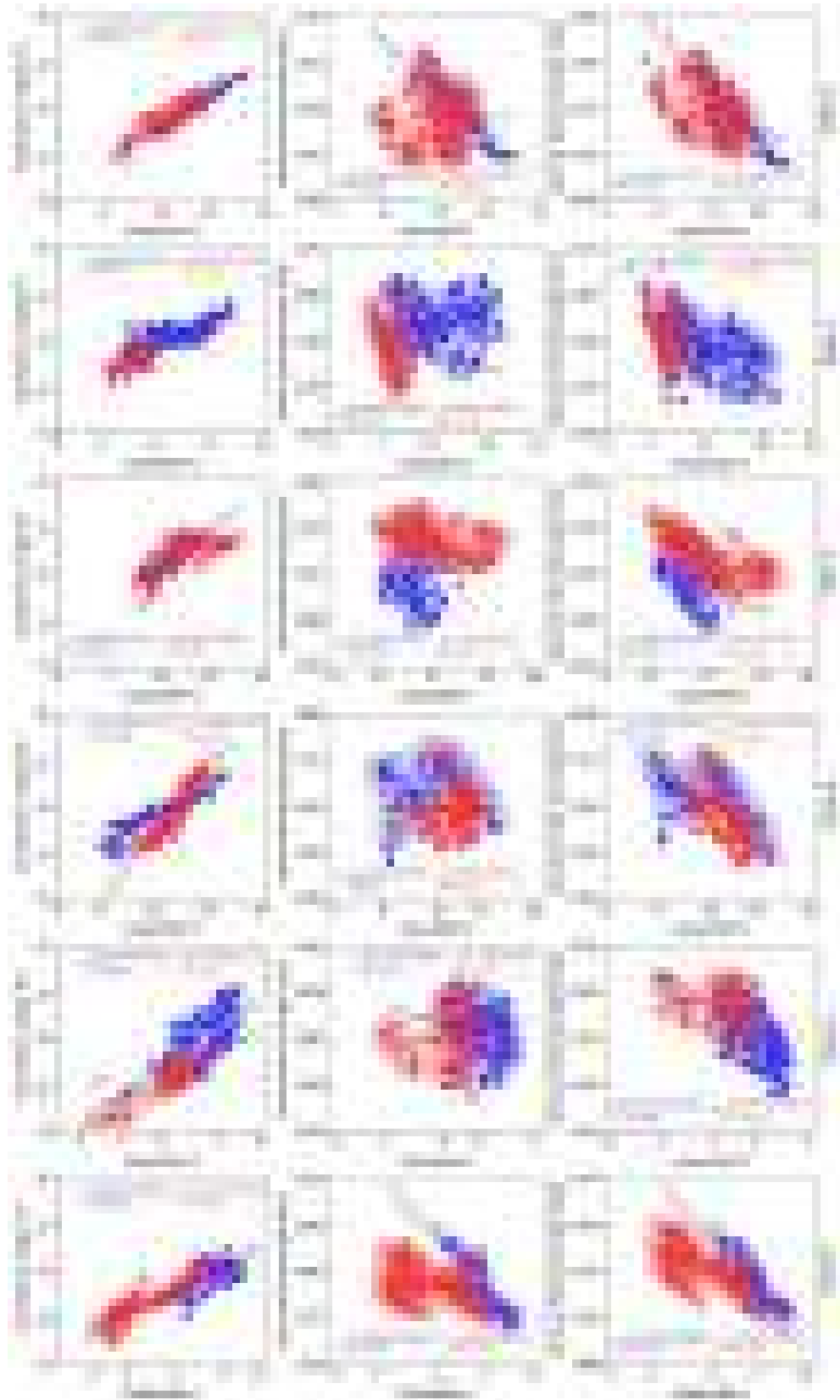


Fig. 7. Scatter plot displaying the correlation between the areas calculated inside the boundary contours (see Fig. 4) and each magnetic parameter derived at the boundary of the studied pores. The colours represent the same time periods described in Fig. 7. The shaded background contours depict the kernel density estimate plot of the correlation distribution. The insets give the parameters of the linear fit and the Pearson correlation coefficient separately for the two phases.

feature. The analyses of sunspots and pores (Schmassmann et al. 2018; Jurčák et al. 2018; García-Rivas et al. 2021) demonstrated the vital role of the vertical magnetic field component on the stability of these structures. The range of values of the maximum vertical magnetic field obtained in this study is between 1400 G and 1600 G, with standard deviations between 7.8% and 14.8%. These values are lower than those reported in previous studies, which may be due to the differences in the data type used as well as the different intensity threshold used.

The most critical calculation when determining the boundary values is defining the contours around the structures. The spatial resolution significantly affects the results, and high spatial resolution improves the accuracy of the values obtained. The results obtained in this study differ from those of García-Rivas et al. (2021), where the vertical magnetic field values exceed the values obtained in this study by more than 100 G. This difference could be attributed to the use of deconvolved data from SDO/HMI data (see Couvidat et al. 2016), which improves the spatial resolution of the data, and in that sense, the variation of the boundary changes considerably with respect of the original SDO/HMI maps. On the other hand, the maximum values of B_{ver} found in the sample of pores studied in this work also differ. Three of the six analysed pores have a maximum B_{ver} of around 1550 G (pores 2, 4, and 5), whereas the others reach lower maximum values (\sim 1448 G). From the temporal evolution of the pore areas defined by the 55% intensity threshold, it seems that only pore 5 is stable, while all the other pores undergo significant changes in their size with time. Pores 2, 4, and 5 also show the least variations in the vertical component of the magnetic field on their boundaries with time (see Fig. 5).

Figure 6 shows the correlation between the magnetic parameters during the two different time ranges over the lifetimes of the pores. As expected from how it is inferred, the vertical magnetic field is highly correlated with the inclination angle as well as the total strength of the magnetic field, whereby the correlation between the magnetic inclination angle and the total field shows a larger scatter. Figure 7 shows the correlation between the magnetic parameters and the areas obtained from the boundary contours. These plots reveal a high correlation between the evolution of the areas of the solar pores and the evolution of their magnetic inclination angles, as can be seen in the first column of Fig. 7.

Defining boundary values and conditions for specific observations can enhance the development of models and initial conditions for simulations that involve the evolution of magnetic field flux tubes, such as magnetic bright points, as shown in Magyar et al. (2021). This can provide critical inputs for comprehending the smaller scales of solar dynamics. Therefore,

exploring the magnetic field properties at the boundary of solar pores, as demonstrated in this comparative study, can contribute to a deeper understanding of their dynamics.

Acknowledgements. This research received support by the Austrian Science Fund (FWF) from the project number I 3955-N27. J. I. Campos Rozo and D. Utz acknowledge also the support from grant 21-16508J of the Grant Agency of the Czech Republic. All the datasets used in this work are courtesy of NASA/SDO, and they were obtained from the Joint Science Operation Center (JSOC).

References

- Borrero, J. M., & Ichimoto, K. 2011, *Liv. Rev. Sol. Phys.*, **8**, 4
- Borrero, J. M., Tomczyk, S., Kubo, M., et al. 2011, *Sol. Phys.*, **273**, 267
- Campos Rozo, J. I., Utz, D., Vargas Domínguez, S., Veronig, A., & Van Doorsselaere, T. 2019, *A&A*, **622**, A168
- Cheung, M. C. M., & Isobe, H. 2014, *Liv. Rev. Sol. Phys.*, **11**, 3
- Couvidat, S., Schou, J., Hoeksema, J. T., et al. 2016, *Sol. Phys.*, **291**, 1887
- Dorotovič, I., Sobotka, M., Brandt, P. N., & Simon, G. W. 2002, *A&A*, **387**, 665
- Ermolli, I., Cristaldi, A., Giorgi, F., et al. 2017, *A&A*, **600**, A102
- Fox, N. J., Velli, M. C., Bale, S. D., et al. 2016, *Space Sci. Rev.*, **204**, 7
- García-Rivas, M., Jurčák, J., & Bello González, N. 2021, *A&A*, **649**, A129
- Gilchrist-Millar, C. A., Jess, D. B., Grant, S. D. T., et al. 2021, *Phil. Trans. R. Soc. London Ser. A*, **379**, 20200172
- Green, L. M., Török, T., Vršnak, B., Manchester, W., & Veronig, A. 2018, *Space Sci. Rev.*, **214**, 46
- Hoeksema, J. T., Liu, Y., Hayashi, K., et al. 2014, *Sol. Phys.*, **289**, 3483
- Jurčák, J. 2011, *A&A*, **531**, A118
- Jurčák, J., Rezaei, R., González, N. B., Schlichenmaier, R., & Vomlel, J. 2018, *A&A*, **611**, L4
- Keppens, R., & Martínez Pillet, V. 1996, *A&A*, **316**, 229
- Kitiashvili, I. N. 2013, *IAU Symp.*, **294**, 269
- Leka, K. D., & Skumanich, A. 1998, *ApJ*, **507**, 454
- Magyar, N., Utz, D., Erdélyi, R., & Nakariakov, V. M. 2021, *ApJ*, **911**, 75
- Müller, D., St. Cyr, O. C., Zouganelis, I., et al. 2020, *A&A*, **642**, A1
- Pesnell, W. D., Thompson, B. J., & Chamberlin, P. C. 2012, *Sol. Phys.*, **275**, 3
- Rempel, M., Schüssler, M., Cameron, R. H., & Knölker, M. 2009, *Science*, **325**, 171
- Rezaei, R., Bello González, N., & Schlichenmaier, R. 2012, *A&A*, **537**, A19
- Rimmele, T. R., Warner, M., Keil, S. L., et al. 2020, *Sol. Phys.*, **295**, 172
- Rucklidge, A. M., Schmidt, H. U., & Weiss, N. O. 1995, *MNRAS*, **273**, 491
- Sainz Dalda, A., Vargas Domínguez, S., & Tarbell, T. D. 2012, *ApJ*, **746**, L13
- Schmassmann, M., Schlichenmaier, R., & Bello González, N. 2018, *A&A*, **620**, A104
- Sobotka, M. 1999, in Motions in the Solar Atmosphere, eds. A. Hanslmeier, & M. Messerotti, *Astrophys. Space Sci. Lib.*, **239**, 71
- Sobotka, M. 2002, in Solar Variability: From Core to Outer Frontiers, ed. A. Wilson, *ESA Spec. Publ.*, **1**, 381
- Sobotka, M., Vázquez, M., Bonet, J. A., Hanslmeier, A., & Hirzberger, J. 1999, *ApJ*, **511**, 436
- Solanki, S. K. 2003, *A&ARv*, **11**, 153
- Mumford, S. J. 2015, *Comput. Sci. Discov.*, **8**, 014009
- Toriumi, S., & Wang, H. 2019, *Liv. Rev. Sol. Phys.*, **16**, 3
- Vargas Domínguez, S., & Utz, D. 2022, *Rev. Mod. Plasma Phys.*, **6**, 33
- Vargas Domínguez, S., de Vicente, A., Bonet, J. A., & Martínez Pillet, V. 2010, *A&A*, **516**, A91
- Zuccarello, F., Romano, P., Guglielmino, S. L., et al. 2009, *A&A*, **500**, L5

Observational evidence for two-component distributions describing solar magnetic bright points

Gerardine Berrios Saavedra¹, Dominik Utz^{2,3,4}, Santiago Vargas Domínguez⁵, Jose Iván Campos Rozo⁶, Sergio Javier González Manrique^{7,8,9}, Peter Gomořý⁹, Christoph Kuckein^{7,8,10}, Horst Balthasar¹⁰, and Peter Zelina⁹

¹ Universidad Nacional de Colombia, Bogotá, Colombia

² Institute of Physics, Faculty of Science, University of South Bohemia, České Budějovice, Czech Republic

³ Computational Neurosciences, Neuromed Campus, Kepler University Hospital, Linz, Austria

⁴ Instituto de Astrofísica de Andalucía IAA-CSIC, Granada, Spain

⁵ Universidad Nacional de Colombia, Observatorio Astronómico Nacional, Bogotá, Colombia

⁶ University of Graz, Graz, Austria

⁷ Instituto de Astrofísica de Canarias, Tenerife, Spain

⁸ Departamento de Astrofísica, Universidad de La Laguna, La Laguna, Tenerife, Spain

⁹ Astronomical Institute, Slovak Academy of Sciences, Tatranská Lomnica, Slovakia

¹⁰ Leibniz – Institute for Astrophysics Potsdam, Potsdam, Germany

The following article is published in ASTRONOMY & ASTROPHYSICS, Volume 657, article number A79, 12 pp. (2022). It is reproduced with the permission of EDP Sciences. The pdf document can be downloaded from the journal web page and it is embedded one-to-one in this thesis. My own contribution to this work was at least 25%.

Observational evidence for two-component distributions describing solar magnetic bright points

Gerardine Berrios Saavedra¹, Dominik Utz^{2,3,4}, Santiago Vargas Domínguez⁵, José Iván Campos Rozo⁶, Sergio Javier González Manrique^{7,8,9}, Peter Gömöry⁹, Christoph Kuckein^{7,8,10}, Horst Balthasar¹⁰, and Peter Zelina⁹

¹ Universidad Nacional de Colombia, Bogotá, Colombia

e-mail: yberrioss@unal.edu.co

² Institute of Physics, Faculty of Science, University of South Bohemia, České Budějovice, Czech Republic

³ Computational Neurosciences, Neuromed Campus, Kepler University Hospital, Linz, Austria

e-mail: dominik.utz@kepleruniklinikum.at

⁴ Instituto de Astrofísica de Andalucía IAA-CSIC, Granada, Spain

⁵ Universidad Nacional de Colombia, Observatorio Astronómico Nacional, Bogotá, Colombia

e-mail: svargasd@unal.edu.co

⁶ University of Graz, Graz, Austria

⁷ Instituto de Astrofísica de Canarias, Tenerife, Spain

⁸ Departamento de Astrofísica, Universidad de La Laguna, La Laguna, Tenerife, Spain

⁹ Astronomical Institute, Slovak Academy of Sciences, Tatranská Lomnica, Slovakia

¹⁰ Leibniz – Institute for Astrophysics Potsdam, Potsdam, Germany

Received 30 April 2021 / Accepted 30 September 2021

ABSTRACT

Context. High-resolution observations of the solar photosphere reveal the presence of fine structures, in particular the so-called Magnetic Bright Points (MBPs), which are small-scale features associated with strong magnetic field regions of the order of kilogauss (kG). It is especially relevant to study these magnetic elements, which are extensively detected in all moments during the solar cycle, in order to establish their contribution to the behavior of the solar atmosphere, and ultimately a plausible role within the coronal heating problem.

Aims. Characterisation of size and velocity distributions of MBPs in the solar photosphere in two different datasets of quiet Sun images acquired with high-resolution solar instruments i.e. Solar Optical Telescope SOT/Hinode and the High-resolution Fast Imager HiFI/GREGOR, in the G -band (4308 \AA).

Methods. In order to detect the MBPs, an automatic segmentation and identification algorithm is used. Next, the identified features were tracked to measure their proper motions. Finally, a statistical analysis of hundreds of MBPs is carried out, generating histograms for areas, diameters and horizontal velocities.

Results. This work establishes that areas and diameters of MBPs display log-normal distributions that are well-fitted by two different components, whereas the velocity vector components follow Gaussians and the vector magnitude a Rayleigh distribution revealing again for all vector elements a two component composition.

Conclusions. The results can be interpreted as due to the presence of two different populations of MBPs in the solar photosphere one likely related to stronger network magnetic flux elements and the other one to weaker intranetwork flux elements. In particular this work concludes on the effect of the different spatial resolution of GREGOR and Hinode telescopes, affecting detections and average values.

Key words. Sun: photosphere – Sun: evolution – methods: observational

1. Introduction

High-resolution observations of the solar photosphere reveal a plethora of exceedingly fine structures, mainly corresponding to Magnetic Bright Points (MBPs), which are small-scale features associated with strong magnetic field regions of the order of up to kilogauss (1.5 kG; Nisenson et al. 2003; Beck et al. 2007; Ishikawa et al. 2007; Utz et al. 2013; Keys et al. 2019). MBPs are found all over the photosphere, in both quiet and active regions of the Sun, in particular located in the intergranular lanes in between granular convective cells (e.g., Muller et al. 1989). Several investigations have found the mean diameter of a MBP in a range of 100–300 km, its horizontal average

velocity between 0.2 and 5 km s^{-1} and average lifetimes of 2.5–10 min, as shown by the results of Sánchez Almeida et al. (2004), Beck et al. (2007), Utz et al. (2010), Liu et al. (2018), among others.

According to Sánchez Almeida et al. (2004), the presence of MBPs in the solar photosphere was first reported by Dunn & Zirker (1973). Since then, MBPs have been extensively, but still not fully, investigated from the various viewpoints of theory (e.g., Spruit 1979; Parker 1978; Deinzer et al. 1984), observations (exemplarily: Berger et al. 2007; Viticchié et al. 2009), and simulations (Danilovic et al. 2010; Riethmüller et al. 2014). Among the better covered aspects of MBPs are their general characteristics as well as their formation which is believed

to be due to the convective collapse theory introduced by [Spruit \(1979\)](#) as well as [Parker \(1978\)](#) and shown impressively in observations by [Nagata et al. \(2008\)](#) in a case study and on statistical grounds by [Fischer et al. \(2009\)](#). Other authors also tried to identify the formation of MBPs in numerical simulations and compared them with observations, e.g., [Danilovic et al. \(2010\)](#). Another hot topic is MBP and MHD waves as these waves can contribute to the solar atmospheric heating (see, e.g., [Jess et al. 2009](#); [Vigeesh et al. 2009](#); [Fedun et al. 2011](#)). Aspects similarly important but less extensively covered are the long-time evolution of MBP pattern with the solar cycle and their relationship to a possible surface dynamo and/or global dynamo (e.g., [Utz et al. 2016, 2017](#)), or the relationship of MBPs and the formation of solar spicules (e.g., [Samanta et al. 2019](#)) showed that magnetic flux cancellation between intranetwork fields and network fields represented by MBPs leads to the formation of spicules.

MBPs can exist as isolated features as well as form groups as reported by [Nisenson et al. \(2003\)](#) and [Berger & Title \(1996\)](#). Their dynamics can be seen as highly influenced by the surrounding granulation pattern and they themselves are being pushed by granules giving rise to a more or less chaotic movement pattern (e.g., [Muller 1983](#); [Stanislavsky & Weron 2009](#)). [Nisenson et al. \(2003\)](#) and [Berger & Title \(1996\)](#) also found that two MBPs can come together and form only one (coalescence), or one can divide into two smaller MBPs (fragmentation). In particular [Berger & Title \(1996\)](#) analysed images in the *G*-band and in the continuum, acquired with the Swedish Vacuum Solar Telescope (SVTS; [Scharmer et al. 1985](#)) at the Observatorio Roque de los Muchachos in La Palma, Canary Islands, Spain, finding rapid fragmentation and coalescence in a sample of MBPs under analysis.

MBPs correspond to thin tubes of magnetic flux as explained by [Steiner et al. \(2001\)](#), which are widening in diameter going from the photosphere to upper heights. When these magnetic elements are observed in high-resolution filtergrams of the solar photosphere, they look brighter than their surroundings ([Zakharov et al. 2005](#)). This is due to the higher magnetic field concentration inside the flux tube generating a strong magnetic pressure and, in order to maintain the equilibrium, the gas pressure inside the tube needs to be reduced. This chain of causal effects leads ultimately to lower densities inside the flux tube (see [Schüssler et al. 2003](#)). The dynamic process to reach the equilibrium is called convective collapse and more details can be found in the works of [Spruit \(1979\)](#), [Parker \(1978\)](#). Due to the lower density, also the opacity decreases giving rise to a higher contribution of emission of radiation from deeper layers and thus increasing the overall brightness of the MBP structure. Added to this, the hot walls of the flux tube can also contribute with an excess of radiation, especially when viewed off the disk centre (for more details see [Steiner et al. 2001](#)).

The study of these magnetic elements is considered relevant to establish their plausible contribution to the behavior of the solar atmosphere, and ultimately to the well-known coronal heating problem (among many others, e.g., [Klimchuk 2006](#); [Erdélyi & Ballai 2007](#)). As [Choudhuri et al. \(1993\)](#) explained, although being small, MBPs could significantly contribute to the energy budget in the corona as they harbour strong magnetic fields, and are spread over the entire surface of the Sun. Theoretically, the movement of the footpoint of a MBP could generate a flow of energy that ascends to the corona and can contribute to its heating (e.g., via the generation of Alfvén waves; [Jess et al. 2009](#); [Mathioudakis et al. 2013](#)). Observations of MBPs can also be acquired in other wavelengths. According to [Nisenson et al. \(2003\)](#), MBPs and the filigree (chains of

bright features located over the intergranular lanes) are observed in lines of the solar spectrum such as H α , Ca II H and K; i.e. lines formed in the chromosphere. Furthermore, the Na I D₁ and D₂ lines can also be used to identify MBPs, as well as the photospheric Si I 10 827 Å and Ca I 10 839 Å lines ([Jess et al. 2010](#); [Kuckein 2019](#)). [Wiehr & Bovelet \(2009\)](#) found a preferred location of these structures (that they called magnetic inter-granular structures) at the footpoints of dark H α fibrils, which are known to delineate the network boundaries.

In this work, the analysis of MBPs is done by means of time series of images of the solar photosphere acquired with high-resolution ground-based and space-borne solar telescopes, i.e. with the Solar Optical Telescope instrument (SOT; [Tsuneta et al. 2008](#)) of the Hinode mission (see [Kosugi et al. 2007](#)) on the one hand and the High-resolution Fast Imager (HiFI; [Kuckein et al. 2017](#)) placed at GREGOR, instrument observing in the *G*-band (4308 Å) on the other hand.

We focus on the detection of MBPs by means of an automatic segmentation and identification algorithm described in [Utz et al. \(2014\)](#), to further track their evolution in order to characterise their dynamics and some of their physical parameters. Section 2 describes the data sets and the algorithm used. In Sect. 3 we give the results of the analysis, in Sect. 4 we discuss the influence of intensity cut-offs and spatial resolution and in Sect. 5 we refer to the principal discussion. Finally, the main conclusions are presented in Sect. 6.

2. Observational data and methodology

This study makes use of data sets taken on two different days with two different telescopes. The Hinode set (henceforth dataset-H) consists of 332 images acquired with the Hinode satellite, specifically with the Solar Optical Telescope (SOT; [Tsuneta et al. 2008](#)). These data correspond to solar observations acquired on March 10, 2007, spanning from 7:00 to 9:59 UT. The temporal resolution is 30 s with a spatial sampling resolution of 0''.108 per pixel. The Field-of-View (FOV) is 55''.8 × 111''.6 (see bottom-left panel in Fig. 1). These observations are not affected by the adverse effects of the atmospheric seeing. On the other hand, the GREGOR telescope ([Schmidt et al. 2012](#); [Kleint et al. 2020](#)) dataset (henceforth dataset-G) consists of 769 images acquired on July 13, 2019 with the HiFI instrument and spanning from 7:38 to 08:48 UT. These data are characterised by presenting a temporal resolution of 5 s, a pixel size of 0''.0286 per pixel and a FOV of 32''.4 × 26''.0 (see top-left panel in Fig. 1). Despite these observations being affected by atmospheric seeing, corrections made with the adaptive optics system ([Berkefeld et al. 2012](#)) considerably improved the image quality. Figure 1 (left panels) shows the corresponding FOV (in *G*-band images) for dataset-G and dataset-H, as labeled.

The first step, before applying the analysis algorithms, is to focus on the data reduction. Dataset-H is acquired in zero level of calibration from the freely accessible Hinode data base. The calibration is performed with the SolarSoft routine *fg_prep* implemented in the Interactive Data Language (IDL); the routine executes a general reduction of intrinsic errors including flat field, dark current and bad pixels. Dataset-G is calibrated using the data reduction pipeline *sTools* ([Kuckein et al. 2017](#)), which includes dark-current and flat-field corrections, as well as image selection. Then, speckle interferometry ([Wöger & von der Lühe 2008](#)) is used to produce level-2 data, which further corrects aberrations caused by the atmosphere as explained by [Kuckein et al. \(2017\)](#).

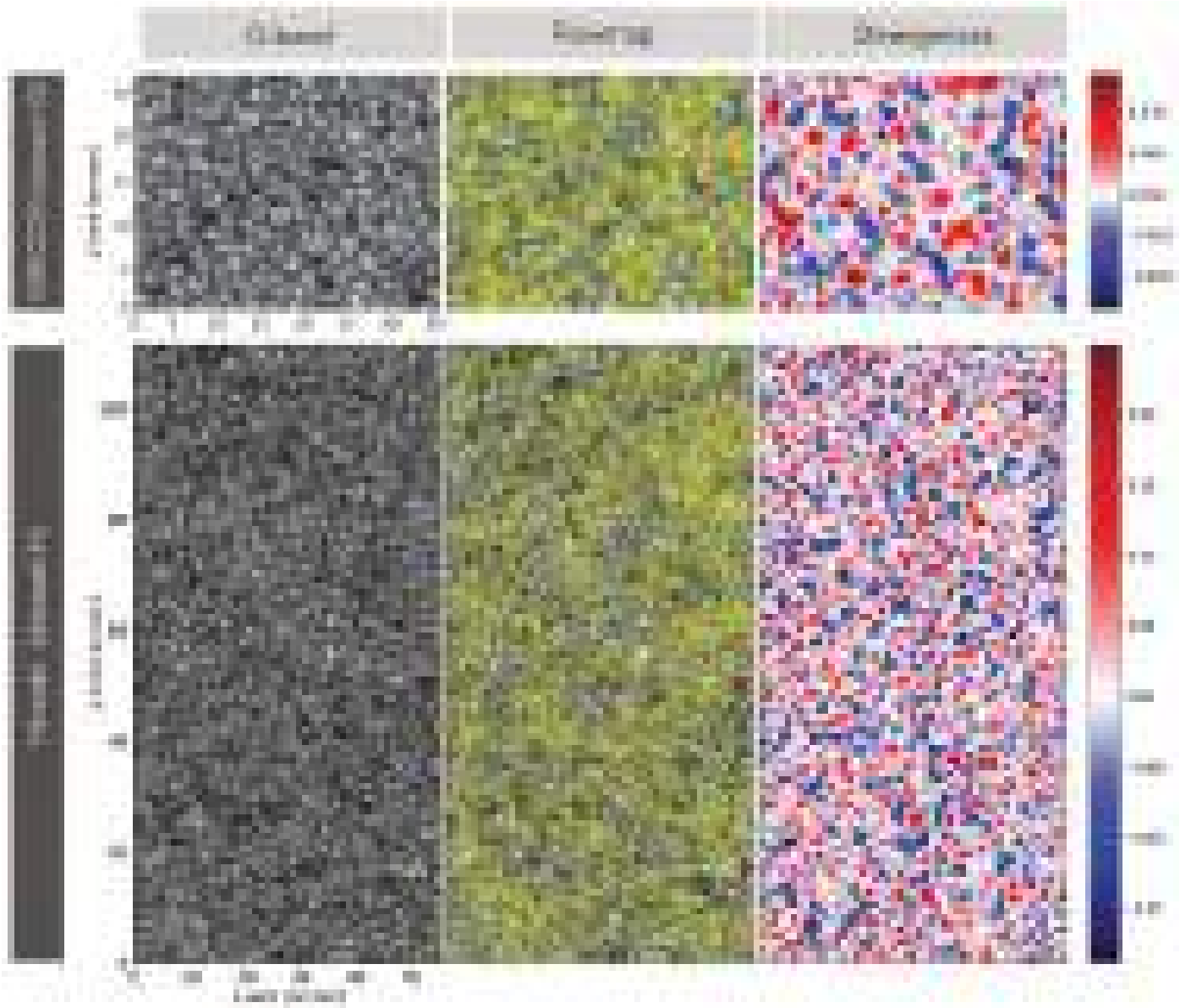


Fig. 1. G-band images, map of velocities, and map of divergences (*from left to right*) for dataset-G (top panels) and dataset-H (bottom panels). The red/black crosses mark the MBPs identified in the FOV. Note that the spatial scales are different for each data set.

Finally, the two data sets are corrected from intensity disparities. When one evaluates the intensity level of the images organised in a data cube, it is found that each image can vary slightly in the dynamic range of intensities as well as its central intensity. Therefore, it is necessary to perform an intensity recalibration process that consists of modifying the dynamic range¹ of the images in such a way that the range keeps the same for all images. In the same way, the average intensity of all the images should be put at the same value. In this way it is guaranteed that all the images have a constant intensity range. Figure 2 illustrates this process in more detail. The figure depicts two intensity histograms in continuous blue and red lines for image 1 and 2, respectively, before the process of intensity recalibration; it can be seen that both the dynamic range and the mean intensity are different. The intensity histograms in dashed-dotted style depict the recalculated histograms after the normalisation process was

applied for each image, respectively. It can be evidenced that both, the dynamic range and mean intensity for the two images, are statistically similar now as expected for images of the quiet Sun.

After the pre-processing is completed, the identification of MBPs is made with an automatic algorithm of detection based on the following steps: firstly, each image is segmented in the following way by multiple-thresholding. In a first step the brightest pixel of the image is detected and initializes the first segment. In the next step an intensity threshold slightly lower to the intensity level of the brightest pixel is applied and the newly found pixels which border the existing segment are added to the existing segment. Those pixels which are left (do not border the existing segment) initialize new segments. After that, the same process is repeated with the succeeding lower intensity threshold. Thus by going through the whole image intensity range from the brightest to the darkest pixel the image is broken up into image segments (practically local intensity maxima initialize segments which grow in size until they reach the boundary

¹ Defined here as the difference between the highest percentile of intensity values compared to the lowest percentile.

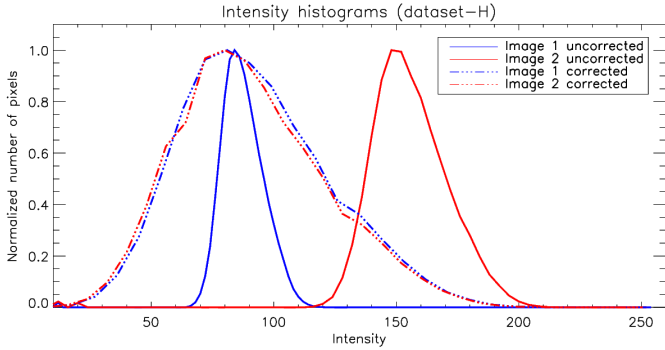


Fig. 2. Intensity histograms from two images, before (continuous lines) and after (dashed-dotted lines) the intensity recalibration process is applied.

of other segments). Subsequently, MBPs in each created segment are detected based on the brightness gradient.

Once the MBPs have been identified (in the case of GREGOR about 110 MBPs per image and about 170 for Hinode; yielding a total number of detected MBP instances of 87 000 for GREGOR, and 56 000 for Hinode, respectively) their size in pixels is calculated; areas in km^2 are determined and subsequently their diameters in km calculated, assuming that the MBP features have a circular shape, which is considered a good approximation for the purposes of this analysis comparing relative sizes of MBPs when detected by different instruments². Histograms for area and diameter are presented and commented in detail in Sect. 3. Furthermore, the brightness barycenters of each MBP are calculated.

Finally, these tiny elements are tracked in a sequence of images with the purpose of determining their dynamic and evolutionary characteristics. This procedure consists in comparing the intensity barycentre position of one MBP in an image with all the found barycentre MBP positions in the next time instance. If the distance between two positions is less than or equal to one pre-established maximum distance, then the two individual detections of MBPs belong to the same MBP time sequence³. The maximum distance parameter can be found by the following two considerations: (i) the allowed distance must be high enough to allow for the highest possible velocities which can be estimated by, e.g., taking 3.5 times the previously established larger MBP velocities of about 4 km s^{-1} (e.g., in the work of Nisenson et al. 2003, one can see a velocity tail starting roughly with 4 km s^{-1} extending up to $(6\text{--}8) \text{ km s}^{-1}$); and ii) by being small enough so that one would not connect a non-involved MBP into the time series. This can be estimated by keeping the maximum distance smaller than an average MBP diameter (about 70 km). Both considerations together speak for a search distance of about 70 km or with a time cadence of 5 s, translating to the maximum detectable velocities of about 14 km s^{-1} . By applying these processing steps to all the images and detected MBPs we

² As Feng et al. (2013) showed, assuming an elliptical shape would be more precise as the modal value of the ratio between the major and minor axis of an equisized ellipse would be around 1.5. However, for comparison purposes we follow the tradition of assuming a round or circular shape and stating diameters for equisized circles as well as the raw results in the form of a size distribution.

³ Due to this definition it is explicitly allowed for MBPs that one temporal realization of an MBP can have several follow-up MBP realizations, i.e. splitting is allowed and can be detected. The estimation of such splitting and merging events as well as the rates of occurrence of such events will be an interesting topic of a future work.

obtain the time sequences and evolution of all the MBPs. In order to calculate MBP velocities, barycentre displacements between MBPs identified by the algorithm in subsequent frames are utilized. This leads finally to the estimation of their velocities and their statistical velocity distributions.

3. Distribution of sizes and velocities of MBPs

In order to characterise the dynamics of the MBPs in the photosphere in quiet Sun regions, this section deals with the analysis of areas, diameters and velocities, in particular for dataset-G as it represents the highest-resolution data used in this work. The actual sizes of the MBPs are calculated by applying either a 50% or 80% cut-off level on each of the segments identified to be a MBP (for more details refer to Sect. 5), the final histograms of the distribution of areas and diameters are illustrated in Fig. 3. Here we used a binning of the original size in pixels of 1 and then recalculated the corresponding size in km^2 , as well as the diameter in km. As this transformation is a non-linear process (via the square root function) the binning looks quenched to larger diameters in this representation. The red curves in the figure represent the log-normal fits for every distribution, and the curves in green correspond to two underlying different components that constitute the distributions in red and each of these is interpreted as a group of MBPs with well-defined characteristic. As evidenced in Fig. 4, the wing is not well represented by a one-component fit, and therefore the need arises for including a second component to better depict the histogram. Moreover, when computing the X^2 test values to quantify the goodness of the fit by using the observed frequencies (i.e. values obtained in the data) and expected frequencies (i.e. theoretical values set by the fit), similar to Crockett et al. (2010), one finds a value of 1.3 for the one component fit model which yields a p-value of 0.5 meaning that there is only a 50–50 likelihood that the one component model is truly fitting the observed data. However, when computing the X^2 value for the two-component model (2.6) the picture changes as the p-value now reaches 0.8 meaning that there is now a 80 percent likelihood that the model truly fits the measurement values. Practically a one component model is just not flexible enough to produce a fit well enough to clearly be able to reproduce the data. The vertical line in blue at 45 km in Fig. 4 represents the diffraction limited spatial resolution of the GREGOR telescope at the given wavelength.

The distribution of the areas for 50% (see panel a in Fig. 3) exhibits a mean value of $\mu = 5700 \cdot | \div 1.6 \text{ km}^2$ ⁴ for the first component (I), that corresponds to 73% of the total distribution, being a more numerous group. Due to their sizes, this component likely corresponds to newborn MBPs or MBPs in formation, with an area range of $2200\text{--}15\,000 \text{ km}^2$. As for the second component (II), the mean value is $\mu = 16\,000 \cdot | \div 1.6 \text{ km}^2$, that corresponds to 27% of the total; this component also represents a family of MBPs but mature ones, with bigger areas in the range $6300\text{--}40\,000 \text{ km}^2$ but decreased in quantity. Table 1 lists the mean values of the distributions together with the factor that multiplies and divides it. The factor (e.g., the value 1.6) is proper of this type of curves, representing the value that multiplies and divides the mean value and indicates the shape of the distribution (log-normal; for more details see

⁴ Growth/fragmentation processes which follow multiplicative rules instead of additive rules follow log-normal distributions instead of normal distributions. This means that the additive standard deviation becomes a multiplicative standard deviation. For all the details see Limpert et al. (2008).

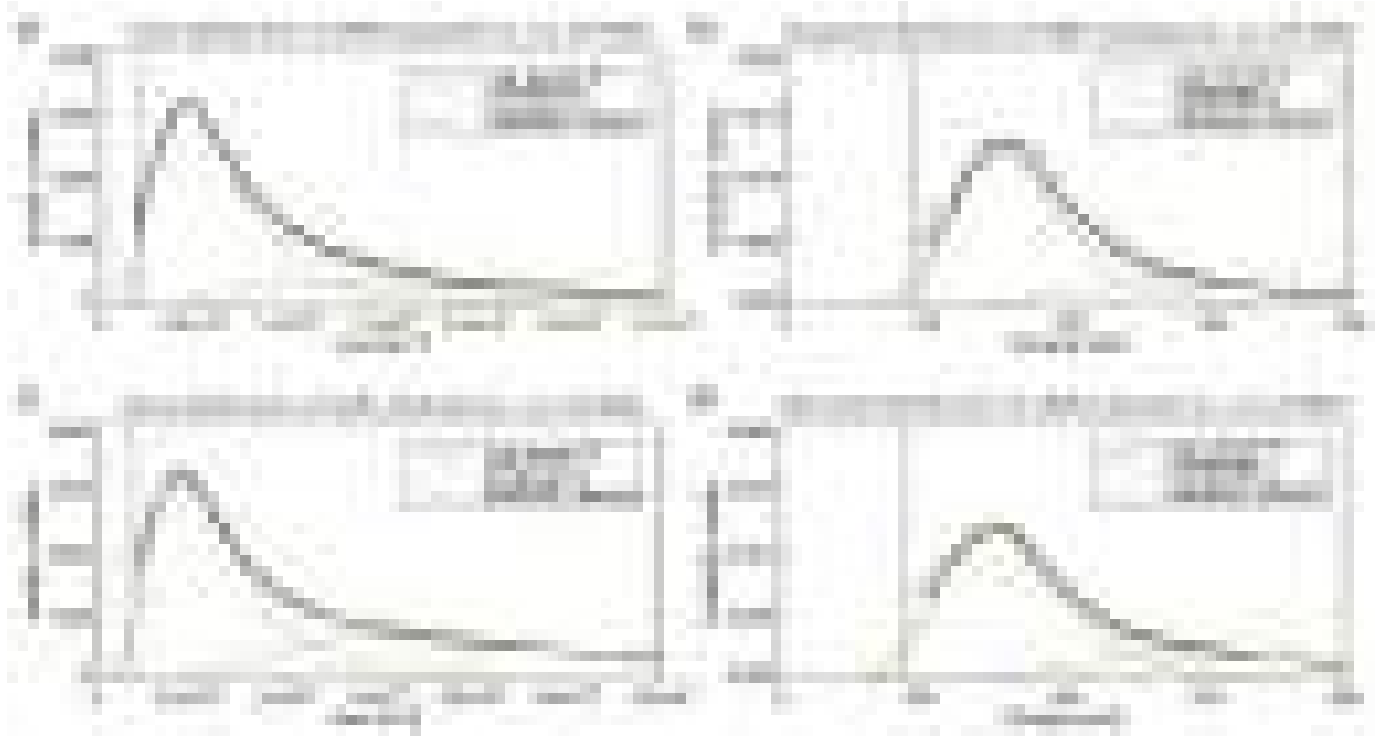


Fig. 3. Area distributions (*panels a,c*) and diameter distributions (*panels b,d*). Both cases are shown for the dataset-G with cut-off of 50% (*panels a,b*) and 80% (*panels c,d*). The plots depict a distribution with a log normal fit (red curves) and the two components (green curves). The blue vertical line around 2000 km^2 (45 km) for area (diameter) indicates the spatial resolution by diffraction of GREGOR.

Limpert et al. 2008). These results are in agreement with previous studies (e.g., Utz et al. 2009; Crockett et al. 2010), which established values between 7000 and 70 000 km^2 for the area of MBPs. Although our obtained mean value of 5700 km^2 is smaller than some of the previous calculations, it can be understood as evidence for the higher resolution of the GREGOR telescope affecting the detection procedure. For instance, Crockett et al. (2010) found a peak in the area distribution at $45 000 \text{ km}^2$ using both, *G*-band observations from the 76 cm Dunn Solar Telescope (DST) with a diffraction limit at $10 000 \text{ km}^2$ and numerical simulations using the MURaM code (Vögler et al. 2005).

Similarly, the distribution of diameters (see panel b in Fig. 3) has a mean value of $\mu = 80 \cdot | \div 1.3 \text{ km}$ for the 70% of the total distribution in the first component. Compared to that, the second component has a mean diameter of $\mu = 130 \cdot | \div 1.6 \text{ km}$ for the 30% of the distribution (see Table 1). Once more, each component (dotted green lines in Fig. 3), of this distribution depicts a population of small MBPs or in process of formation/disintegration. The first of these populations, with greater number of cases, remains in a diameter range of 50–140 km. Moreover, the second population of MBPs, that is characterised by having less number of elements, exhibits diameters spanning in a range from 50 to 330 km.

Figure 5 shows the velocity distribution for the same data set in their velocity components v_x and v_y together with the surface and scatter plots. Here, and in the following, positive values for v_x represent movement to the right, while a positive value for v_y means a movement to the top of the image (images oriented with solar north to the top of the image). The analysed velocities were calculated in a frame by frame, or MBP instance by MBP instance, fashion without considering any temporal averaging (except of the unavoidable averaging by the given cadence of the data). The velocity histogram, shown in panel c in the figure, is fitted by a Rayleigh function (red) that can be split into two



Fig. 4. Area distribution of MBPs for dataset-G (cut-off 50%) showing a one-component only fit (in red). Evidently, the tail of the histogram is not well-fitted, leading to the idea of two-component fit.

components (green). The mean value for the first component (I) of the velocity (see panel c in Fig. 5), that represents the 67% of the total distribution, is $\mu = 7.5 \text{ km s}^{-1}$. For the second component (II), the mean value is $\mu = 1.9 \text{ km s}^{-1}$ with 33% of the total. Each component plausibly indicates a different population of MBPs, as will be discussed in Sect. 4, the first of which exhibits a velocity in the range between 0 and 13 km s^{-1} and is more numerous. Accordingly, the second component depicts a population of MBPs with a velocity range from 0 to 5 km s^{-1} being less in number of elements. Unlike values for areas and diameters, velocity components v_x and v_y are well fitted by Gaussian distributions. Panels a and b in Fig. 5 show the frequency histograms of the velocity in x (v_x) and in y (v_y) with, again, evidence for a behaviour described by two components (component I and component II, as labeled for the green curves). A blue vertical line was located at the zero velocity value for clarity. In the case of the v_x the mean value is found to be $\mu = 0.009 \pm 4.8 \text{ km s}^{-1}$

Table 1. Areas and mean diameters for the different datasets (G and H), cut-offs (50 and 80%) and components (I and II).

Dataset	%	Component	Mean Area (km ²)	Mean Diameter (km)
G	50	I	5700 · ÷ 1.6	80 · ÷ 1.3
G	50	II	16000 · ÷ 1.6	130 · ÷ 1.6
G	80	I	5700 · ÷ 1.6	80 · ÷ 1.3
G	80	II	20000 · ÷ 1.6	150 · ÷ 1.5
H	50	I	230000 · ÷ 1.9	510 · ÷ 1.7
H	50	II	494000 · ÷ 1.2	780 · ÷ 1.3
H	80	I	37000 · ÷ 1.7	260 · ÷ 1.5
H	80	II	115000 · ÷ 1.2	380 · ÷ 1.2

for component I with a 80% of the total distribution. This component represents a population of MBPs with a range from -14 to 14 km s^{-1} and is characterised by a higher number of elements. On the other hand, component II has a mean value of $\mu = -0.14 \pm 1 \text{ km s}^{-1}$ with 20% of the total (as listed in Table 2) and corresponds to a population of MBPs in a velocity range from -3 to 3 km s^{-1} , besides it is characterised by a lower number of elements. Analogously, the distribution of v_y has a mean value for the component I of $\mu = -0.08 \pm 5.7 \text{ km s}^{-1}$ with a total contribution of 63%, representing a population of MBPs featuring velocities within a range from -17 to 17 km s^{-1} . This component features the higher number of elements, whereas component II has $\mu = -0.03 \pm 1.4 \text{ km s}^{-1}$ with a contribution of 37% to the total distribution, representing a population of MBPs, featuring velocities in the range from -4 and 4 km s^{-1} . This second component is characterised by a lower number of elements. Both distributions, v_x and v_y , have similar behaviour, as can be evidenced in Fig. 5. In the same figure it can be noticed that the underlying population of MBPs for component II of velocity distributions corresponds to component I for area and diameter distributions. This behaviour can be interpreted as MBPs of smaller sizes belonging to a population that exhibits a more extended velocity distribution and thus larger velocities on average. Contrarily, larger MBPs are characterised by having lower velocities, i.e. component I velocity distributions correspond to component II distributions for area and diameter. Panel d in the figure aims at visualizing a 3D plot combining the information from v_x and v_y values, and a scatter plot that better evidences the central concentration of points.

4. Influence of intensity cut-off and spatial resolution: GREGOR versus Hinode

In the results described in Sect. 3 for dataset-G, a percentage of cut-off at 50% is used, that is to say, the commonly employed value by previous similar studies (see e.g., Berger et al. 1995). However, it is necessary to evaluate whether that definition, which is commonly used, yields the most accurate results. In order to do so, the definition that is established is based on finding the existing relationship between the size of MBPs and the percentage of intensity cut-off. Figure 6 represents the main scheme behind the characterisation of MBPs according to the intensity profile, displaying the enlargement in identified areas with the reduction of the intensity cut-off. The plot in panel b in Fig. 6 evidences that the more horizontal the curve is, the more independent the MBP size will be from the cut-off percentage parameter. Panel c shows the evolution of identified areas

with the intensity thresholding in a sample image, for cut-off values of 0, 25, 50 and 80%, respectively. Black contours in the lower row highlight the corresponding areas, while red contours are overplotted to compare the area enlargement from one cut-off value to a lower one, and therefore affecting the recognized features, i.e. MBP core, MBP core and wall, the whole MBP and surroundings, and the MBP and some dark intergranular lanes. In panel b of the figure the stability zone is evidenced in the range from 60% to 100%. A median of 80% is the final representative value selected as the cut-off percentage (see also Bovelet & Wiehr 2001, who used a similar approach to ‘shrink’ detected granules to correct sizes). The description of the results using this new cut-off value is performed to compare both cut-off values at 50% and 80%. The examination of areas for this cut-off results in a two-component distribution with log-normal fits, as shown in panel c of Fig. 3, with the first component having a mean value of $\mu = 5700 \cdot | \div 1.6 \text{ km}^2$ and representing 57% of the total distribution. Component I corresponds to a large family of newborn MBPs under formation, whose areas cover a range from 2200 to 15 000 km². The other component is characterised by a mean value of $\mu = 20\,000 \cdot | \div 1.6 \text{ km}^2$ and depicts 43% of the total distribution; this second component corresponds to a family of mature MBPs with areas ranging from 7800 to 52 000 km² but with a smaller number of elements. The previous results are within the range of other studies, like those described in Wiehr et al. (2004), Utz et al. (2009), Abramenco et al. (2010), Liu et al. (2018) to list a few, with established values between 7000 and 70 000 km².

As for the distribution of diameters, shown in panel d in Fig. 3, the mean value corresponds to $\mu = 80 \cdot | \div 1.3 \text{ km}$, 70% of the total, for the first component; this corresponds to a group of MBPs with a range of diameters between 50 and 140 km and with a large number of elements. The second component has a mean value of $\mu = 150 \cdot | \div 1.5 \text{ km}$, 30% of the distribution; this corresponds to a group of MBPs with diameters from 70 to 340 km, with a lower number of elements. Table 1 summarizes the information for mean areas and diameters. In the panels c and d in Fig. 3, the blue vertical line around 2000 km² (45 km) represents the spatial resolution limited by the diffraction of GREGOR for areas and diameters, respectively. The results for area and diameter for dataset-G do not change significantly when raising the cut-off value from 50% to 80%, as shown in panels a vs. c and b vs. d in Fig. 3. Indicating the superb quality of the GREGOR telescope and its HiFi instrument as well as the proper application of the identification and analysis algorithms as the results are practically independent of the chosen thresholding parameter.

Nevertheless, for the case of dataset-H, in which the spatial resolution is not as high, the results are strongly influenced by the thresholding as plotted in Fig. 7. Similarly as for dataset-G, these distributions also exhibit a bimodal contribution with two protruding peaks (components I and II). The fit parameters of the log normal fits are shown on Table 1. For the case of cut-off at 80%, shown in panel c in Fig. 7, the mean area of the first component is $\mu = 37\,000 \cdot | \div 1.7 \text{ km}^2$ and represents 71% of the total distribution. On the other hand, the mean value of the second component is $\mu = 115\,000 \cdot | \div 1.2 \text{ km}^2$ and corresponds to 29% of the total distribution. Values to the left from the blue vertical line are not reliable as they lie below the spatial resolution by diffraction for Hinode (i.e. 21 000 km²). Considering that the second component of the distribution surpasses the values reported in other studies, e.g., areas from 7000 to 70 000 km² in Utz et al. (2009), Crockett et al. (2010),

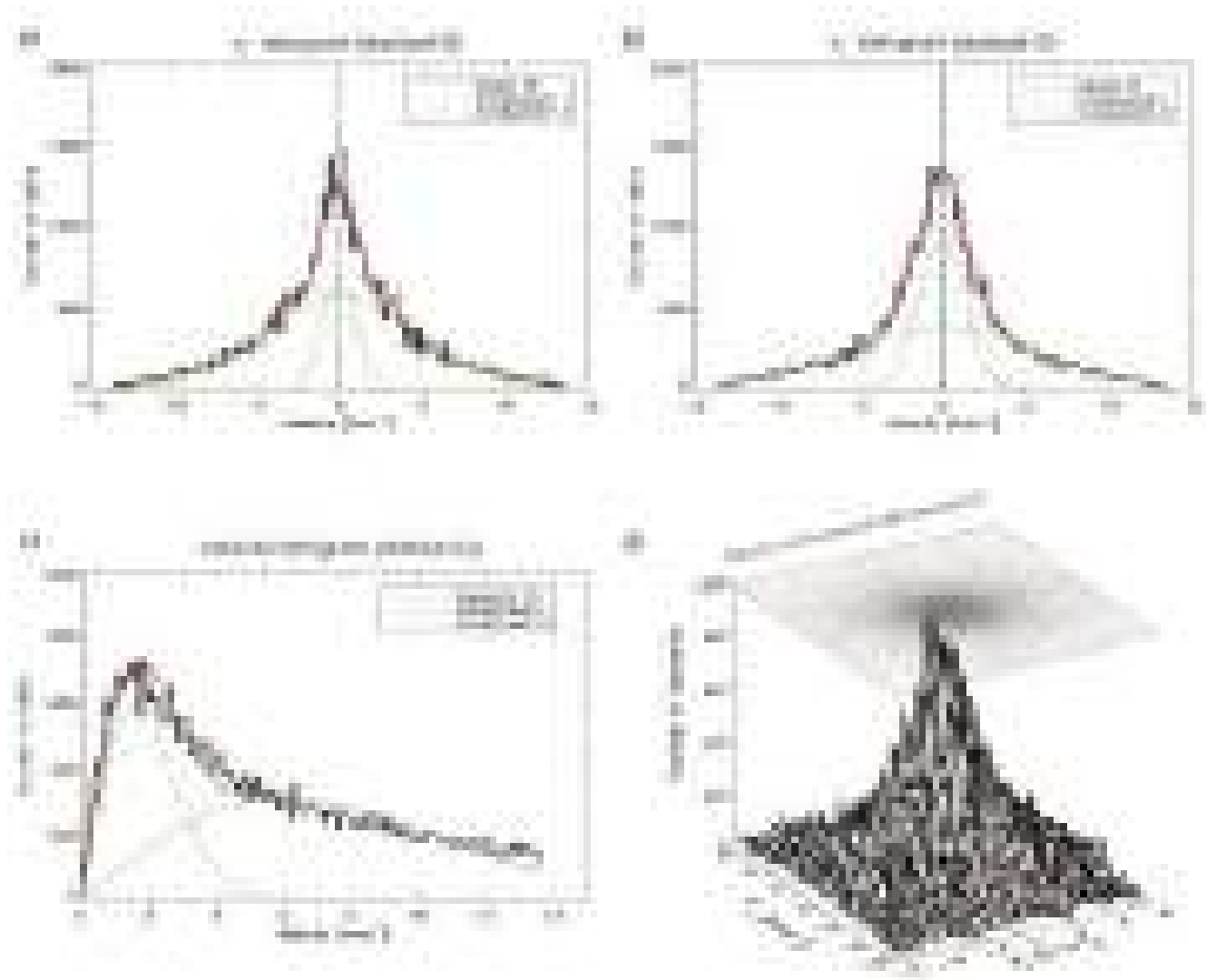


Fig. 5. Velocity histograms of MBPs for the GREGOR set. *Top*: v_x and v_y velocity components with the normal fit curve (red) and the two components of the distribution (green). *Bottom left*: velocity with the Rayleigh fit in red and the two components in green. *Bottom right*: surface and scatter plot of the v_x and v_y components.

Table 2. Mean velocity values (in km s^{-1}) for the two datasets (G and H) and components (I and II).

Dataset	Component	Mean v_x	σ_{v_x}	Mean v_y	σ_{v_y}	Mean effective velocity	σ_{v_R}
G	I	0.009	4.8	-0.08	5.7	7.5	6.1
G	II	-0.14	1	-0.03	1.4	1.9	1.5
H	I	-0.063	1.7	0.024	1.5	2.3	2.8
H	II	-0.00007	0.7	-0.024	0.6	1.1	1.4

Notes. The fit parameters (st.dev.) σ are indicated.

Abramenko et al. (2010), Yang et al. (2014), it is compelling to discuss the meaning of it. A plausible explanation relies on representing two different population of elements, one with areas in the range from 22 000 to 63 000 km^2 that constitutes a family of MBPs (with greater number of elements), and the second with values from 96 000 to 138 000 km^2 and likely to correspond to a family of small granules in process of formation or segments of granules, with a lower number of elements, considering the granules have values of area between the range of 105 000–2 600 000 km^2 (Kawaguchi 1980).

For the case of diameters computed with the same cut-off value (80%), the mean value of the first component of the bimodal distribution, plotted in panel d of Fig. 7, is $\mu = 260 \cdot | \div 1.5 \text{ km}$ and corresponds to the 84% of the total, and with a greater of number elements. Diameters are in the range from 170 to 390 km, in agreement with the values reported by other studies (Utz et al. 2009), which are between 100 and 300 km. On the other hand, the mean value of component II is $\mu = 380 \cdot | \div 1.2 \text{ km}$, which corresponds to a population of forming granules (or fragments) with values from 310 to 450 km, and

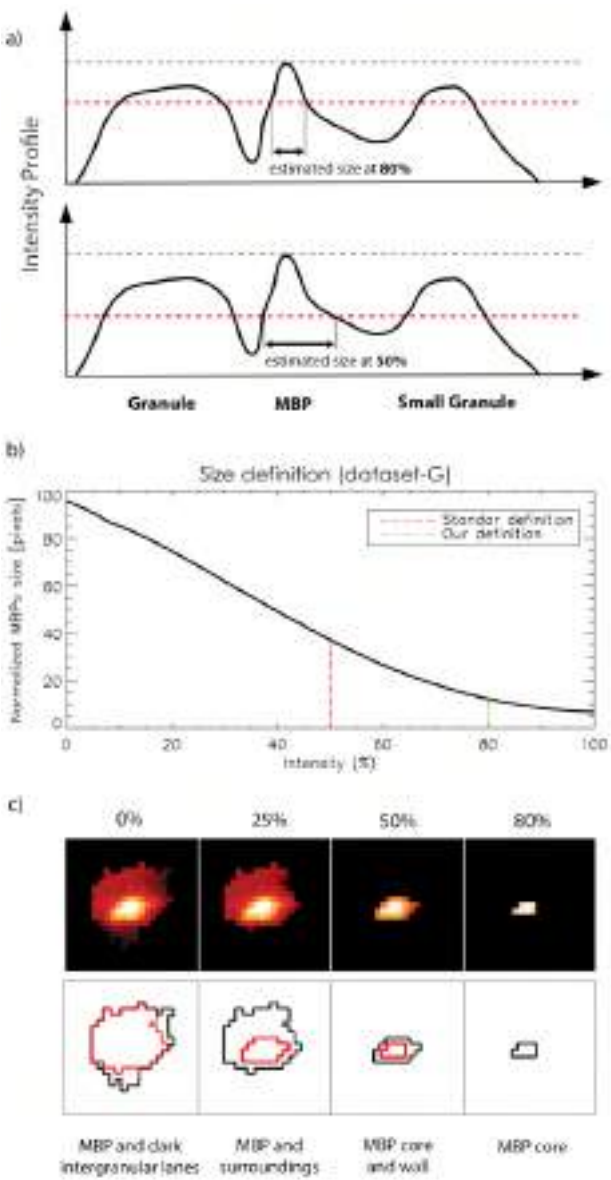


Fig. 6. Intensity characterisation of MBPs. *Panel a:* schematic side view cut of the solar surface in intensity with two granules and a MBP. The dashed horizontal line illustrates the cutting level and the following size of a segmented MBP. *Panel b:* criteria for setting the area of a MBP. The concept that underlies this criterion is based on finding a range of independence between the size of the MBP and the intensity cut-off percentage. *Panel c:* intensity thresholding (for values of 0, 25, 50 and 80%) applied over a segmented sample image and the effect on the identification of features, as labeled. The lower row represents contours in black for each frame in the upper row, and in red for every corresponding frame on the right, in order to compare the progressive area enlargement as the intensity threshold reduces from 80 to 0%. For exhaustive discussion refer to the main text.

lower number of elements. This result is comparable to the range from 370 to 1800 km, found by Kawaguchi (1980).

To verify the precision in the definition of size described above, the distribution of the areas and diameters is calculated using the commonly definition (intensity cut-off at 50%). Panels a and b in Fig. 7 show the resulting two bimodal distributions that are fitted with log-normal curves (red), together with the two components that constitute it (green). Table 1 lists the fit parameters of such distributions. The mean value for the area of

the first component is $\mu = 230\,000 \cdot | \div 1.9 \text{ km}^2$ and represents the 80% of the total distribution. For the second component, the value is $\mu = 490\,000 \cdot | \div 1.2 \text{ km}^2$, which corresponds to 20% of the total. Surprisingly, the component I of this distribution, with higher number of elements, shows now areas that are in the range between 120 000–400 000 km². Thus changing the thresholding level in the case of Hinode changed quite dramatically the estimated size of the features. One has to keep in mind here that the same segments were identified in both cases and just the “estimation” of the true size changed by the parameter. A possible explanation for the effect of larger sizes is shown in Fig. 6. Panel a shows a schematic representation of the solar surface in a side-cut view. In between two granules we can find a MBP situated in the intergranular lane. The segmentation algorithm will grow all segments starting from the brightest pixel until the growing segments will stop their growth when encountering a neighbouring segment at the darkest intergranular pixels. Thus, a MBP segment can contain quite a large extent of the intergranular area and needs after segmentation to be cut down to the brightest part (corresponding to the true size of the MBP). If the cut-off, however, is chosen too low, the MBP size can be artificially extended by intergranular dark lane pixels. One can see that varying the cut-level by about 20% of the brightest intensity does not lead to a significant change of size, as shown in panel b in Fig. 6. This means that the brightest pixels of an MBP (the core structure) have homogenous brightness distribution, and thus they are under equivalent physical conditions. Taking the threshold to lower brightness levels, the structure increases in size as more pixels surrounding the brightest core of the structure are added. It is preferable to choose a threshold sufficiently high as well as in a part of the curve where it is nearly horizontal as this corresponds to a greater independence of the estimated size from the chosen threshold parameter. Thus the first component is also at the 50% cut-off level truly an MBP size distribution, however, sizes are estimated too large by a too deep cut level. The second component found in the Hinode data (Fig. 7) is interpreted as corresponding to a family of granules with area in the range of 400 000–600 000 km², but with a lower number of elements. These results are in agreement with the range found by Kawaguchi (1980) of 105 000–2 600 000 km². By visually inspecting some of the images we confirm the second distribution is in agreement with false detection of small granules misinterpreted as MBPs. The analysis evidences that the value for the cut-off at 80% manifests greater detection accuracy i.e. 22 000–62 000 km², whereas results based on the commonly definition provide very large sizes for the MBPs of the order of 122 000–500 000 km². Table 1 compiles the fitted values. Mean value of the first component of this bimodal distribution is $\mu = 510 \cdot | \div 1.7 \text{ km}$ and represents the 81% of the totality of the same, and for the second distribution is $\mu = 780 \cdot | \div 1.3 \text{ km}$ with a 19%.

Moreover we can conclude that the resolution of Hinode is not sufficient to detect the bi-component composition of the size distribution of MBPs. Besides, due to the lower resolution there is a certain level of misidentified forming granules detected in the Hinode data set constituting the second component in the case of MBP size distribution for dataset-H.

Figure 8 shows the results for the computed velocities. Panels a and b in the figure depict the frequency histograms for the components x and y of the velocity, i.e. V_x and V_y , respectively, with the fitted curves in red (normal distribution) and the two components in green dotted curves. The fit parameters μ and σ are summarized in Table 2. Panel c in the figure displays the effective velocity fitted by Rayleigh distribution (red)

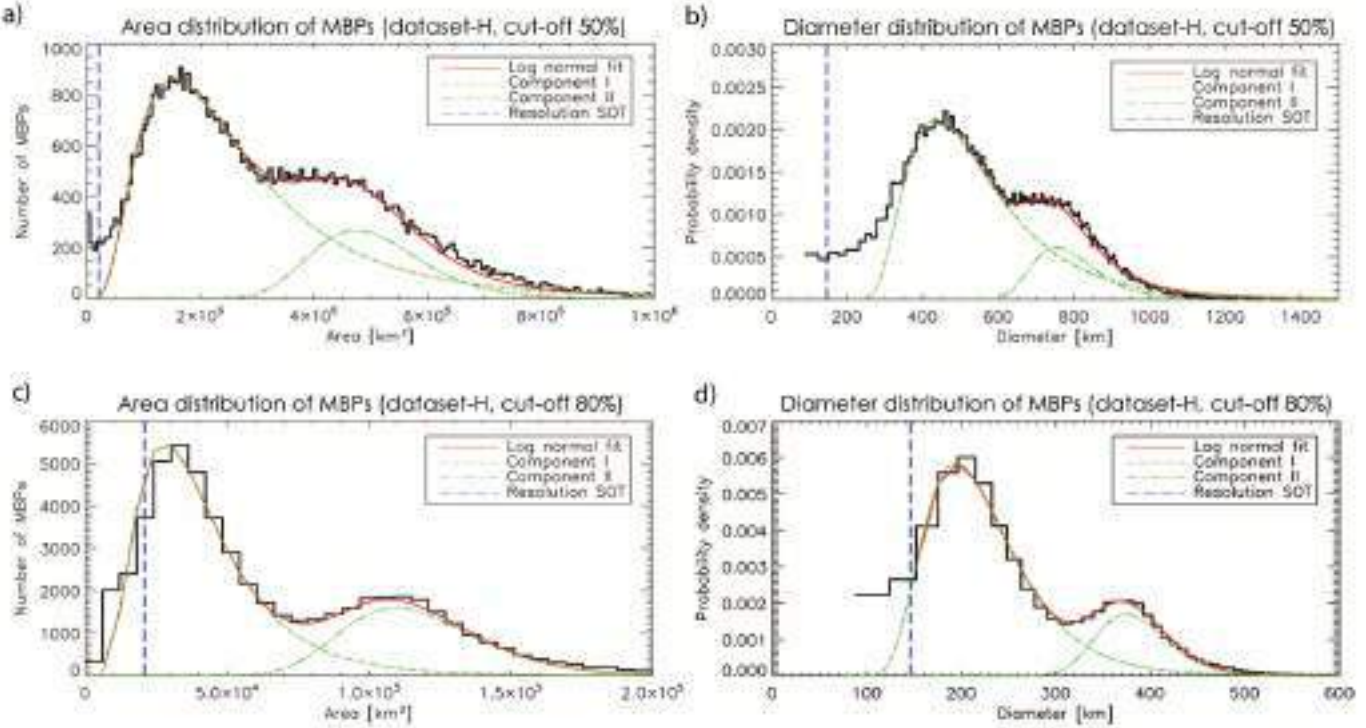


Fig. 7. Area distributions (panels *a,c*) and diameter distributions (panels *b,d*). Both cases are shown for the dataset-H with cut-off of 50% (panels *a,b*) and 80% (panels *c,d*). The plots depict a bimodal distribution with a log-normal fit (red curves) and the two components (green curves). The blue vertical line at 146 km (around $21\,000\,\text{km}^2$) indicates the spatial diffraction limit of Hinode.

and the two components (green). The mean velocity value for component I, that represents the 49% of the total distribution, is $\mu = 2.3\,\text{km}\,\text{s}^{-1}$ and is characterised by displaying a velocity range from 0 to $6\,\text{km}\,\text{s}^{-1}$ and with a slightly smaller number of elements. Component II has a mean value $\mu = 1.1\,\text{km}\,\text{s}^{-1}$ and represents 51% of the total distribution; indicating a population of MBPs with a velocity range from 0 to $3\,\text{km}\,\text{s}^{-1}$ and with a slightly higher number number of elements.

We expressed the velocity components in 2 orthogonal directions (x, y ; horizontal and vertical directions), which correspond to v_x and v_y , respectively, displaying Gaussian distributions as it is expected in the case of a non-preferential direction random walk process. A different outcome would only be expected if there were reasons for a large-scale flow-field with preferred directions like in the moat flows of sunspots. Panels *a* and *b* in Fig. 8 show the frequency histograms of v_x and v_y , respectively, fitted to normal curves (red) and the corresponding two components (green). A vertical line (blue) is located at the value of velocity equal to $0\,\text{km}\,\text{s}^{-1}$ for clarity. The mean value for v_x is $\mu = -0.063 \pm 1.7\,\text{km}\,\text{s}^{-1}$ for the component I (76% of the total) and represents a population of MBPs in a range from -5 to $5\,\text{km}\,\text{s}^{-1}$ with greater number of elements. For component II, the mean value is $\mu = -0.00007 \pm 0.7\,\text{km}\,\text{s}^{-1}$, 24% of the total distribution, representing a population of MBPs in a range from -2.2 to $2.2\,\text{km}\,\text{s}^{-1}$ but lower number of elements. For v_y , the mean value is $\mu = 0.024 \pm 1.5\,\text{km}\,\text{s}^{-1}$ for component I (73% of the total) and $\mu = -0.024 \pm 0.6\,\text{km}\,\text{s}^{-1}$ for component II (27% of the total distribution). In panels *a* and *b* in Fig. 8 both, v_x and v_y , exhibit essentially the same distribution for the two components. Component I represents a population of MBPs with v_y from -4.5 to $4.5\,\text{km}\,\text{s}^{-1}$ with a slightly higher number of elements, whereas component II indicates a population of MBPs with v_y from -1.9 to $1.9\,\text{km}\,\text{s}^{-1}$ but with lower number of elements.

5. Discussion

It is well-known that the magnetic field inhibits convection and therefore plasma velocities are expected to reduce while the magnetic field intensifies. Thus, it is highly likely that this physical mechanism is underlying the two-component behaviour. Some previous investigations have dealt with velocity distributions of MBPs in different environments. Jafarzadeh et al. (2017) showed the variation in diffusion of MBPs across a network cell (with regions of flux emergence), whereas Keys et al. (2014) demonstrated the velocity distribution in three regions of varying background flux and show that MBPs in regions of higher flux have lower transverse velocities. The authors suggest that this is due to convection being disrupted in regions of higher flux, resulting in more regions of stagnation points for the MBPs reducing velocities. The regions of disrupted convection would relate to the small granules that are mentioned in this work. Convective cells are smaller in regions of higher flux, which, in turn, creates more regions where there are several intersecting intergranular lanes, forming the stagnation points where MBPs get trapped, thus resulting in a lower peaked velocity distribution (i.e. a peak at a lower velocity). We expect that the differences observed in our analysis are due to where the MBPs are found in the quiet-Sun regions (i.e. whether they can be classed as network or internetwork MBPs), but this requires further analysis of velocity flow maps, with the precise testing of parameters and comparison with magnetograms, for a definitive statement to be manifested. This will be the focus of a subsequent study.

The first group of MBPs, exhibiting lower velocities, are likely to harbour strong magnetic fields that impedes the rapid movement of this population. On the other hand, the second group, with greater velocities, would correspond to weaker magnetic fields letting them move faster while embedded in the photospheric plasma flow. And indeed there is a recent finding

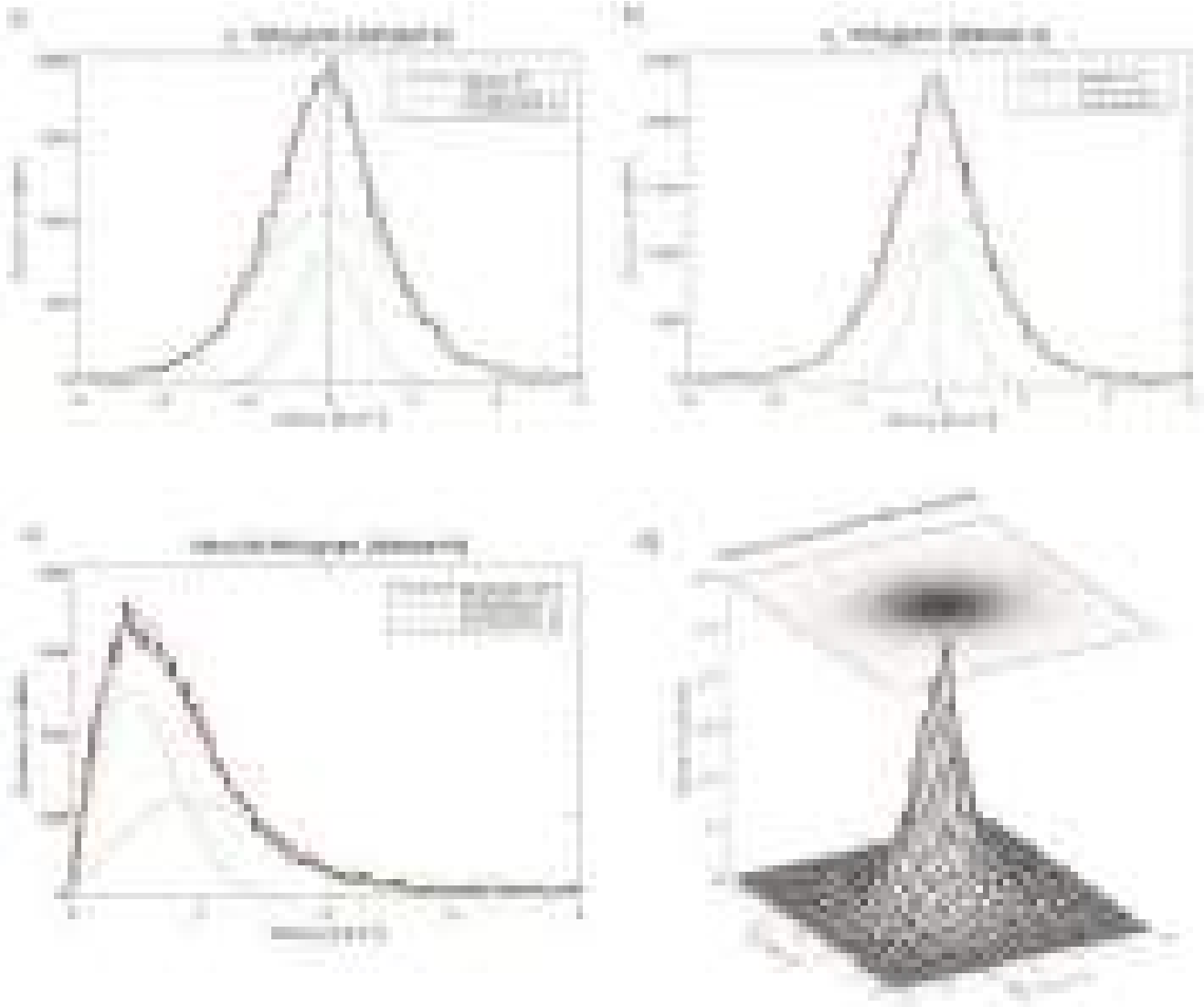


Fig. 8. Velocity histograms of MBPs for the Hinode set. *Top*: v_x and v_y velocity components with the normal fit curve (red) and the two components of the distribution (green). *Bottom left*: Velocity with Rayleigh fit in red and the two components in green. *Bottom right*: surface and scatter plot of the v_x and v_y components.

suggesting also, for the magnetic field strength distribution of MBPs, a bi-component composition as evidenced by Keys et al. (2019). Figure 1 shows (from left to right) *G*-band images of the FOV, map of velocities computed from local correlation tracking (LCT) techniques, and map of divergences for dataset-G (top row) and dataset-H (bottom row). This figure shows a spatial correspondence between the location of MBPs and lower velocities (red crosses in middle panels) and, in turn, with negative divergences (black crosses in right-most panels). Blue regions in the divergence maps are tracing intergranular lanes. This is in concordance with the presence of two populations of MBPs, one group located in the network (with stronger magnetic fields and thus likely the larger MBPs showing lower velocities) and the other population of MBPs located in the internetwork (with weaker magnetic fields, harboring smaller MBPs which can move faster), though a detailed analysis including magnetic field information is out of the scope of this analysis and will be covered in a future work.

Moreover the inspection of the results obtained by GREGOR and Hinode highlight the necessity for high spatial as well

as temporal resolution as it is not possible to differentiate the two populations of MBPs in size with the Hinode instrument while it became apparent with the GREGOR data set. Besides, at the same time the higher resolution of GREGOR helps to eliminate the misidentified population of small granules. Moreover, we can find higher velocities by the GREGOR telescope which are related to the better temporal and spatial resolution as discussed in Utz et al. (2010). The authors claim and verify in Utz et al. (2012) that a random walk motion observed under higher temporal cadence conditions would yield higher velocities as the length of the travelled path between two fixed time instances of the MBP increases. Such results are of particular value for MHD wave simulations as more rapid footpoint motions of the flux-tube, i.e. MBP will yield MHD waves carrying more energy into the higher atmosphere or possibly creating the recently observed magnetic field line switchbacks (e.g., Choudhuri et al. 1993; Vigeesh et al. 2009; Magyar et al. 2021). Finally, with the hindsight of this work, it is even possible to find evidence for the two-component velocity distributions in earlier works such as Bodnárová et al. (2014) in which the authors

used DOT (Dutch Open Telescope; [Rutten et al. 2004](#)) data. Evidently in their Fig. 2, depicting the magnitude of the MBP velocity, the second Rayleigh component has been left unnoticed by the authors, who, however, state that there is widening discrepancy for the high velocity tail compared to their one component Rayleigh fit.

6. Conclusions

In the present investigation, the study of the dynamics of MBPs on the solar photosphere for two quiet Sun regions, close to the central meridian of the solar disk, was carried out. Observations from ground-based and space-borne solar telescopes were employed, specifically using the HiFI/GREGOR and the SOT/Hinode instruments. Unprecedented results for the size, diameter, and velocity of MBPs were found as a direct consequence of the excellent spatial resolution of the observations with the GREGOR telescope. The results of the characterisation of physical parameters of MBPs are in correspondence with others found in previous investigations (see [Muller et al. 1994](#); [Utz et al. 2009](#); [Crockett et al. 2010](#); [Liu et al. 2018](#)). The most important findings of the present investigation are related to the distribution of sizes, diameters, and velocities of MBPs. The results obtained with the two sets of observational data exhibit, for both area and diameter, a log-normal distribution, in agreement with previous observational and numerical studies (e.g., [Crockett et al. 2010](#)). As suggested by [Bogdan et al. \(1988\)](#), the underlying fragmentation process might be responsible for log-normal distributions. In this work, the log-normal distributions of areas and diameters are found to be well described by two different components, each of which is proposed to correspond to a different population of solar features. As for velocities of MBPs, results show a Rayleigh distribution with the presence of two clear components, representing different groups of MBPs. For dataset-H (Hinode), a population of MBPs in addition to small granules were found, in the area and diameter results. This is due to difficulties arising by the lower spatial resolution of the telescope. On the other hand, in the velocity results two populations of MBPs were found. Similarly, for dataset-G (GREGOR), two populations of MBPs were found for areas, diameters and velocities, and no misidentifications (small granules) were found. This is by virtue of the prominent resolution of the telescope. Finally, another finding related to the effect of the intensity cut-off is that the cut-off percentage value of 80% better describes the area and diameter of the MBPs under study, which were not so large but consistent with those found in [Utz et al. \(2009\)](#), [Kawaguchi \(1980\)](#). In our case, using the commonly used definition cut-off at 50% resulted in misidentification of granules and excessively large values of MBPs for the results of area and diameter.

With this study at hand, and the previous study of [Keys et al. \(2019\)](#) describing two-component magnetic field strength distributions for MBPs, evidence is growing for a paradigm shift from a single population of MBPs to a more complex model, where we will have to deal in the future with two distinct types of MBPs, likely related to network and intranetwork magnetic fields and thus maybe even to the global magnetic field dynamo versus a shallow surface magnetic field dynamo. The new generation of solar telescopes, e.g., Daniel K. Inouye Solar Telescope (DKIST; [Rast et al. 2021](#)) and European Solar Telescope (EST; [Jurčák et al. 2019](#)) with larger apertures and, in turn, better spatial resolution, will shed more light to the two-component groups enabling further confirmation of the characterisation of MBPs presented in this study.

Acknowledgements. Part of this work was supported by Austrian FWF – Der Wissenschaftsfonds project number P27800 as well as the German Deutsche Forschungsgemeinschaft, DFG project number Ts 17/2–1. SVD acknowledges support by the Beyond Research Program between University of Graz and Universidad Nacional de Colombia. SJGM acknowledges the support of grants PGC2018-095832-B-I00 (MCIU) and ERC-2017-CoG771310-PI2FA (European Research Council). PG acknowledges the support of the project VEGA 2/0048/20. P.Z. acknowledges support from the Stefan Schwarz fund for post-doctoral researchers awarded by the Slovak Academy of Sciences. This research data leading to the results obtained has been supported by SOLARNET project that has received funding from the European Union's Horizon 2020 research and innovation programme under grant agreement no 824135. The 1.5-meter GREGOR solar telescope was built by a German consortium under the leadership of the Kiepenheuer Institute for Solar Physics in Freiburg with the Leibniz Institute for Astrophysics Potsdam, the Institute for Astrophysics Göttingen, and the Max Planck Institute for Solar System Research in Göttingen as partners, and with contributions by the Instituto de Astrofísica de Canarias and the Astronomical Institute of the Academy of Sciences of the Czech Republic. The authors are grateful for the possibility to use Hinode data. Hinode is a Japanese mission developed and launched by ISAS/JAXA, collaborating with NAOJ as a domestic partner, NASA and UKSA as international partners. Scientific operation of the Hinode mission is conducted by the Hinode science team organized at ISAS/JAXA. This team mainly consists of scientists from institutes in the partner countries. Support for the post-launch operation is provided by JAXA and NAOJ (Japan), UKSA (UK), NASA, ESA, and NSC (Norway). We would like to express our gratitude to the anonymous referee for all the valuable comments that helped us to improve the presentation of the results and ideas highlighted in this work.

References

- Abramenko, V., Yurchyshyn, V., Goode, P., & Kilcik, A. 2010, [ApJ](#), **725**, L101
- Beck, C., Bellot Rubio, L. R., Schlichenmaier, R., & Süttlerin, P. 2007, [A&A](#), **472**, 607
- Berger, T. E., & Title, A. M. 1996, [ApJ](#), **463**, 365
- Berger, T. E., Schrijver, C. J., Shine, R. A., et al. 1995, [ApJ](#), **454**, 531
- Berger, T. E., Rouppe van der Voort, L., & Löfdahl, M. 2007, [ApJ](#), **661**, 1272
- Berkefeld, T., Schmidt, D., Soltau, D., von der Lühe, O., & Heidecke, F. 2012, [Astron. Nachr.](#), **333**, 863
- Bodnárová, M., Utz, D., & Rybák, J. 2014, [Sol. Phys.](#), **289**, 1543
- Bogdan, T. J., Gilman, P. A., Lerche, I., & Howard, R. 1988, [ApJ](#), **327**, 451
- Bovelet, B., & Wiehr, E. 2001, [Sol. Phys.](#), **201**, 13
- Choudhuri, A. R., Auffret, H., & Priest, E. R. 1993, [Sol. Phys.](#), **143**, 49
- Crockett, P. J., Mathioudakis, M., Jess, D. B., et al. 2010, [ApJ](#), **722**, L188
- Danilovic, S., Schüssler, M., & Solanki, S. K. 2010, [A&A](#), **509**, A76
- Deinzer, W., Hensler, G., Schüssler, M., & Weisshaar, E. 1984, [A&A](#), **139**, 435
- Dunn, R. B., & Zirker, J. B. 1973, [Sol. Phys.](#), **33**, 281
- Erdélyi, R., & Ballai, I. 2007, [Astron. Nachr.](#), **328**, 726
- Fedun, V., Shelyag, S., & Erdélyi, R. 2011, [ApJ](#), **727**, 17
- Feng, S., Deng, L., Yang, Y., & Ji, K. 2013, [Ap&SS](#), **348**, 17
- Fischer, C. E., de Wijn, A. G., Centeno, R., Lites, B. W., & Keller, C. U. 2009, [A&A](#), **504**, 583
- Ishikawa, R., Tsuneta, S., Kitakoshi, Y., et al. 2007, [A&A](#), **472**, 911
- Jafarzadeh, S., Solanki, S. K., Stangalini, M., et al. 2017, [ApJS](#), **229**, 10
- Jess, D. B., Mathioudakis, M., Erdélyi, R., et al. 2009, [Science](#), **323**, 1582
- Jess, D. B., Mathioudakis, M., Christian, D. J., Crockett, P. J., & Keenan, F. P. 2010, [ApJ](#), **719**, L134
- Jurčák, J., Collados, M., Leenaarts, J., van Noort, M., & Schlichenmaier, R. 2019, [Adv. Space Res.](#), **63**, 1389
- Kawaguchi, I. 1980, [Sol. Phys.](#), **65**, 207
- Keys, P. H., Mathioudakis, M., Jess, D. B., Mackay, D. H., & Keenan, F. P. 2014, [A&A](#), **566**, A99
- Keys, P. H., Reid, A., Mathioudakis, M., et al. 2019, [MNRAS](#), **488**, L53
- Kleint, L., Berkefeld, T., Esteves, M., et al. 2020, [A&A](#), **641**, A27
- Klimchuk, J. A. 2006, [Sol. Phys.](#), **234**, 41
- Kosugi, T., Matsuzaki, K., Sakao, T., et al. 2007, [Sol. Phys.](#), **243**, 3
- Kuckein, C. 2019, [A&A](#), **630**, A139
- Kuckein, C., Denker, C., Verma, M., et al. 2017, in *Fine Structure and Dynamics of the Solar Atmosphere*, eds. S. Vargas Domínguez, A. G. Kosovichev, P. Antolin, & L. Harra, 327, 20
- Limpert, E., Stahel, W. A., & Abbt, M. 2008, [BioScience](#), **51**, 341
- Liu, Y., Xiang, Y., Erdélyi, R., et al. 2018, [ApJ](#), **856**, 17
- Magyar, N., Utz, D., Erdélyi, R., & Nakariakov, V. M. 2021, [ApJ](#), **911**, 75
- Mathioudakis, M., Jess, D. B., & Erdélyi, R. 2013, [Space Sci. Rev.](#), **175**, 1
- Muller, R. 1983, [Sol. Phys.](#), **85**, 113
- Muller, R., Hulot, J. C., & Roudier, T. 1989, [Sol. Phys.](#), **119**, 229
- Muller, R., Roudier, T., Vigneau, J., & Auffret, H. 1994, [A&A](#), **283**, 232

- Nagata, S., Tsuneta, S., Suematsu, Y., et al. 2008, [ApJ](#), **677**, L145
- Nisenson, P., van Ballegooijen, A. A., de Wijn, A. G., & Süttlerlin, P. 2003, [ApJ](#), **587**, 458
- Parker, E. N. 1978, [ApJ](#), **221**, 368
- Rast, M. P., Bello González, N., Bellot Rubio, L., et al. 2021, [Sol. Phys.](#), **296**, 70
- Riethmüller, T. L., Solanki, S. K., Berdyugina, S. V., et al. 2014, [A&A](#), **568**, A13
- Rutten, R. J., Hammerschlag, R. H., Bettonvil, F. C. M., Süttlerlin, P., & de Wijn, A. G. 2004, [A&A](#), **413**, 1183
- Samanta, T., Tian, H., Yurchyshyn, V., et al. 2019, [Science](#), **366**, 890
- Sánchez Almeida, J., Márquez, I., Bonet, J. A., Domínguez Cerdeña, I., & Muller, R. 2004, [ApJ](#), **609**, L91
- Scharmer, G. B., Brown, D. S., Pettersson, L., & Rehn, J. 1985, [Appl. Opt.](#), **24**, 2558
- Schmidt, W., von der Lühe, O., Volkmer, R., et al. 2012, [Astron. Nachr.](#), **333**, 796
- Schüssler, M., Shelyag, S., Berdyugina, S., Vögler, A., & Solanki, S. K. 2003, [ApJ](#), **597**, L173
- Spruit, H. C. 1979, [Sol. Phys.](#), **61**, 363
- Stanislavsky, A., & Weron, K. 2009, [Ap&SS](#), **104**
- Steiner, O., Hauschildt, P. H., & Bruls, J. 2001, [A&A](#), **372**, L13
- Tsuneta, S., Ichimoto, K., Katsukawa, Y., et al. 2008, [Sol. Phys.](#), **249**, 167
- Utz, D., Hanslmeier, A., Möstl, C., et al. 2009, [A&A](#), **498**, 289
- Utz, D., Hanslmeier, A., Müller, R., et al. 2010, [A&A](#), **511**, A39
- Utz, D., Hanslmeier, A., Müller, R., et al. 2012, in Hinode-3: The 3rd Hinode Science Meeting, eds. T. Sekii, T. Watanabe, & T. Sakurai, [ASP Conf. Ser.](#), **454**, 55
- Utz, D., Jurčák, J., Hanslmeier, A., et al. 2013, [A&A](#), **554**, A65
- Utz, D., del Toro Iniesta, J. C., Bellot Rubio, L. R., et al. 2014, [ApJ](#), **796**, 79
- Utz, D., Müller, R., Thonhofer, S., et al. 2016, [A&A](#), **585**, A39
- Utz, D., Müller, R., & Van Doorsselaere, T. 2017, [PASJ](#), **69**, 98
- Vigeesh, G., Hasan, S. S., & Steiner, O. 2009, [A&A](#), **508**, 951
- Viticchié, B., Del Moro, D., Berrilli, F., Bellot Rubio, L., & Tritschler, A. 2009, [ApJ](#), **700**, L145
- Vögler, A., Shelyag, S., Schüssler, M., et al. 2005, [A&A](#), **429**, 335
- Wiehr, E., & Bovelet, B. 2009, [Cent. Eur. Astrophys. Bull.](#), **33**, 19
- Wiehr, E., Bovelet, B., & Hirzberger, J. 2004, [A&A](#), **422**, L63
- Wöger, F., & von der Lühe, O. I. 2008, in Advanced Software and Control for Astronomy II, eds. A. Bridger, & N. M. Radziwill, [SPIE Conf. Ser.](#), **7019**, 70191E
- Yang, Y.-F., Lin, J.-B., Feng, S., et al. 2014, [Res. Astron. Astrophys.](#), **14**, 741
- Zakharov, V., Gandorfer, A., Solanki, S. K., & Löfdahl, M. 2005, [A&A](#), **437**, L43

Discussion and Conclusions

The main topic of this work is the study and analysis of the interaction between the solar plasma and the magnetic fields. The three research papers presented three different studies which investigate different magnetic features namely active regions, solar pores, and magnetic bright points. In these studies, we cover different spatial and temporal scales, from the large active regions which can occasionally evolve on sizes of some ten thousand kilometers and lifetimes of weeks to months, to magnetic bright points with lifetimes of a few minutes and sizes of a some ten kilometers. This chapter presents a summary of the key findings and the significance of this research and its contribution to the scientific community.

Summary of Key Findings of the research and their Implications

Photospheric proper motions have been observed to follow a Rayleigh distribution. However, the presence of intense and abrupt flux emergences reveals a second component that contributes and provides valuable insights into the underlying processes during these transitions. The first distribution gives information about the proper motions associated with the background motions of the granular region and the quiet magnetic fields, whereas the second distribution becomes evident when new magnetic fields emerge from the solar interior. This second distribution also indicates the correlation between the existing plasma and the changes it suffers during the appearance of the new rising magnetic fields. Furthermore, the temporal evolution of the Rayleigh distribution parameters demonstrates a correlation and anti-correlation between the apparent motions of plasma and the magnetic features. Such findings contribute as an indicator of the presence of newly emergent flux even before it becomes visible in the photosphere.

Intense magnetic fields can form various magnetic structures on the Sun, including solar pores, sunspots, and active regions, each exhibiting distinct properties. These structures can be identified and classified by using different intensity thresholds. A novel empirical approach, known as the Jurčák criterion, permits the differentiation of these features based on physical parameters such as the vertical magnetic field. When investigating the boundary of solar pores, various magnetic variables are utilised. As expected, the inclination angle on their boundaries remains predominantly vertical ($\sim 30^\circ$) with maximal values of the vertical magnetic field on the boundaries of the studied solar pores ranging from 1400 G to 1600 G. These findings may shed light on the characteristics and behaviour of solar pores and contribute to a deeper understanding of the Sun's magnetic phenomena.

Continuous emergence of magnetic fields across the solar surface gives rise to small-scale flux tubes or magnetic bright points observed mainly in the G-band. Through morphological (size, area) and dynamical analysis (velocity), a two-component log-normal distribution classifying MBPs into two different categories was discovered. Understanding these distinctions can aid in characterizing such small-scale magnetic structures, providing insights into their evolution and influence on solar phenomena, with special relevance in the context of the Quiet Sun.

Significance of the Research and its Contribution to the Community

Understanding the properties of the magnetic field and its interaction with solar plasma is crucial to the advancement of solar physics. The findings from Paper 1 (Chapter 3) revealed that the evolution of velocity distribution parameters, inferred from intensity maps, undergoes changes in the presence of magnetic elements before the formation of an active region. These valuable insights hold the potential to enhance our ability to predict the emergence of active regions through full-disk observations, as they allow the detection of small changes in both horizontal and vertical velocity distributions during their evolution.

Studying the evolution and properties of the magnetic field of different manifestations of solar activity such as active regions or solar pores, contributes a better understanding of the global and local magnetic field in the Sun. The investigation developed in Paper 2 (Chapter 4) yields magnetic field parameters such as the vertical magnetic field and the magnetic field inclination angle associated with the observed data by SDO-HMI. These findings may help to improve the development of different models or simulations of flux tubes, extending the possibility of comparing the observations and theoretical simulations.

Previous studies have treated MBPs as simple and congruent representations of a magnetic flux tube, described by a single-component distribution. However, recent research, such as the work done by Keys et al. (2019), suggests that the magnetic field of MBPs follows a two-component distribution. The study made in Paper 3 (Chapter 5) supports the two-component and two-population theory by demonstrating that the area, and derived diameter, distribution of MBPs, as well as their velocity distribution follow two-component distributions. In conclusion, this study significantly reinforces the notion of sub-populations of MBPs, potentially linked to their creation process or location on the Sun.

J. I. Campos Rozo: Publication list

Journals

- [1] T. S. Community, S. J. Mumford, S. Christe, D. Pérez-Suárez, J. Ireland, A. Y. Shih, A. R. Inglis, S. Liedtke, R. J. Hewett, F. Mayer, K. Hughitt, N. Freij, T. Meszaros, S. M. Bennett, M. Malocha, J. Evans, A. Agrawal, A. J. Leonard, T. P. Robitaille, B. Mampaey, J. I. Campos-Rozo, and M. S. Kirk. “SunPy—Python for solar physics”. In: *Computational Science & Discovery* 8.1 (July 2015), p. 014009. DOI: [10.1088/1749-4699/8/1/014009](https://doi.org/10.1088/1749-4699/8/1/014009). URL: <https://dx.doi.org/10.1088/1749-4699/8/1/014009>.
- [2] J. I. Campos Rozo, D. Utz, S. Vargas Dominguez, A. Veronig, and T. Van Doorsselaere. “Photospheric plasma and magnetic field dynamics during the formation of solar AR 11190”. In: *Astronomy & Astrophysics* 622, A168 (Feb. 2019), A168. DOI: [10.1051/0004-6361/201832760](https://doi.org/10.1051/0004-6361/201832760). arXiv: [1901.02437 \[astro-ph.SR\]](https://arxiv.org/abs/1901.02437).
- [3] S. Mumford et al. “SunPy: A Python package for Solar Physics”. In: *The Journal of Open Source Software* 5.46, 1832 (Feb. 2020), p. 1832. DOI: [10.21105/joss.01832](https://doi.org/10.21105/joss.01832).
- [4] J. Palacios, D. Utz, S. Hofmeister, K. Krikova, P. Gömöry, C. Kuckein, C. Denker, M. Verma, S. J. González Manrique, J. I. Campos Rozo, J. Koza, M. Temmer, A. Veronig, A. Diercke, I. Kontogiannis, and C. Cid. “Magnetic Flux Emergence in a Coronal Hole”. In: *Solar Physics* 295.5, 64 (May 2020), p. 64. DOI: [10.1007/s11207-020-01629-9](https://doi.org/10.1007/s11207-020-01629-9). arXiv: [2006.11779 \[astro-ph.SR\]](https://arxiv.org/abs/2006.11779).
- [5] G. Berrios Saavedra, D. Utz, S. Vargas Dominguez, J. I. Campos Rozo, S. J. González Manrique, P. Gömöry, C. Kuckein, H. Balthasar, and P. Zelina. “Observational evidence for two-component distributions describing solar magnetic bright points”. In: *Astronomy & Astrophysics* 657, A79 (Jan. 2022), A79. DOI: [10.1051/0004-6361/202141231](https://doi.org/10.1051/0004-6361/202141231). arXiv: [2110.12404 \[astro-ph.SR\]](https://arxiv.org/abs/2110.12404).
- [6] J. I. Campos Rozo, S. Vargas Dominguez, D. Utz, A. M. Veronig, and A. Hanslmeier. “Exploring magnetic field properties at the boundary of solar pores: A comparative study based on SDO-HMI observations”. In: *Astronomy & Astrophysics* 674, A91 (June 2023), A91. DOI: [10.1051/0004-6361/202346389](https://doi.org/10.1051/0004-6361/202346389). arXiv: [2304.13212 \[astro-ph.SR\]](https://arxiv.org/abs/2304.13212).

Proceedings and others

- [7] S. Vargas Domínguez, G. Berrios Saavedra, D. Utz, J. I. Campos Rozo, S. González Manrique, P. Gömöry, C. Kuckein, H. Balthasar, and P. Zelina. “Evidence For Two-component Distributions Describing Magnetic Bright Points In The Solar Photosphere”. In: *American Astronomical Society Meeting Abstracts*. Vol. 53. American Astronomical Society Meeting Abstracts. June 2021, 113.10, p. 113.10.
- [8] J. I. Campos Rozo, D. Utz, and S. Vargas Domínguez. *The Science of EST. Scientific challenges to be addressed by the European Solar Telescope*. Vol. 1. Instituto de Astrofísica de Andalucía, Consejo Superior de Investigaciones Científicas, May 2020, p. 92.
- [9] D. Utz, C. Kuckein, J. I. Campos Rozo, S. J. González Manrique, H. Balthasar, P. Gömöry, J. P. Hernández, C. Denker, M. Verma, I. Kontogiannis, K. Krikova, S. Hofmeister, and A. Diercke. “Revisiting the building blocks of solar magnetic fields by GREGOR”. In: *Solar and Stellar Magnetic Fields: Origins and Manifestations*. Ed. by A. Kosovichev, S. Strassmeier, and M. Jardine. Vol. 354. Jan. 2020, pp. 38–41. DOI: [10.1017/S174392131900989X](https://doi.org/10.1017/S174392131900989X).
- [10] J. I. Campos Rozo, D. Utz, A. Veronig, and S. Vargas Domínguez. “Modelling the solar photospheric plasma and magnetic field dynamics in the quiet Sun and comparison of these results with the flow fields in an evolving active region”. In: *Proceedings of Tenth Workshop Solar Influences on the Magnetosphere*. Ed. by K. Georgieva, B. Kirov, and D. Danov. June 2018, pp. 37–42.
- [11] V. Quintero Ortega, S. Vargas Dominguez, and J. I. Campos Rozo. “Analysis of large-scale photospheric dynamics during the solar cycle 24”. In: *Scientia et Technica* 23 (June 2018), pp. 288–292. DOI: [10.22517/23447214.17541](https://doi.org/10.22517/23447214.17541).

- [12] J. I. Campos Rozo, D. Utz, A. Veronig, and S. Vargas Domínguez. “Modelling the solar photospheric plasma and magnetic field dynamics during the emergence of AR 11190”. In: *Proceedings of the 24th National Solar Physics Meeting*. June 2018, 1, p. 1.
- [13] O. Kuehner, D. Utz, R. Muller, T. Van Doorsselaere, N. Magyar, A. Veronig, J. I. Campos Rozo, and P. Jelinek. “Formation Heights of HINODE SOT/BFI Filters”. In: *Central European Astrophysical Bulletin* 42, 9 (Jan. 2018), p. 9.
- [14] J. I. Campos-Rozo and S. Vargas Domínguez. “A Python-based interface to examine motions in time series of solar images”. In: *Fine Structure and Dynamics of the Solar Atmosphere*. Ed. by S. Vargas Domínguez, A. G. Kosovichev, P. Antolin, and L. Harra. Vol. 327. Oct. 2017, pp. 25–27. DOI: [10.1017/S1743921317003568](https://doi.org/10.1017/S1743921317003568).
- [15] D. Utz, T. van Doorsselaere, N. Magyar, M. Bárta, and J. I. Campos Rozo. “P-mode induced convective collapse in vertical expanding magnetic flux tubes?” In: *Fine Structure and Dynamics of the Solar Atmosphere*. Ed. by S. Vargas Domínguez, A. G. Kosovichev, P. Antolin, and L. Harra. Vol. 327. Oct. 2017, pp. 86–93. DOI: [10.1017/S174392131700401X](https://doi.org/10.1017/S174392131700401X).
- [16] D. Utz, T. Van Doorsselaere, O. Kühner, N. Magyar, I. Calvo Santamaría, and J. I. Campos Rozo. “Fulfilling Magnetostatic Conditions in Numerical Simulations of Expanding Flux Tubes”. In: *Central European Astrophysical Bulletin* 40 (Jan. 2016), pp. 9–22.
- [17] J. I. Campos Rozo and S. Vargas Domínguez. “Sunpy - Python para física solar: una implementación para seguimiento de correlaciones locales”. In: *Revista de Ciencias*. Vol. 6/1. IV Congreso Colombiano de Astronomía y Astrofísica. Spanish article. Mar. 2015.
- [18] J. I. Campos Rozo, S. Vargas Domínguez, and D. Utz. “Dinámica de puntos brillantes en la fotósfera solar”. In: *Revista de Ciencias*. Vol. 6/2. IV Congreso Colombiano de Astronomía y Astrofísica. Spanish article. Mar. 2015.
- [19] J. I. Campos Rozo and S. Vargas Domínguez. “SunPy: Python for Solar Physics. An implementation for local correlation tracking”. In: *Central European Astrophysical Bulletin* 38 (Jan. 2014), pp. 67–72.

Thesis Documents

- [20] J. I. Campos Rozo, A. M. Veronig, and D. Utz. “Plasma and magnetic field interaction on large- and small-scales within the solar atmosphere.” Under preparation. PhD thesis. 2023.
- [21] J. I. Campos Rozo, S. Vargaz Domínguez, and D. Utz. “Evolution and dynamic properties of photospheric plasma in solar active regions”. MA thesis. Universidad Nacional de Colombia, 2017.
- [22] J. I. Campos Rozo, B. Calvo Mozo, and D. Utz. *Dinámica de puntos brillantes en la fotósfera solar. English: Dynamics of bright points on the solar photosphere*. Bachelor thesis. 2014.

Colophon

This thesis was typeset with L^AT_EX 2_<. It uses the *Clean Thesis* style developed by Ricardo Langner, available at <http://cleanthesis.der-ric.de/>. The design of the *Clean Thesis* style is inspired by user guide documents from Apple Inc.

The template was adapted by Desmond Grossmann, BSc, Stefan Janisch, BSc, Lea Schimak and Paul Beck, PhD to implement the editorial guidelines of *Astronomy & Astrophysics* and the cooperate-identity guidelines of the University of Graz for the Institute for Physics. This thesis uses the template, released on the webpage of the *Department for Geophysics, Astrophysics and Meteorology (IGAM)*¹ on February 12, 2021.

¹ <https://physik.uni-graz.at/de/igam/>

Declaration

I declare that I have authored this thesis independently, that I have not used other than the declared sources/resources, and that I have explicitly indicated all material that has been quoted either literally or by content from the sources used. The text document uploaded to UNIGRAZonline is identical to the present Ph.D.'s thesis.

Graz, August 10, 2023

MSc. Jose Iván Campos Rozo